Department of Geography
University of Fribourg

Master Thesis

Spatial and Temporal Variability of Soil Moisture and the Influence on the Thermal Regime of Permafrost at the Schilthorn (Bernese Alps)

Author
Adrian Wicki
Seilerstrasse 25
3011 Bern

Supervison
Prof. Dr. Christian Hauck
Cécile Pellet

Fribourg, January 2016

Abstract

Soil moisture may considerably impact the thermal regime of permafrost soils. At Schilthorn (2970 m asl, Swiss Alps), soil moisture has been identified to be a major contributor to the thermal differences between two borehole locations which are located 10 m apart. In this study, the spatial distribution and temporal variability of soil moisture at Schilthorn were assessed during the summer 2014 and compared to the thermal behaviour at the boreholes.

Electrical resistivity tomography (ERT) was used to assess the spatial variability of soil moisture. A small electrode spacing (0.8 m) and a time-lapse inversion scheme were used to detect small scale hydrological processes under variable snow and weather conditions as well as in different geological contexts. Additional ERT data of an automated profile line provided daily measurements at a coarser resolution (2 m spacing). The resistivity changes were compared to soil moisture conditions measured by soil moisture monitoring sensors. Infiltration events were identified and related to snow melt and precipitation events using meteorological, snow depth and runoff modelling data. Finally, the hydrological regimes were compared to the ground temperatures measured at the boreholes to identify their thermal impact.

At Schilthorn, infiltration is mainly limited by the thaw depth and bedrock topography, however even under frozen conditions, some infiltration takes place. The thermal impact of soil moisture was found to vary greatly depending on soil texture, geological setting and hillslope water flow. In general, latent heat fluxes are dominant through freezing and evaporation of soil water, while sensible heat fluxes are negligible. According to our findings, the change of ground thermal properties with depth (thermal conductivity and diffusivity) is a major contributor to the different thermal behaviour. Finally, high soil moisture is thought to precondition active layer thickening, whereas heat conduction is the dominant process of heat transport in the subsurface.

Keywords: Soil Moisture, Non-Conductive Heat Transfer, Alpine Permafrost Soils, Latent Heat

Acknowledgements

First of all, I would like to thank my supervisors, Christian Hauck and Cécile Pellet, for their help with all my questions, their inputs in the field and the idea for this interesting topic. Moreover, I would like to thank Christin Hilbich for her valuable inputs on everything ERT related, Matthias Huss for the installation and helpful tips on the GERM model, and Benno Staub, Martin Scherler, Jeannette Noetzli and Martin Hoelzle for their support and for providing me with additional data.

Also, I would like to thank the Schilthornbahn AG, particularly Johannes Feuz, for the logistics and the use of their apartment on the summit, which was very useful to me.

A special thanks goes to the numerous field helpers who not only helped digging snow or carrying heavy field equipment, but also brought a great atmosphere to the Schilthorn. In alphabetical order, Joaquim, Joël, Jutta, Kommer, Manuela, Marina, Michael and Michael, Sämi, Sebastian and Simon.

Finally, I would like to thank my parents Lisbeth and Werner, who after all encouraged me to follow my interests and made it possible to do so.

Contents

1 Introduction **1**

1.1 Context . . . 1

1.2 Aims and Research Questions . . . 2

1.3 Structure of the Work . . . 3

2 Theory **4**

2.1 Definitions . . . 4

2.2 Climate-Ground Thermal Interactions . . . 6

2.3 Energy Exchange at the Surface . . . 7

2.4 Subsurface Heat and Water Flow . . . 9

2.4.1 Soil-Water-Interactions . . . 10

2.4.2 Conductive Heat Transfer . . . 13

2.4.3 Non-Conductive Heat Transfer . . . 15

2.5 Hillslope Hydrology . . . 17

3 Study Area **19**

3.1 Climate . . . 19

3.2 Lithology . . . 20

3.3 Permafrost . . . 20

3.3.1 Measurements . . . 20

3.3.2 Permafrost Characteristics . . . 21

3.4 Energy Balance Components . . . 22

4 Methods **24**

4.1 Electrical Resistivity Tomography . . . 25

4.1.1 General Principles . . . 25

4.1.2 Measurement Configurations . . . 28

4.1.3 The Inversion Problem . . . 29

4.1.4 Application of ERT . . . 30

4.1.5 Measurement Setup . . . 31

4.2 Soil Moisture Measurements . . . 33

4.2.1 Soil Moisture Sensors . . . 33
4.2.2 Soil Samples . . . 35
4.3 Meteorological Measurements . . . 36
4.3.1 Air Temperature and Snow Depth . . . 36
4.3.2 Precipitation . . . 37
4.3.3 Snow Distribution . . . 37
4.4 Borehole Temperature Measurements . . . 38
4.5 Runoff Modelling . . . 39
4.5.1 Mass Balance Module . . . 40
4.5.2 Runoff Routing Module . . . 41
4.5.3 Model Adaptations . . . 42
4.5.4 Model Setup and Calibration . . . 43

5 Thermal Regime **44**
5.1 Meteorology and Snow Depths . . . 44
5.2 Spatial Snow Distribution in Summer 2014 . . . 47
5.3 Ground Temperatures . . . 48
5.3.1 Temporal Evolution . . . 48
5.3.2 Infiltration Events . . . 51
5.3.3 Thermal Regimes . . . 55
5.4 Discussion . . . 58

6 Hydrological Regime **60**
6.1 Soil Moisture Sensors . . . 60
6.2 Field Observations . . . 63
6.3 Soil Samples . . . 65
6.4 Runoff Modelling . . . 65
6.5 Discussion . . . 68

7 Resistivity Regime **72**
7.1 Apparent Resistivity . . . 72
7.2 Specific Resistivity . . . 73
7.3 Electrical Resistivity Tomograms . . . 75
7.3.1 Specific Resistivities of all Profile Lines . . . 75
7.3.2 SCHpara and SCVpara Resistivity Change . . . 77
7.3.3 SCH Resistivity Change . . . 82
7.4 Discussion . . . 85
7.4.1 Spatial Soil Moisture Distribution . . . 85
7.4.2 Situation at the Boreholes . . . 86

8 General Discussion **88**

9 Conclusion **91**

9.1 Conclusion 91

9.2 Outlook 93

Bibliography **95**

A Appendix **103**

A.1 Borehole Temperatures 103

List of Figures

2.1 Characteristic temperature profile in perennially frozen ground 5
2.2 Flow chart of the interactions at the surface boundary layer. 7
2.3 Sketch of adsorption and capillary water. 11
2.4 Hillslope runoff generation during strong infiltration events. 18

3.1 Location of the Schilthorn and view on the summit. 19
3.2 2D profile a north-south cross section of the Schilthorn summit showing the subsurface temperature field. 22
3.3 Monthly values of the energy balance components at Schilthorn from summer 1999 to winter 2013. 23

4.1 Overview of the measurement instruments in the study area. 24
4.2 Typical four-electrode configuration in resistivity measurements. 26
4.3 Lines of equipotential and equal currents between two current electrodes. . 27
4.4 Schematic overview of the Wenner, Wenner-Schlumberger and Dipole-Dipole Arrays. 29
4.5 Map and installation depths of the soil moisture sensors 34
4.6 Overview of the study area, the subbasins and the points of snow depth measurements for the GERM simulation. 42

5.1 Air temperature, precipitation and snow depth at Schilthorn in 2014. 44
5.2 Air temperature and precipitation in 2014 in comparison with long-term climate means. 45
5.3 Time series of snow depth records in various years at Schilthorn. 46
5.4 Spatial snow distribution at the study site in summer 2014 47
5.5 Temporal evolution of daily mean subsurface temperatures at the three boreholes in 2014. 49
5.6 Contour Plot of the daily mean subsurface temperatures at SCH5198 in 2000 to 2014. 50
5.7 Contour Plot of the daily mean subsurface temperatures at SCH5000 in 2003 to 2014 (uppermost 13 m). 50

5.8 Contour Plot of the daily mean subsurface temperatures at SCH5200 in 2003 to 2014 (uppermost 12 m). 51
5.9 Data compilation showing infiltration events during spring. 52
5.10 Data compilation showing infiltration events during summer. 53
5.11 Data compilation showing infiltration events during late summer and autumn. 54
5.12 Temperature envelopes of the top 20 m at the three boreholes. 55
5.13 Typical shapes of thermal orbits at the boreholes. 56

6.1 Daily mean volumetric soil moisture content in 2014 60
6.2 Vol. soil moisture measured by the SMT and PICO64 sensors in summer 2014. 61
6.3 Seasonal variation of volumetric soil moisture measured by the SISOMOP sensors in various years. 62
6.4 Photographs of near-surface soil moisture regimes around outcrops. 63
6.5 Photographs of near-surface soil moisture regimes below snow patches. . . . 64
6.6 Photographs of near-surface soil moisture regimes near SCH5198 and due to precipitation. 64
6.7 Volumetric soil moisture content of soil samples and the hand probe taken along the ERT profile lines. 65
6.8 Spatial snow depth distribution as simulated by GERM (degree day model) at four dates in summer 2014. 66
6.9 Hourly runoff and SWE modelled by GERM opposed by hourly temperature values and precipitation sums. 67
6.10 Hourly runoff modelled by GERM and hourly values of volumetric soil moisture. 68

7.1 Apparent resistivities at four near-surface locations opposed by soil moisture measurements. 73
7.2 Specific Resistivities along two virtual boreholes in the vicinity of SCH5198 and SCH5000. 74
7.3 Logarithmic percentage change in specific resistivity along two virtual boreholes in the vicinity of SCH5198 and SCH5000 74
7.4 Inverted resistivity tomogram of the A-ERT profile line. 76
7.5 Inverted resistivity tomograms of the SCHpara and SCVpara profile lines. . 77
7.6 Resistivity tomogram and logarithmic percentage change in specific resistivity at SCHpara1. 78
7.7 Resistivity tomogram and logarithmic percentage change in specific resistivity at SCHpara1_ext. 79
7.8 Resistivity tomogram and logarithmic percentage change in specific resistivity at SCHpara2. 80

7.9 Resistivity tomogram and logarithmic percentage change in specific resistivity at SCHpara3. 81
7.10 Resistivity tomogram and logarithmic percentage change in specific resistivity at SCVpara1. 82
7.11 Specific resistivity tomograms and logarithmic percentage change in specific resistivities for several infiltration events at the A-ERT profile line SCH. . . 83

A.1 Contour Plot of the daily mean subsurface temperatures at SCH5000 in 2003 to 2014. 103
A.2 Contour Plot of daily mean subsurface temperatures at SCH5200 in 2003 to 2014. 104
A.3 Thermal Orbits for daily mean temperatures in the year 2014 at SCH5198 for all temperature sensors. 105
A.4 Thermal Orbits for daily mean temperatures in the year 2014 at SCH5000 for the upper 15 m. 106
A.5 Thermal Orbits for daily mean temperatures in the year 2014 at SCH5200 for the upper 12 m. 107

List of Tables

2.1 Thermal properties of soils and soil constituents. 15

4.1 Resistivity ranges in different geologic materials. 27
4.2 ERT measurements conducted in 2014. 31
4.3 Overview of the available soil moisture sensor data. 33
4.4 Overview of the meteorological data and corresponding data gaps in 2014. . 36
4.5 Overview of the boreholes ground temperature measurements and corresponding data gaps in 2014. 38

5.1 Classification of the shapes of the thermal orbits at the boreholes. 57

Chapter 1

Introduction

In this chapter, the context of the work is presented, the aims and research questions are formulated and an overview of the work's structure is given.

1.1 Context

The thermal regime of permanently frozen ground can be seen as a function of climate, microclimate and lithology. While a cold climate is the precondition for the presence of permafrost, local factors such as the local snow cover, the albedo or the lithology as well as the local microclimate overprint the general climate conditions and contribute to the local thermal regime. (Haeberli et al., 2010) As a consequence, ground temperatures may vary considerably over small spatial scales. In the Alps, where topography is complex and ground properties are spatially very heterogeneous, ground temperatures are reported to vary up to 15° C on horizontal distances of as short as 1 km. In the Arctic in contrary, such variability occurs over horizontal distances on the order of 1000 km. (Gruber and Haeberli, 2010)

In this context, soil moisture conditions may considerably modify the energy exchange at the surface and in the ground and as such have a large impact on the thermal regime (Williams and Smith, 1989). While research on the spatial and temporal variability of soil moisture and its impact on the thermal regime of permafrost soils has been ongoing in the past 30 years in arctic areas, little is currently known about the processes and their importance in alpine permafrost (Gruber and Haeberli, 2010).

At Schilthorn in the Swiss Alps, ground temperatures and ice contents have been monitored over the past 15 years (Noetzli, 2013). In the SNSF-project TEMPS (Thermal Evolution of Permafrost in Switzerland), the sensitivity of the permafrost at Schilthorn

for degradation was assessed in multiple studies (e.g. Scherler et al., 2013). Currently, soil moisture is being studied in the SNSF-project SOMOMOUNT (Soil moisture in mountainous terrain and its influence on the thermal regime in seasonal and permanently frozen terrains) for which new soil moisture sensors were installed. Substantial differences in the thermal regime occur between two borehole locations, situated just 20 m apart. Data series analyses indicate that the ground temperatures in the near-surface soil layers are influenced by latent heat effects and convective heat transfer by water. (Harris et al., 2009) The presence of such processes was further assumed by other field and modelling studies (Hilbich et al., 2008; Scherler et al., 2010). However, little is known about the spatial variability of the hydrological processes and subsequent thermal impacts at the study site. This study aims at filling this knowledge gap and ought to contribute to the general lack of knowledge on the thermal impact of soil moisture in alpine permafrost soils.

1.2 Aims and Research Questions

This work aims at assessing the impact of soil moisture on the thermal regimes of the permanently frozen ground at Schilthorn. More precisely, the differences in the thermal regimes of the boreholes at Schilthorn are to be attributed to differences in the soil moisture conditions. In a first step, the spatial and temporal distribution patterns of soil moisture at Schilthorn are assessed. A particular focus is laid on the spring and summer months 2014. Secondly, the differences in the thermal regimes at the three boreholes are analysed and related to the corresponding soil moisture conditions.

Regarding the spatial and temporal distribution patterns of soil moisture, the following research questions are to be answered:

- How are the spatial snow melt patterns at Schilthorn?
- How much water from snow melt and precipitation events is available proportionally?
- What is the infiltration depth?
- Does preferential flow occur?
- How does the soil moisture regime change with respect to the active layer growth?
- What are the soil moisture conditions at the boreholes?

Regarding the thermal impact of soil moisture, following research questions are to be answered:

- How does the thermal impact of water infiltration events under frozen and unfrozen conditions differ?

- What is the difference in the thermal impact between the infiltration of relatively cold snow melt water compared to warmer rain water?
- How does soil moisture contribute to active layer growth?
- What is the relative importance of non-conductive heat transport through soil moisture compared to heat transport through conduction?

1.3 Structure of the Work

In chapter two, an introduction on the state of research regarding alpine permafrost soils is given. A focus is laid on the energy exchange in permafrost soils and processes related to the spatial distribution and temporal evolution of soil moisture. It is followed by the presentation of the study area in chapter three and the outline of the methods in chapter four. The results are presented and discussed in three thematic chapters including the meteorological and snow conditions as well as ground temperatures in chapter five, the soil moisture conditions in chapter six and the resistivity measurements in chapter seven. In chapter eight, the thermal impact of soil moisture is wrapped up in a general discussion. The conclusions are drawn in chapter nine.

Chapter 2

Theory

In this chapter, a literature review is given of the principal concepts of permanently frozen grounds as well as on the state of knowledge of processes related to the mass and heat exchange in alpine permafrost soils. Soils are hereinafter referred to as bodies of unconsolidated debris. In high alpine areas as opposed to lower elevations, soils are primarily prone to physical weathering processes, hardly vegetated and usually have no soil layering.

First, some terms are defined and the general interactions between climate and permafrost soils are outlined. Secondly, an explanation of the energy balance at the surface is given. It is followed by a thorough discussion of the ground heat flux with an emphasis on soil physics and the role of soil moisture in non-conductive heat transfer. Finally, hillslope hydrological processes in alpine permafrost soils are discussed.

2.1 Definitions

Permafrost is commonly defined as ground (rocks or soils and included material) that stays at or below 0° C for at least two consecutive years (van Everdingen, 2005). As for the purely thermal definition, permafrost may but not necessarily needs to contain moisture in the form of liquid water or ice. Additionally, glaciers are not considered as permafrost (Gruber and Haeberli, 2010).

The characteristic temperature profile of permafrost ground and associated terms are shown in Figure 2.1. The *permafrost body*, also denoted by the *permafrost thickness*, is delimited at the bottom of the profile by the *permafrost base* where the thermal cooling from the surface is in equilibrium with the heat flux from the earth's interior (geothermal heat flux). At the surface, seasonal air temperature variations cause variations in the ground temperatures which are progressively damped and lagged with depth. (Williams

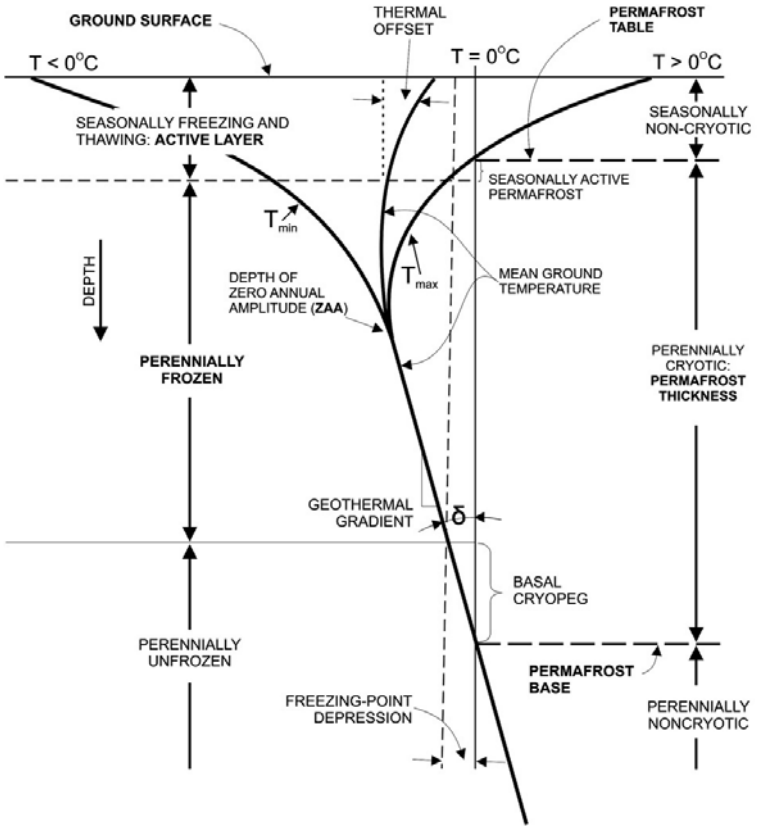


Figure 2.1: Temperature profile and associated terms in perennially frozen ground (Dobinski, 2011).

and Smith, 1989) Annual variations in mountain permafrost typically propagate until depths of 10 to 20 m, also referred to as the *depth of zero annual amplitude (ZAA)*, where seasonal temperature fluctuations are damped to less than 0.1° C. At the top of the profile, the permafrost body is delimited by the *permafrost table* above which ground temperatures exceed 0° C in the summer. The layer in which the seasonal air temperature variations cause ground ice to thaw is called the *active layer*. Due to the effect of supercooling, the freezing point of water (the temperature at which water solidifies) may be slightly depressed and the active layer may then extend below the permafrost table. (van Everdingen, 2005) In alpine permafrost, the active layer usually amounts to a thickness of 0.5 to 8 m (Gruber and Haeberli, 2010), while it typically ranges between 15 cm and 1 m in the Arctic (van Everdingen, 2005). In the top part of the profile, the difference between the *mean annual ground surface temperature (MAGST)* and the *mean annual air temperature (MAAT)* is called *surface offset* or *thermal offset*. This temperature offset is caused by a stronger cooling in winter than warming in summer due to changes in thermal conductivity which are related to the ice, water or air content or air convection in blocky layers. (Harris et al., 2009)

Permafrost exists at high latitudes or high altitudes, where cold climates favour its occurrence. Permafrost is commonly categorized into *latitudinal (polar) permafrost*,

mountain permafrost and *plateau permafrost* (exclusively on the Tibet Plateau). (French, 2007) These categorizations are based on common properties and do not sharply delineate geographic spaces. They may even be applicable at the same location. (Gruber and Haeberli, 2010) In Switzerland, the area covered by permafrost makes up to 4-6% of the territory which corresponds to double the area of glaciers. (Keller et al., 1998)

2.2 Climate-Ground Thermal Interactions

Generally, the ground thermal regime and its temporal and spatial variability can be seen as a function of climate, microclimate and lithology. In order to assess the different factors influencing the ground thermal regime, they can be grouped into the following scales and process domains. (Gruber and Haeberli, 2010)

(a) Climate scale: On a regional scale, latitude and global circulation determine the distribution of cold climates.
(b) Topography scale: Local topography (elevation, slope, aspect) influences the microclimate, the energy fluxes at the surface and the mass balance by modifying air temperature, solar radiation, and snow distribution by wind and avalanches, respectively.
(c) Ground conditions: Lithology and ground properties locally overprint the topography and climate signals by influencing the heat and mass transfer in the ground.

In mountain permafrost soils, surface and near-surface properties may vary considerably on a small spatial scale. The effects of topography and ground conditions may lead to ground temperature differences of up to 15° C over horizontal distances of as short as 1 km. In polar lowlands in contrast, similar temperature variations occur only over horizontal distances of about 1000 km. (Gruber and Haeberli, 2010)

Figure 2.2 shows a schematic view of the atmosphere-ground interactions which occur at the surface layer and of the processes that govern the heat fluxes within the ground. Climate and weather conditions determine the basic disposition for permafrost occurrence. The climate is locally altered by site-specific factors such as topography, albedo, snow cover, lithology or surface roughness owing for a site-specific microclimatology. These factors determine the local energy balance at the surface, which is furthermore influenced by the soil moisture conditions in the surface layer. From the energy balance, the surface temperature can be derived, which in return modifies the soil moisture conditions. Ultimately, the surface temperatures propagate into the ground and result in a characteristic temperature regime. The propagation of the ground temperatures is influenced by the local thermal properties of the soil which in return are influenced by the

ground temperature regime and the soil moisture conditions in the ground. The base of the permafrost body is determined by the geothermal heat flux from the earth's interior. (Williams and Smith, 1989)

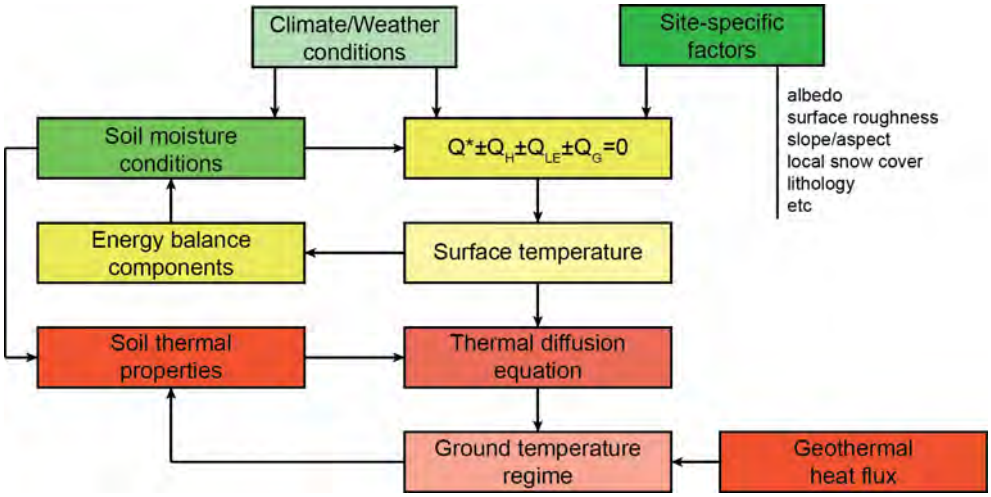


Figure 2.2: Flow diagram of the interactions occurring in the surface boundary layer affecting the thermal regime of permafrost ground (modified after Williams and Smith, 1989).

To conclude, the ground temperature regime can be expressed as a function of climate, local factors and lithology and can be significantly different from mean air temperatures. In order to be able to interpret the ground temperature regime at a specific site and to address temperature signals to specific processes, it is important to understand the magnitude as well as the temporal and spatial variability of the different processes. In the following, the processes influencing the ground temperature regime are discussed in detail on the basis of the surface energy balance (Section 2.3) and the ground heat flux (Section 2.4).

2.3 Energy Exchange at the Surface

The thermal regime in the uppermost ground layers is governed by the heat and water exchange at the surface, as expressed by the surface energy balance (Hoelzle, 1994):

$$Q_R + Q_H + Q_{LE} + Q_G + Q_M = 0 \tag{2.1}$$

where Q_R is the radiation balance, Q_H is sensible and Q_{LE} is the latent heat flux, both forming the turbulent heat fluxes of the atmosphere, Q_G is the ground heat flux and Q_M is the energy required to melt snow. Changes of any component of the energy balance lead to changes in the ground surface temperature. The surface temperature regime typically

shows yearly cycles overprinted by daily variations both of which are mainly influenced by the radiation budget. Changes in the cloudiness, the weather conditions and long term climate changes can cause further irregular temperature variations. In the following the individual components of the energy balance are discussed in more detailed. The ground heat flux is discussed in Section 2.4.

The radiation balance Q_R is separated into a short wave term $K\downarrow(1-\alpha)$ for wave lengths shorter than 4 μm, and a long wave term $L\downarrow - L\uparrow$ with wave lengths longer than 4 μm. $K\downarrow$ is mainly influenced by the azimuth and zenith of the sun. As such, it is directly related to the sunshine duration. It is further modulated by the local terrain through exposition, slope and horizon. The surface albedo controls the amount of backscattered short wave radiation and complements the short wave radiation budget. Due to highly variable atmospheric conditions and due to the spatially variable snow cover, the short wave radiation budget can be temporally highly variable. (Hoelzle, 1994)

$L\downarrow$ on the contrary is emitted from the atmosphere and depends on the air temperature and the atmosphere's emissivity, which is directly related to the thickness and height of the clouds. $L\uparrow$ is primarily dependent on the surface temperature and the surface emissivity and is to a small extent composed of reflected $K\downarrow$. As such, the long wave radiation budget mainly varies on a seasonal scale and in relation to large weather systems and thus has a medium spatial and temporal variability. In general, it is positive in summer and negative in winter, i.e., energy is gained in summer and lost in winter. (Hoelzle, 1994)

The sensible heat flux Q_H depends on the heat capacity of air, the turbulent transport coefficient (related to wind speed, surface roughness and the temperature gradient between the surface and the air temperature) and the temperature gradient within the atmosphere. The temporal variability of the sensible heat flux can be tremendous. The latent heat flux Q_{LE} corresponds to the energy exchange through evaporation and is related to the density of air, the heat of evaporation, the turbulent transport coefficient as described above and the water vapour gradient. The latent heat flux is related to the thermal balance and the soil moisture at the surface. In steep mountainous terrain where water drains quickly, the impact of the latent heat flux is assumed to be small. (Hoelzle, 1994)

Q_M describes the energy used to melt snow. As for this, it is negligible throughout most of the year. However, during the snow melt period, Q_M acts as a significant sink for energy and it can take up between 20 to 50% of the radiation energy. After the snow melt period, snow fall events in summer can cause significant cooling of surface and air temperatures. (Hoelzle, 1994)

Measurements of the energy balance at mountain permafrost sites in the Alps conclude the following (Hoelzle, 1994):

- The net radiation is by far the dominant factor in the energy balance, whereas the short wave balance inhibits the greatest seasonal variation.
- The sensible heat flux determines the basic disposition for permafrost occurrence whereas the latent heat flux can be locally an important factor.
- The melt energy is only important during the snow melt season.
- The snow cover plays a major role in the modification of the surface energy balance by its influence on the albedo, emissivity and due to its insulation effect.
- In summer, the overall energy balance is positive, whereas in winter, the balance is negative. There is usually a small imbalance of the energy budget which can be explained by advective energy fluxes. (Hoelzle et al., 2001)

2.4 Subsurface Heat and Water Flow

The subsurface heat flow is composed of a conductive and a non-conductive part. Given no water or air flow, the subsurface heat transfer can be described by heat conduction only, which incorporates several effects: The geothermal heat flow from the earth's interior establishes a constantly increasing temperature profile. This long-term steady heat flow is modified in the upper 10 to 20 m by seasonal fluctuations of the surface temperature and ground properties due to atmospheric influences, which may cause an offset to the mean temperature profile. Transient effects such as climate change or climate variability are superimposed on this long-term steady state and may extend hundreds of meters downwards. (Williams and Smith, 1989) Lateral variations such as caused by topographic effects can further modify the temperature profile (Noetzli et al., 2007).

In reality however, the conductive heat transfer may be considerably altered by non-conductive heat transport (Harris et al., 2009). Non-conductive processes are strongly connected to the circulation of water, vapour or air in porous material. They are generally highly variable over space and time and are typically dominant during periods of strong water infiltration such as during the snow melt period or during precipitation events. (Kane et al., 2001)

The following first outlines soil-water-interactions, which play a key role in the ground thermal regime. It is followed by a discussion of the conductive heat transfer, the impact of latent heat effects and a discussion of typical forms of non-conductive heat transfer which are present in alpine permafrost soils.

2.4.1 Soil-Water-Interactions

Soil within the seasonally thawing active layer can be seen as a complex system consisting of two solids (soil matrix and ice) and two fluids (liquid water and air). The composition of these components may vary considerably over time and strongly controls the presence or absence of latent heat effects. It further influences physical soil properties such as the thermal and hydraulic conductivity or the heat capacity (see below). During *saturated unfrozen* conditions, only the matrix and water are present, whereas in *unsaturated unfrozen* soils, air is present too. The situation is more complex under *frozen* conditions: In *saturated frozen* soils, the matrix, ice and water need to be considered whereas in *unsaturated frozen* soils, all four components are present. (Kane et al., 2001)

The fraction of water in the soil is called the soil moisture content or the soil wetness. Its per-mass and per-volume fraction is expressed as following. (Hillel, 2004)

$$w = M_W / M_S \tag{2.2}$$

$$\theta = V_W / V_t = V_W / (V_S + V_W + V_a) \tag{2.3}$$

where the mass wetness w (g/g) is the ratio of water mass M_W to soil mass M_S and the volumetric water content θ (m^3/m^3) is the ratio of water volume V_W to total Volume V_t, which is equal to the sum of the volumes of the solids (V_S), water (V_W) and air (V_a). (Hillel, 2004)

In natural conditions, water is always present in the form of thin films covering the surface of the soil particles, so-called adsorption water (see figure 2.3). Furthermore, capillary water is held at the contact points between two particles due to the bending of the water surface (so-called menisci). In these states, water is bonded very strongly to the soil particles through the presence of bonding forces, namely the van der Waals forces and hydrogen bridges. Further layers of water molecules may increase the soil moisture content through additional hydrogen bridges with the first layer of water molecules, however these bonds are weaker than in the first layer. (Hartge and Horn, 1991) Due to the strong bonding, some adsorption water exists even under the lowest wetness encountered in nature, also referred to as the air dryness. Under the wettest possible conditions, called the condition of saturation, the pore volumes are additionally filled with bulk water. (Hillel, 2004)

Below the freezing point, unfrozen water is only present as adsorption and capillary water. In contrary to bulk water, the freezing point of adsorbed and capillary water is lowered in relation to the strength of the bonding forces acting on the water molecules.

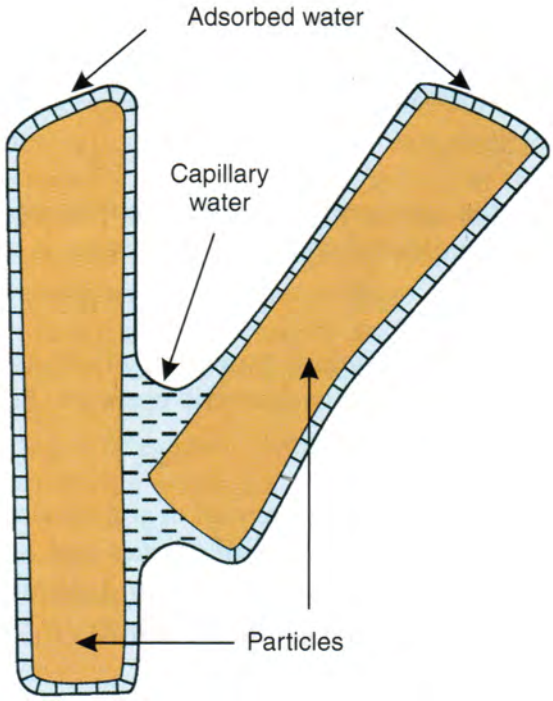


Figure 2.3: Sketch of adsorption and capillary water as it is present around soil particles in unsaturated soils (negative matric potential). (Hillel, 2004)

(Kane and Stein, 1983) The amount of unfrozen water below 0° C thus strongly depends on temperature and gradually decreases until about -3° C (Williams and Smith, 1989). Additionally, water content depends on the soil type, whereas fine-grained soils generally retain more unfrozen water due to their higher specific surface area (Kane and Stein, 1983).

To determine the movement of water in soils, the energy of a specific mass of soil water is expressed through its potential energy (the velocity of moving water is quite slow and the kinetic energy is thus negligible). Water flow between two points is induced when a potential difference is present, while the water flow is directed from higher to lower potential energy. (Hillel, 2004) Therefore, relative potentials expressed through gradients are used to determine the forces acting on water particles. The most important gradients are the gravitational, the pore water pressure and the osmotic gradient: (Kane et al., 2001)

(a) The gravitational gradient is directed downwards and thus enhances the downward movement of water from snow melt or precipitation during spring and summer (Hillel, 2004). It further counteracts the upward movement of water towards the freezing front in autumn or towards the drying surface under evaporation (Kane and Stein, 1983). It is the most dominant gradient of the three (Kane et al., 2001).
(b) The pore water pressure gradient is positive when the hydrostatic pressure is greater than the atmospheric pressure (below the ground water table) and it is

negative when it is lower than atmospheric pressure (above the ground water table). The negative pressure potential is also called the matric potential and results from the capillary and adsorptive forces between water and the soil matrix. The strength of the gradient depends on the moisture content and the soil type: If the soil dries or freezes, the gradient becomes more negative and water will migrate towards the drier zone or the freezing front. Fine-grained soils have a higher specific surface and therefore a higher matric potential. As opposed to the gravitational gradient, the pressure gradient may be directed in either direction. Under dry conditions, it may overcome the gravitational gradient. (Hillel, 2004)

(c) The osmotic gradient forms when pore water freezes and the solute concentration of the residual soil water increases as ions are excluded from the ice crystal lattice. Consequently, water will move towards zones of higher solute concentration. (Hillel, 2004) In mineral soils, the osmotic gradient only plays a minor role and is mostly associated to freezing processes (Kane et al., 2001).

The hydraulic conductivity K_h (m/s) is expressed as the ratio of the flux of water to the potential gradient and describes the ability of a soil to transport water (Hillel, 2004). It is affected by both texture (grain size distribution) and structure (arrangement of solid parts and pore space) and it is greater in highly porous, fractured or aggregated soils. It does not only depend on total porosity but also and primarily on the sizes of the conducting pores. Furthermore, K_h may change through the interaction with water and depending on the water properties. (Hartge and Horn, 1991)

The process of water entry into the soil is called infiltration and it denotes the downward flow of water through the soil surface. The infiltration rate determines how much water will enter the soil column and how much runs off along the surface. The infiltration capacity at the surface is therefore a crucial property in terms of the water balance of a soil. When soil moisture increases at the surface, the matric potential gradient decreases and as a consequence, soil infiltrability decreases too. The infiltrability can thus be highly variable over time. Furthermore, it is lower in a soil which initially was moist compared to initially dry soil. The infiltration rate can further deteriorate due to the sealing of the surface or a blocking of the pores. Higher infiltration rates are observed during preferential flow. As opposed to distributed flow, where water moves through the entire volume of the soil, preferential flow occurs only in a small fraction of the soil's total volume. Water flows along preexisting features in the soil such as cavities, fissures or macropores. (Hillel, 2004)

In *unfrozen soils*, water movement may be fast. Under such conditions, the pore size distribution and water content determine the rate of water movement. The water movement in *frozen soils* is generally impeded when the pores are filled with ice. In this

case, the rate of water movement strongly depends on the ice saturation. (Hillel, 2004) In *saturated frozen soils*, two forms of water flow are known. First, it is assumed that water moves through the unfrozen water films on the soil particles. Secondly, water may migrate by the process of regelation, where water freezes at ice lenses which in return partly melt and increase unfrozen water content at the other end. However, movement rates associated with these processes are very low. (Kane and Stein, 1983) In *unsaturated frozen soils* on the contrary, more effective forms of water transport occur if some of the macropores are air filled. These pores may then act as preferential flowpaths, allowing rapid liquid water flow and thus significantly increasing the hydraulic conductivity locally and during short time periods. (Stähli et al., 1996)

Following from this, the ice saturation at the onset of the snow melt infiltration in spring is crucial for the hydraulic conductivity during this time. In general, the saturation of frozen soils reflects the saturation at the onset of freezing in autumn. (Stähli et al., 1996) Alpine soils in particular are well drained and thus usually unsaturated when freezing (Gruber and Haeberli, 2010). In unsaturated frozen state, the smallest pores hold unfrozen water, ice is present in intermediary pores and the largest pores contain air. However, as described before, water tends to move towards zones of freezing. In winter, when the freezing front propagates downwards from the surface, water tends to be redistributed towards the surface. This results in higher moisture and ice contents near the ground surface at the beginning of the melt season in spring. (Kane and Stein, 1983)

2.4.2 Conductive Heat Transfer

The conductive ground heat flow Q_G can be written as (Williams and Smith, 1989):

$$Q_G = -K_t(\delta T/\delta z) \tag{2.4}$$

where K_t is the thermal conductivity (W m^{-1} K^{-1}), T is the temperature and z is the depth. K_t is a measure of the quantity of heat that will flow through a unit area per unit time under a given unit temperature gradient. The negative sign indicates a flow of heat towards decreasing temperatures. This relationship holds true for steady state conditions. In reality however, surface temperatures and ground properties are subject to constant change. Furthermore, the thermal properties are temperature dependent. To account for the temperature change over time, the volumetric heat capacity C (J m^{-3} K^{-1}) is introduced which is a measure for the energy required to heat up a unit volume by 1 K. Given a temperature change dT, the change in heat content is the product of C and dT. (Williams and Smith, 1989)

Following the relationships above, the heat balance of a soil layer results from the heat flowing in balanced by the heat flowing out and the change of heat content of the soil layer (Williams and Smith, 1989):

$$K_t(dT/dz)_{in} = K_t(dT/dz)_{out} + C(dT/dt)dz \tag{2.5}$$

where T is the temperature and z is the depth. If this equation is rearranged and written in differential form, the heat conduction equation can be formulated (Williams and Smith, 1989):

$$\partial T/\partial t = \kappa(\partial^2 T)/(\partial z^2) \tag{2.6}$$

where κ is the thermal diffusivity ($m^2\ s^{-1}$). The thermal diffusivity equals K_t/C and is the coefficient of heat diffusion. A high κ leads to rapid and large temperature changes. (Williams and Smith, 1989)

From these considerations follows, that the thermal regime strongly depends on the thermal properties K_t and C and consequently κ. For steady-state situations, only the thermal conductivity needs to be considered, whereas in transient problems, the thermal diffusivity is important. In the case of phase changes however, the latent heat of fusion is most dominant (see Section 2.4.3). (Williams and Smith, 1989) The thermal properties of different soil constituents and soils with different soil moisture contents are shown in Table 2.1.

From Table 2.1, it is visible that the thermal conductivity of ice is much higher than that of water and air. In the case of unfrozen soils where pores are either filled with water or air, higher water content (less air content) increases the thermal conductivity of the soil. In frozen soils on the contrary, the situation is more complicated: Between 0 and about -3° C the thermal conductivity gradually increases in relation to the decreasing unfrozen water content. Additionally, the mineralogy of a soil determines its overall conductivity. As quartz minerals are more conductive than clay minerals, sandy soils show an overall higher thermal conductivity than clay soils. (Williams and Smith, 1989)

Considering the heat capacity, water can store more heat than ice and even more than air. Consequently, frozen and unfrozen soils differ in their ability to store heat. In the case of unfrozen soils, the heat capacity increases linearly with increasing water content since the heat capacity of water is much greater than air. For frozen soils, the relationship is further complicated by latent heat effects. If a soil is cooled to some point below 0° C, parts of the pore water will freeze and thus release latent heat, which in return has to be removed before further cooling. Since the amount of latent heat released depends on the

Table 2.1: Thermal properties of soils and soil constituents. (Williams and Smith, 1989)

	Density (kg m^{-3})	Mass Heat Capacity (J kg^{-1} K^{-1})	Thermal Conductivity (W m^{-1} K^{-1})	Thermal Diffusivity (10^{-6} m^2 s^{-1})
Soil constituents				
Quartz	2660	800	8.800	4.14
Clay minerals	2650	900	2.920	4.14
Organic matter	1300	1920	0.250	0.10
Water (0° C)	1000	4180	0.560	0.13
Ice (0° C)	917	2100	2.240	1.16
Air	1.2	1010	0.025	20.63
Unfrozen soils				
Sandy soil ($\phi = 40\%$)				
$\theta = 0vol\%$	1600	800	0.30	0.24
$\theta = 20vol\%$	1800	1180	1.80	0.85
$\theta = 40vol\%$	2000	1480	2.20	0.74
Clay soil ($\phi = 40\%$)				
$\theta = 0vol\%$	1600	890	0.25	0.18
$\theta = 20vol\%$	1800	1250	1.18	0.53
$\theta = 40vol\%$	2000	1550	1.58	0.51

amount of water subject to phase change, it is related to the characteristic unfrozen water content curve for a specific soil. Subsequently, the heat capacity is highly temperature dependent and elevated between 0 to -3° C. In contrary to the thermal conductivity, the heat capacity is less variable between different mineralogies. (Williams and Smith, 1989)

The thermal diffusivity reflects the interplay between K_t and C. For unfrozen soils, the thermal diffusivity is dependent on water content: When water is added, diffusivity first increases reflecting a more rapid conductivity increase. When soils are close to saturation, conductivity increases less than heat capacity and thus the diffusivity decreases again. In frozen soils on the contrary, thermal diffusivity is temperature related, especially between 0 to -3° C. In this range, the thermal diffusivity mainly reflects the heat capacity is therefore decreased in this range. (Williams and Smith, 1989)

2.4.3 Non-Conductive Heat Transfer

In mineral soils, non-conductive heat transfer is mainly associated with the movement of water and air within the soil matrix. In this form, heat transfer occurs based on the advection of sensible or latent heat. The relative importance of non-conductive heat transfer

through fluid movement compared to conductive heat transfer then mainly depends on the specific heat of the moving fluid, the velocity of the fluid, the thermal conductivity of the soil as well as on the presence or absence of latent heat effects. (Kane et al., 2001) Due to the relatively low permeability of mineral soils, movement of air in the form of free convection is unlikely to occur in such systems (Kane et al., 2001) as opposed to coarse-grained blocky subsurfaces such as in talus slopes (Delaloye and Lambiel, 2005) or in the active layer of rock glaciers (Gruber and Hoelzle, 2008). Air convection is thus not discussed in the following.

The advection of latent heat is strongly connected to phase changes, which considerably impact the thermal regime of a soil. Energy is released and consumed during freezing and melting (0.33 MJ kg^{-1}), condensation and evaporation (2.50 MJ kg^{-1}), and sublimation (2.83 MJ kg^{-1}). Within the active layer of permafrost soils, latent heat effects are particularly important during periods of thawing (spring) and freezing (autumn). In spring, the melting of pore ice requires additional heat and essentially retards the penetration of warm temperatures in the ground. In autumn, the advance of the freezing front is retarded due to the release of latent heat when pore water freezes up. In both cases, a isothermal region at or near to 0° C is present, referred to as the zero-curtain. Upon the closure of the zero-curtain, rapid penetration of warm or cold temperatures may occur. During summer, near-surface soil water may be evaporated. Evaporation of soil water acts as an energy sink and results in lower soil temperatures. (Kane et al., 2001)

The advection of sensible heat on the contrary, is solely dominant during intense summer precipitation events, as shown for arctic soils by Kane et al. (2001). During snow melt events on the contrary, where water temperature is close to 0° C and infiltration rates are lower, sensible heat advection is negligible.

As most of the studies on non-conductive heat transfer in permafrost soils were conducted in polar regions, only little is known about the effectiveness of these processes in alpine terrain. In contrary to polar areas, alpine permafrost soils usually have no vegetation cover, are characterized by a higher porosity and may be steeply inclined. As a result, hydraulic conductivities are higher and the soils drain faster. Moreover, ground water tables are often absent. (Rist and Phillips, 2005)

From a modelling study by Scherler et al. (2010) in the permafrost soils at the Schilthorn, step-wise temperature increases towards 0° C are reported during spring when the surface is still snow covered. The temperature increase is followed by a relatively long phase of zero-curtain conditions in the uppermost meters. The authors suggest the infiltration of snow melt water and associated transport of sensible and latent heat as the driving processes of this sudden temperature shift. During 2 months, alternating melting and freezing cycles lead to highly variable infiltration capacities. More precisely, the model

data suggests water infiltration until a critical amount of water has refrozen in the top layer, impeding further water inflow. During this time, soil temperatures increase due to the advection of sensible heat and the release of latent heat upon freezing. It is followed by a period of downward conductive heat flow as water flow has stopped and temperatures decrease again. Simultaneously, melt water accumulates at the surface until a critical pressure head is built up which leads to melt of the top soil ice and the onset of a further infiltration period. The soil temperature consequently rises step-wise towards zero-curtain conditions and stays at 0° C until all ice has melted.

Significant snow melt water infiltration into the frozen active layer is reported by Rist and Phillips (2005) for a permafrost site on Muot da Barba Peider (Eastern Swiss Alps). A sharp temperature increase at the beginning of snow melt indicates the dominance of non-conductive heat transfer during this period. Soil moisture increase is delayed and dampened with depth which leads to the highest temperature increase due to water infiltration at the top. The authors suggest increasing infiltration rates as the temperature increases and ice melts. However, the highest infiltration rates are associated with the infiltration along preferential flowpaths.

2.5 Hillslope Hydrology

The runoff generation on slopes and attributed flow regimes may vary greatly over time and depend strongly on the infiltration and retention capacity of soils. In general, four distinct regimes can be differentiated, as visualized in Figure 2.4 (Spreafico et al., 2003):

(a) Overland flow (Hortonian Overland Flow HOF) due to infiltration obstructions may occur on water-repellent or compressed soils.
(b) If soils are saturated or if the precipitation or snow melt rate is higher than the infiltration rate, Saturated Overland Flow (SOF) may occur. The rate of runoff generation then strongly depends on the retention capacity of the soils.
(c) If highly conductive soil layers lie above an impermeable layer or if macropores allow fast lateral flow, Sub-Surface Flow (SSF) occurs.
(d) Water may move to the deep subsurface and be stored through the process of Deep Percolation (DP) if a permeable soil lies above a permeable geological subsurface.

The characteristics of runoff generation and hillslope hydrology are determined by local key elements. For alpine mineral soils without a vegetation cover and limited biotic activity, three key elements are important: First, the bulk density and grain size distribution determine the porosity and consequently the retention and infiltration capacity. Second, fissures or macropores may act as preferential flowpaths and their presence may thus enhance infiltration. Finally, the geological subsurface may be impermeable and lead

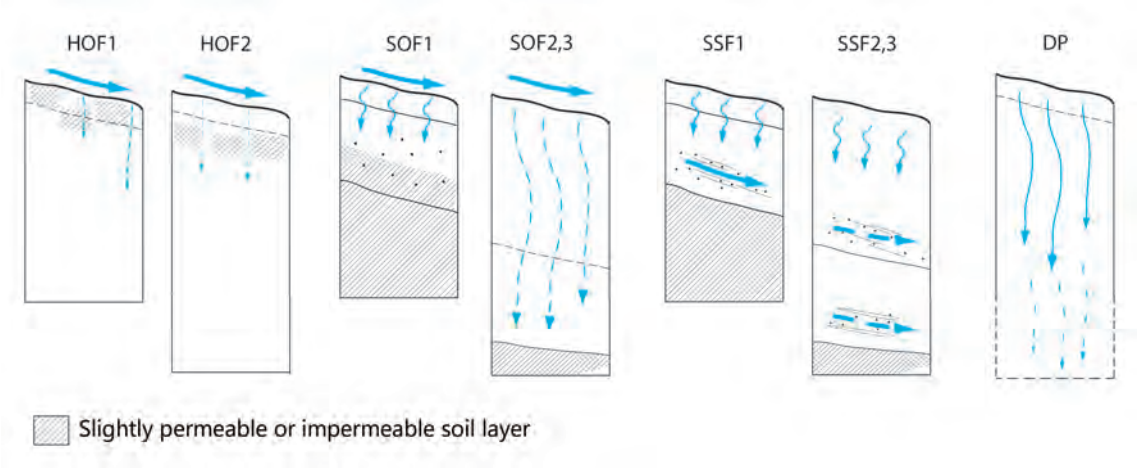


Figure 2.4: Hillslope runoff generation during strong infiltration events. Hortonian Overland Flow (HOF), HOF1 quick, HOF2 delayed. Saturated Overland Flow (SOF), SOF1 quick, SOF2 delayed, SOF3 strongly delayed. Subsurface Flow (SSF), SSF1 slightly delayed, SSF2 delayed, SSF3 strongly delayed. Deep Percolation (DP). (modified after Spreafico et al., 2003)

to saturation which is a condition for lateral flow of water within slopes. (Spreafico et al., 2003)

In mountain permafrost, the permafrost table is generally assumed to be impermeable with respect to runoff generation. Usually, water percolates until the permafrost table where a minor part refreezes but the major part runs downslope along this interface (Rist and Phillips, 2005). For the more gentle slopes in the Arctic, Wright et al. (2009) found that at the beginning of the ground thawing, the subsurface flow is governed by the frost table topography in a similar manner that bedrock topography controls the subsurface flow. During this time, the frost table topography is highly variable over space due to the heterogeneous melt-out pattern of the snow cover. This leads to spatially variable storage of ground water in subsurface depressions of the frost table. Furthermore, overland flow is reported during the snow melt period due to the shallow and saturated active layer. (Boike et al., 1998) Water flow below the frost table is reported from alpine rock glaciers, where internal unfrozen flow channels developed in association with the formation of taliks (Zenklusen Mutter and Phillips, 2012a). The connection of such taliks to the active layer and ability to conduct water may vary over the turn of the year (Arenson et al., 2010).

Chapter 3

Study Area

The study area is located in the northern slope of the Schilthorn summit (2970 m asl, see Figure 3.1). The Schilthorn is situated in the northern Swiss Alps at the transition between the Prealps and the main chain of the Bernese Alps which exceed 4000 m asl. (Hauck, 2001) While the summit is easily accessible via a cable car, the study site is reached by foot and is located on a small plateau beneath the cable car station at about 2900 m asl.

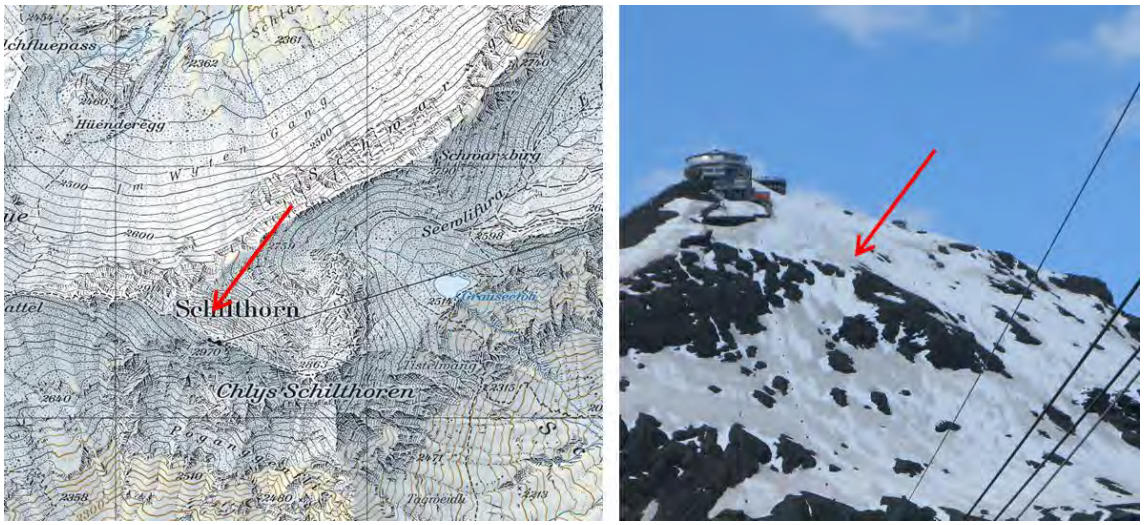


Figure 3.1: Map of the Schilthorn (Bundesgeoportal, 2015) and view from the cable car on the summit area. The red arrows indicate the location of study site (boreholes location).

3.1 Climate

The Schilthorn summit is exposed to moist western winds and exhibits a climate of almost alpine maritime character (Hoelzle and Gruber, 2008). Mean annual air temperature (1999–2008) is -2.6 °C (Scherler et al., 2013). In the summit area, mean annual precipita-

tion is estimated to 2700 mm, most of which falls as snow. Compared to the central Alps, cloudiness and precipitation are higher. (Imhof et al., 2000)

Due to the high precipitation and wind redistribution, maximum snow depths in the northern slope may reach up to 300 cm (Imhof et al., 2000). At the study site, maximum snow depths reach up to 220 cm as measured at the climate station (see Section 5.1). In summer, most of the snow ablates while some isolated snow patches may persist until the onset of winter. However, perennial snow and firn patches have been shrinking considerably since the 1980s. (Imhof et al., 2000)

3.2 Lithology

The lithology at the study site consists of micaceous shales of Mesozoic and early Tertiary age (Glockhaus formation), which were thrusted over the crystalline Aar massif (Imhof et al., 2000). The surface is deeply weathered and partly covered by a layer of debris which is up to 5 m in thickness. However, the depth of the debris cover layer is highly variable over space and at many locations, outcrops of the bedrock appear at the surface. (Hilbich et al., 2008) The micaceous shales decay into fine-grained material and build up a sandy and silty matrix. Soil texture measurements from the surface debris cover inhibit a grain size distribution of 70 % sand, 18 % silt and 9 % clay and a porosity of 54 %. Such thick layers of relatively fine-grained debris are uncommon for alpine permafrost sites and effect in a relatively high retention capacity. Nevertheless, infiltration water, which is mostly present in the summer months, drains fast. (Scherler et al., 2010) The underlain bedrock is strongly weathered and highly fractured. It is assumed that in the fractures and crevices, water can easily percolate. (Noetzli et al., 2008)

3.3 Permafrost

In the following, the permafrost measurement setups and the permafrost characteristics at Schilthorn are presented.

3.3.1 Measurements

First permafrost occurrence in the form of ice lenses was encountered when the cable car station was built in the 1960s (Hauck, 2001). After the site was chosen to be part of the European PACE project (Permafrost and Climate in Europe), two vertical boreholes of 14 m and 101 m depth (hereinafter referred to as SCH5198 and SCH5000) as well as an inclined borehole of 100 m depth (SCH5200, inclination 60° to the vertical) were drilled

in 1998 and 2000 in the north facing slope. Later on, they were incorporated in the Swiss permafrost monitoring network PERMOS (Permafrost Monitoring in Switzerland) allowing for continuous ground temperature measurements. (Vonder Mühll et al., 2004; Hauck, 2001) SCH5198 is uninsulated, whereas SCH5000 and SCH5200 are insulated with a PVC-pipe. All three boreholes are protected from water infiltration with a cap and the temperature is measured by thermistor chains. (Scherler et al., 2010) The site furthermore includes measurements of meteorological parameters (air temperature, snow depth, net radiation, relative humidity, wind speed/direction). (Vonder Mühll et al., 2004)

In addition, a permanent ERT monitoring line was installed in 1999 in proximity of the three boreholes to measure water and ice content distribution along a two-dimensional profile in the uppermost 10 m (hereinafter referred to as SCH). The 58 m long profile runs horizontally (E-W-oriented), consisting of a set of 30 electrodes of 2 m spacing. (Hauck, 2002) In 2006, the ERT monitoring profile was complemented with an additional N-S-oriented profile line running across the Schilthorn crest (hereinafter referred to as SCV). It is 164 m long, has an electrode spacing of 4 m, reaches 25 m in depth and covers both the south and north facing slope. (Noetzli et al., 2009) Both profile lines were incorporated in the PERMOS network in 2005 and up to 10 measurements per year were conducted since then. In 2009, the E-W-oriented profile was automated, allowing for daily measurements throughout the year. It was further extended to 49 electrodes in 2012. Soil moisture sensors (SISOMOP, (Krauss et al., 2010)) were installed in 2007 at two locations along the SCH profile line, allowing for continuous measurements of volumetric soil moisture and soil temperature at various locations in the uppermost 60 cm (Hilbich et al., 2011). In summer 2014, additional soil moisture sensors (SMT-100, PICO64) were installed near the boreholes (Pellet et al., 2015). The setup of the soil moisture sensors is described in more detail in Section 4.2.

3.3.2 Permafrost Characteristics

The borehole temperatures confirm that the permafrost extends to more than 100 m depth. However, the temperature is comparatively high and close to 0 °C throughout the borehole profiles. (Harris et al., 2003) The active layer is relatively thick ranging from around 5 to almost 10 m in depth. At SCH5198, maxima of 8.6 and 9.9 m were reached in the exceptionally warm summers of 2003 and 2015, respectively. (PERMOS, 2015) Generally, resistivity values at Schilthorn are relatively low compared to other locations. This is attributed to both the presence of fine-grained material and the relatively low ice content (temperatures near the freezing point). (Hauck, 2002) The low ice contents were confirmed during the drilling of SCH5198, where no ice lenses were encountered (Vonder Mühll et al., 2000). At Schilthorn, the resistivities are very sensitive to interannual changes in

weather conditions and ERT measurements showed remarkably low ice contents in the warm summers of 2003, 2009 and 2010. It is assumed, that the permafrost at Schilthorn inhibits a great potential for degradation. (Noetzli, 2013)

Modelling of the subsurface temperature field along a north-south cross section of the Schilthorn summit and the comparison with resistivity data of the SCV profile line revealed that the subsurface thermal regime is largely influenced by topography and transient effects. Specifically, three zones of different thermal and resistivity characteristics can be distinguished (see Figure 3.2). In the northern slope, a zone of lower temperatures and lower resistivities (lower ice content) exists around the boreholes (A). Further upslope, subsurface temperatures decrease and resistivities increase (higher ice content, B). Just below the crest, isotherms are steeply inclined, indicating a lateral flow of heat from the warm south side to the north side. It is assumed that permafrost is not present near the surface of the south slope. (Noetzli et al., 2008)

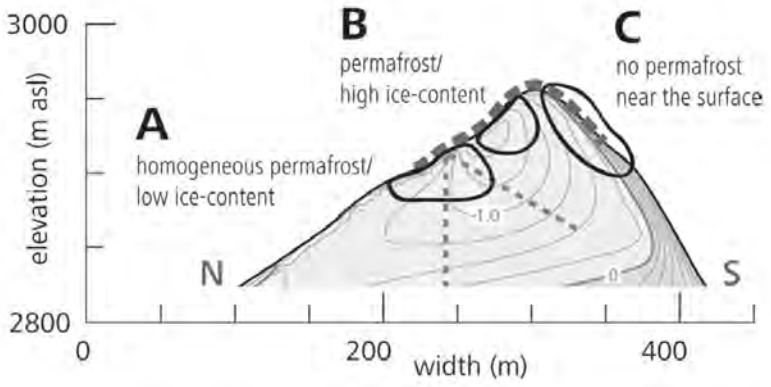


Figure 3.2: 2D profile for a north-south cross section of the Schilthorn summit. The Isotherms are a modelled subsurface temperature field and the three zones A, B and C delimit regions of specific temperature and resistivity characteristics. (Noetzli et al., 2008)

3.4 Energy Balance Components

Monthly averages of the energy balance at Schilthorn are shown in Figure 3.3 (Hoelzle, October 28, 2015, pers. communication). Clear seasonal variations are visible for all energy balance components. Net radiation is negative in winter and only for a short time, while in summer, it reaches up to 150 W m^{-2}. The reverse is visible for the sensible and latent heat flux, however at a smaller scale. Both are a major heat sinks in summer. The heat flux through the snow cover is generally small, owing to its insulating effect. The melting of the snow cover consumes most energy in spring but it is small as well. The resulting ground heat flux is negative in winter and positive in summer.

The year-to-year variability in the net radiation is small in summer but higher in winter. However, individual months can show quite large deviations. While the variability of the heat flux through the snow cover is quite small, it is higher for the heat flux produced by the melt of the snow cover, reflecting annual snow depth variations. Both the sensible and latent heat flux can vary considerably in both winter and summer. The ground heat flux is rather homogeneous, but some single years show large deviations.

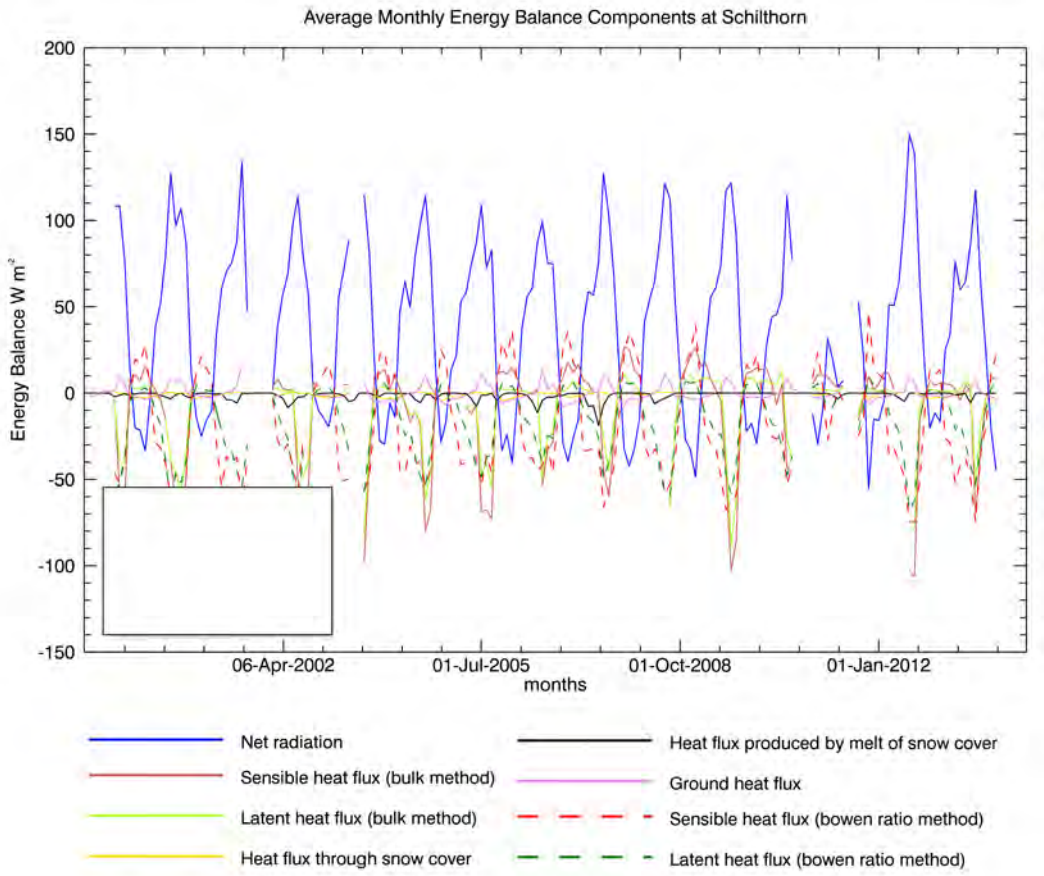


Figure 3.3: Monthly values of the energy balance components at Schilthorn from summer 1999 to winter 2013. (Hoelzle, October 28, 2015, pers. communication)

Chapter 4

Methods

In this chapter, the methods and approach used in this work are outlined. First, an overview of the ERT measurements is given. It is followed by the presentation of the soil moisture measurements and the measurements of the meteorological parameters. Finally, the approach for the runoff modelling is presented. Figure 4.1 shows an overview of the locations of the measurements.

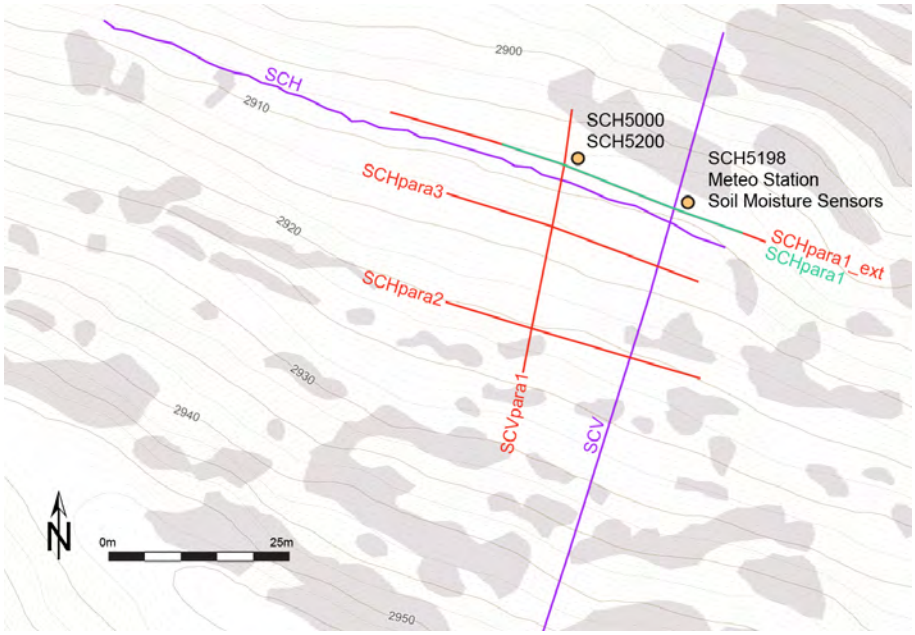


Figure 4.1: Overview of the measurement instruments in the study area. The grey patches show outcrops at the surface.

4.1 Electrical Resistivity Tomography

In this Section, the general principles of the electrical resistivity tomography (ERT), its application in permafrost studies and the measurement setup for this study are explained in more detail.

4.1.1 General Principles

In resistivity surveys, the material's ability to conduct electricity is measured. If a cube of electrically homogeneous material is considered, the material resists the conduction of electricity and results in a potential drop between the two sides. The resistance R (Ω) of the block is as following: (Reynolds, 2011)

$$R = \rho \frac{L}{F} \tag{4.1}$$

where ρ is the true resistivity of the block's material (Ωm), L is the block's length (m) and F is the area of the block's cross section (m^2). Ohm's law describes the resistance as following: (Reynolds, 2011)

$$R = \frac{\Delta V}{I} \tag{4.2}$$

where ΔV is the potential drop (V) between the two sides of the block and I is the applied electric current (A). If Equatins 4.1 and 4.2 are combined, the true electrical resistivity is defined as following: (Reynolds, 2011)

$$\rho = \frac{F}{L} \cdot \frac{\Delta V}{I} \tag{4.3}$$

In resistivity measurements, as visible for a typical four-electrode configuration in Figure 4.2, a direct electrical current is injected into the ground via two current electrodes (A and B) and the voltage difference is measured at two potential electrodes (M and N). The apparent resistivity ρ_a is calculated with the following equation (Hauck and Kneisel, 2008)

$$\rho_a = G \frac{\Delta V}{I} \tag{4.4}$$

where G is a geometric factor depending of the arrangement of the four electrodes. The apparent resistivity at a specific location corresponds to the true resistivity which is altered

by the resistivity of upper lying soil layers (in an electrically heterogeneous subsurface). The true resistivity value, referred to as the specific resistivity, can then be derived using inversion methods (see below).(Hauck and Kneisel, 2008)

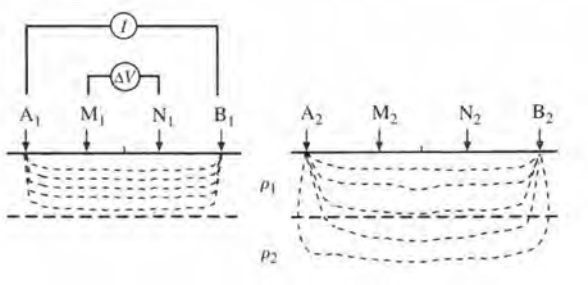


Figure 4.2: Typical four-electrode configuration in resistivity measurements. (Hauck and Kneisel, 2008)

Three ways of electrical conduction in the ground are possible. Through *electrolytic conduction*, ions move relatively slow within an electrolyte. The conduction depends on the type of ion, ionic concentration and mobility. Secondly, metals for example, allow electrons to move rapidly through the process of *electronic conduction*. Third, in very weakly conducting materials (insulators), *dielectric conduction* occurs, in which atomic electrons are shifted slightly with respect to their nuclei. In most subsurface materials, the electrical conduction takes place within the pore fluids through electrolytic conduction. The actual mineral grains contribute only little to the overall conductivity. (Reynolds, 2011)

From an electrode planted in an electrically homogeneous subsurface, the current flows away radially in all directions and thus covers a hemisphere. The voltage drop between two points at the surface depends on the resistivity of the host material and is described by the potential gradient $(-\delta V/\delta x)$. Lines of equal current intersect lines of equal voltage ('equipotentials') at right angles. In resistivity surveys, where a current sink is deployed, they appear as in Figure 4.3. (Reynolds, 2011)

The electrical resistivity of different geological materials may vary considerably as shown in Table 4.1. This effect allows the identification of different layers of rock material in the subsurface. Furthermore, the electrical conductivity of the subsurface may be considerably altered through the presence of water, ice or air, depending on the presence and the volume of pores or cracks. As for sedimentary rocks, it is assumed that the resistivity of the fluids which is present in the pores is more important than the resistivity of the host material itself. Consequently, sediments and sedimentary rocks have typically lower resistivity values than igneous or metamorphic rocks. (Reynolds, 2011) Furthermore, when pore fluids are present, resistivity strongly depends on the water saturation, the chemical properties of the pore water, the structure of the pore volume and the temperature (as unfrozen water content is temperature dependent) (Hauck and Kneisel, 2008).

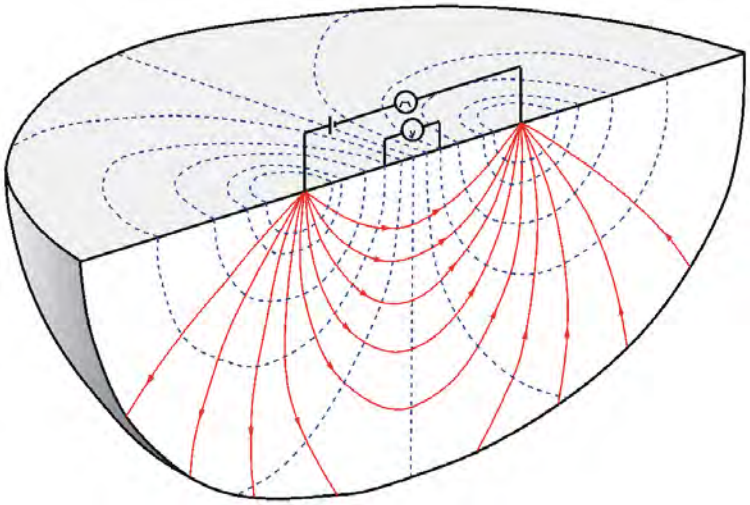


Figure 4.3: Lines of equipotential (blue) and equal current (red) between two current electrodes. (TRICON Geophysik und Systemtechnik GmbH, Munich, 2015)

Table 4.1: Resistivity ranges in different geologic materials. (Hauck and Kneisel, 2008)

Material	Range of resistivity (Ωm)
Clay	1–100
Sand	100–5×10^3
Gravel	100–400
Granite	5×10^3–10^6
Gneiss	100–10^3
Schist	100–10^4
Groundwater	10-300
Glacier ice (temperate)	10^6–10^8
Air	infinity
Frozen sediments, ground ice, mountain permafrost	10^3–10^6

From this relationship, the unfrozen water content of a subsurface can be determined with the following empirical formula, developed by Archie (1942):

$$\rho = a\phi^{-m}s^{-n}\rho_w \tag{4.5}$$

where ρ is the effective resistivity of a two-phase medium (rock matrix and liquid), ρ_w is the resistivity of the pore water, ϕ is the porosity and s is the fraction of the pore space occupied by liquid water. a, m and n are empirically derived parameters. If the resistivity of the pore water and the porosity are known and if the factors a, m and n are determined, the unfrozen water content can be derived from resistivity measurements (Hauck, 2002). However, the interpretation of resistivities in terms of water content can be a difficult task

as it is quite sensitive to the porosity value which is difficult to assess and may be very heterogeneous over space (Brunet et al., 2010).

4.1.2 Measurement Configurations

The spacing between the current electrodes (A and B) determines the penetration depth d. Thereby, if informations about deeper layers are to be obtained, the distance between A and B is to be increased. Consequently, the maximum penetration depth is limited by the maximum electrode spacing which has practical implications, particularly if very deep soil layers are to be measured. (Reynolds, 2011)

In order to obtain a two dimensional picture of the subsurface to account for an inhomogeneous subsurface, two-dimensional electrical resistivity tomography (ERT) is applied, where multi-electrode systems and two-dimensional data inversions may produce accurate models of the underground. In this approach, the geometry of the current and potential electrodes is varied to cover a set of measurement points of a two-dimensional profile. (Hauck and Kneisel, 2008) This variable geometry is represented by the geometry factor G (see Equation 4.4). A multitude of array types is recognised, only few of which are often applied. (Reynolds, 2011) The following array types are most common (see also Figure 4.4).

(a) In the Wenner array, the two outermost electrodes work as the current electrodes whereas the potential electrodes are located in between them. The spacing between each electrode is equal for each measurement (a). The Wenner array is best suited to resolve horizontal structures that change with depth. It has a medium depth of investigation and a relatively small number of measurements is necessary (however less information is collected). (Hauck and Kneisel, 2008)

(b) In the Wenner-Schlumberger array, the current and potential electrodes are arranged equally to the Wenner array. However, while the potential-electrode spacing stays constant (a), the current-electrode spacing is increased as an integer n multiple of the potential-electrode spacing. It allows for a better in-depth resolution than the Wenner array and is best suited to conduct both horizontal and vertical geological structures. It is seen as a compromise of the Wenner and Dipole-Dipole array. (Hauck and Kneisel, 2008)

(c) The Dipole-Dipole array has two dipoles on each side formed by the current and potential electrodes. While the current and potential spacings stay the same (a), the spacing between the dipoles is an integer n multiple of the first. The horizontal resolution is better than that of the previous arrays, however the depth of investigation is shallower. It has the largest number of measurements required. (Hauck and Kneisel, 2008)

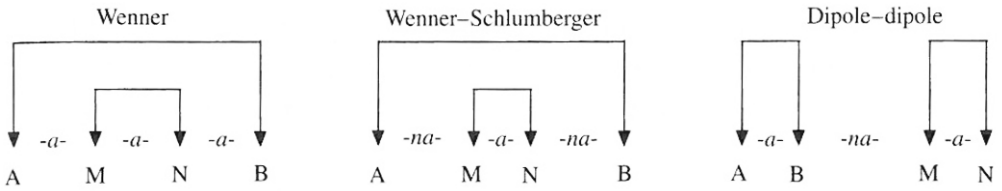


Figure 4.4: Schematic overview of the Wenner, Wenner-Schlumberger and Dipole-Dipole Arrays where a is the potential-electrode spacing and n is an integer multiplier of a. (Hauck and Kneisel, 2008)

An ERT imaging survey typically consists of 100 to several 100 measurements. The use of multi-electrode systems allows for automatic measurements of the different electrode combinations (also referred to as quadripoles). With a multi-electrode system and for an ERT data set of about 40 electrodes, between 0.5 and 1.5 hours are needed to acquire the full data set, depending on the array type and the number of required repetitions of a single combination. (Hauck and Kneisel, 2008)

4.1.3 The Inversion Problem

In order to deduct specific resistivities for an ERT data set, the apparent resistivity data set needs to be processed with an inversion algorithm. Since the growth in available computer resources in the 1980s, such inversion algorithms have become widely available and are able to produce 2D and 3D images of the subsurface. (Binley et al., 2015) In general, the inversion process aims at finding a model of the specific resistivities of the subsurface which produces similar responses (apparent resistivities) as the actually measured values. Ultimately, the inversion process iteratively adapts an initial model the specific resistivities of the subsurface until its response (apparent resistivities) agrees well with the data that was measured. Thereby, a well known problem is the non-uniqueness of resistivity modelling: A wide range of models may correspond well to the measured data. To counteract this, assumptions about the nature of the subsurface can be incorporated in the inversion process (e.g. whether the subsurface has sharp or gradual boundaries). (Loke, 2001)

A widely applied resistivity inversion software is RES2DINV/RES3DINV (Geotomo Software). The inversion algorithm produces 2-D and 3-D model sections of specific resistivities. (Loke, 2001) Furthermore, the effect of topography on resistivity measurements is accounted for in the inversion process, which makes it valuable for the application in mountainous terrain. Prior to the inversion, it is further possible to manually eliminate single measurement points with unusually high or low resistivity values which are usually due to measurement errors or bad electrode contact. (Hauck and Kneisel, 2008)

Initially, a starting model is calculated using the logarithm of the measured apparent resistivity values. From this starting model, a set of apparent resistivities is calculated, as how they would be measured in the field. Iteratively, the algorithm subsequently tries to minimise the differences between the observed and the calculated apparent resistivity values for each model block by adjusting their resistivity values. The difference between model and observed values is calculated by the root-mean-square (RMS) error for the whole profile. The inversion process is stopped after the discrepancies do not alter significantly between two inversion steps or if they become smaller than the measurement accuracy. (Hauck and Kneisel, 2008)

4.1.4 Application of ERT

ERT has been widely applied in various fields of research (Daily et al., 2004). Advantages of ERT and to some extent of geophysical methods in general are amongst others that they provide information on the spatial distribution of physical properties of the subsurface on a variety of different scales in two as well as three dimensions. Furthermore, ERT is particularly well suited to monitor changes in these properties through the application of time-lapse inversion schemes, where the inversion is conducted simultaneously for a whole set of measurements and differences between them are related to properties changes. Finally, the application of ERT methods is non-invasive and measurements are conducted rapidly, in a big area and at comparatively low costs. (Kneisel et al., 2008)

In periglacial environments, ERT is used to measure ground ice, as the physical properties of pore ice differ from those of pore water or air. ERT is typically applied to assess the presence, the spatial distribution and origin of the ground ice as well as the volumetric ice content of the subsurface. Furthermore, the temporal evolution of permafrost can be assessed using time-lapse inversion schemes. In this context, resistivity surveys are a cost-efficient method to complement temperature measurements in boreholes and to assess spatial information. (Kneisel et al., 2008) In alpine permafrost research, ERT has proven to be reliable in detecting the change in active layer thickness for both seasonal and annual variations and to reflect the subzero unfrozen water content (e.g. Hauck, 2002), to detect long-term ground ice degradation (e.g. Hilbich et al., 2008), as well as to measure changes in the water saturation in relation to infiltration events (Hilbich et al., 2011).

In hydrology, ERT is mainly used to assess water content and pore water conductivity. In contrary to traditional measurement methods, where soil properties are sampled at point locations typically through the recovery of samples and by apparatus that sample the pore fluids, ERT assesses soil properties on a larger scale (spatial information), in higher depths and in a non-invasive manner. (Kneisel et al., 2008) It has been used to assess water contents and small scale hydrological processes related to infiltration and water

movement in both frozen and unfrozen ground (e.g. Daily et al., 1992; French et al., 2002; Binley et al., 2002; French and Binley, 2004; Slater et al., 1997) and to study hillslope water movements (e.g. Brunet et al., 2010).

4.1.5 Measurement Setup

The locations of the measured profile lines is visible on Figure 4.1 and an overview of the individual profile lines is given in Table 4.2. ERT measurements were conducted manually along five profile lines, four of which are parallel to the A-ERT profile line SCH (therefore SCHpara), and one of which is parallel to the vertical profile line SCV (therefore SCVpara). SCHpara1_ext is an extension of the SCHpara1 profile line. During the study period, the SCV profile line was not working due to technical problems and could thus not be included in the analysis.

Table 4.2: ERT measurements conducted in 2014.

Name	Number of Electrodes	Spacing [m]	Topography	First Measurement	Number of Measurement
SCH	49	2	No	2014-07-31	93
SCV	44	4	Yes	No meas. in 2014	
SCHpara1	48	0.8	Yes	2014-08-02	6
SCHpara1_ext	72	0.8	No	2014-08-25	2
SCHpara2	48	0.8	Yes	2014-07-31	10
SCHpara3	48	0.8	Yes	2014-08-20	5
SCVpara1	48	0.8	Yes	2014-08-20	6

All SCHpara and SCVpara profiles have a spacing of 0.8 m in contrast to SCH (2 m) and SCV (4 m). This spacing was chosen in order to be able to reproduce small scale hydrological processes. With 48 electrodes, the profile lines are 37.6 m in length (56.8 m for SCHpara1_ext). The depth of investigation of approximately 6 m is considered enough to cover infiltration events. In contrast, SCH has 49 electrodes which amounts to a profile length of 96 m and a depth of investigation of approximately 10 m. The spatial resolution is therefore coarser. Topography was measured and included in the inversion process for all profile lines except for SCH and SCHpara1_ext.

The SCHpara and SCVpara profiles were measured manually using a SYSCAL Junior multi-electrode resistivity meter (IRIS Instruments). Electrode contacts to the ground were generally good, therefore no measures to improve the contacts had to be undertaken. Measurements were conducted repeatedly during four field campaigns of each 3 to 5 days in summer 2014. The A-ERT profile in contrary is measured automatically using a Geotom multi-electrode resistivity meter (Geolog2000). An external computer situated at the cable

car station Birg (2677 m asl), which is connected to the resistivity meter via radio, controls the measurements. (Hilbich et al., 2011) In summer 2014, the SCH profile line was measured daily at 08:00 h (the very first measurement was conducted at 16.00 h). They were conducted daily from the 31st of July to the 22nd of October 2014 and on an irregular basis thereafter. All ERT measurements were conducted using a Wenner-Schlumberger array, as it resolves well both vertical and horizontal subsurface structures. Vertical contrasts are expected due to a seasonally varying infiltration depth, whereas horizontal contrasts are expected due to the presence of preferential flowpaths and preferential flow downslope.

The apparent resistivities of the SCHpara and SCVpara profiles were inverted in RES2DINV using a time-lapse inversion scheme. Initially, bad datum points (spikes in the apparent resistivities) were removed manually. Inversions were conducted simultaneously for each profile line using a robust smoothness constraint. To account for small scale hydrological processes, the model was refined to half width unit spacing and a moderate damping parameter was chosen.

At SCH in contrary, due to the automatic conduction of the measurements, no initial tests of the electrode contacts were performed. Therefore, the apparent resistivities were filtered and de-spiked before the inversion process, using an automated algorithm. (Hilbich et al., 2011; Rosset et al., 2013) The resulting apparent resistivities were then inverted individually in RES2DINV using the standard settings for the A-ERT profile line with a robust inversion constrain. To account for smaller scale processes, the model was refined to half width unit spacing.

This methodology, particularly the spatial arrangement and setup of the profile lines, the timing of the measurements and the specific inversion procedures, allows for the following analyses thereafter:

- Different conditions in snow cover (spatial distribution, snow depth, snow melt intensity), meteorology (air temperature, precipitation, cloudiness) and soil moisture (degree of saturation) were covered and thoroughly documented. Furthermore, measurements were conducted at different stages of the advancing thaw depth. Resistivity changes can thus be attributed to specific infiltration events, particular soil moisture conditions or the thawing of the subsurface.
- The spatial arrangement of the profile lines was chosen to cover different geological conditions (variability in the loose debris cover thickness, areas of blocky surface material, areas near or above outcrops) in order relate hydrological processes to the geological setting.
- The alignment of the profile lines allows for the detection of possible lateral preferential flowpaths downslope.

- The profile lines SCH, SCHpara1, SCHpara1_ext and SCVpara1 run near the ground temperature boreholes, which allows for a relation of temperature change to resistivity change.
- A comparison of SCH and SCHpara1/SCHpara1_ext may reveal differences in the resistivity tomograms due to the different spatial resolution.

4.2 Soil Moisture Measurements

This section describes the in-situ measurements of soil moisture. First, the measurements by the soil moisture sensors are presented, followed by the soil sampling.

4.2.1 Soil Moisture Sensors

An overview of the available data in the study area is shown in Table 4.3. The locations of the soil moisture sensors as well as the installation depths of the soil moisture sensors at SM1 are shown in Figure 4.5. Two different sensor types (FDR/TDR) within two measurement networks are available. The soil moisture sensors provide information on the point scale and only for the uppermost soil layers. However, they have a high temporal resolution and are a valuable data source for the investigation of temporal changes in the soil moisture content.

Table 4.3: Overview of the available soil moisture sensor data.

Location	Name	Type	Depths [cm]	Resolution	Data Availability
SM1	SMT100	FDR	10, 30, 50	30 min	2014-07-31 to 2014-12-31
					No data for 30cm in 2014
SM1	PICO64	TDR	10	30 min	2014-07-31 to 2014-12-31
SM2	SISOMOP	FDR	20, 40	10 min	2007-08-21 to 2014-03-21
SM3	SISOMOP	FDR	12, 36, 60	10 min	2007-08-21 to 2014-03-21

The SMT100 and SISOMOP (Simplified Soil Moisture Probe) sensors measure soil moisture contents on the basis of the frequency-domain reflectometry method (FDR). The sensor is made up of a ring oscillator based on a digital inverter, which drives a transmission line. A signal is sent along the transmission line, which is fed into the digital inverter again. The frequency of the oscillation strongly depends on the surrounding ground material and its water content. Higher soil moisture contents result in lower frequencies, as the higher dielectric permittivity of the water lowers the wave propagation velocity. In order to relate the dielectric constant to true soil moisture values, the sensor needs to be calibrated to a specific subsurface. (Krauss et al., 2010) The accuracy of the SMT100 and SISOMOP sensors are $\pm 0.03\ m^3/m^3$ (Schlaeger et al., 2005; Truebner, 2012). The sensors were

calibrated to the conditions at Schilthorn which improved the accuracy to $\pm 0.01\ m^3/m^3$ (Pellet, December 17, 2015).

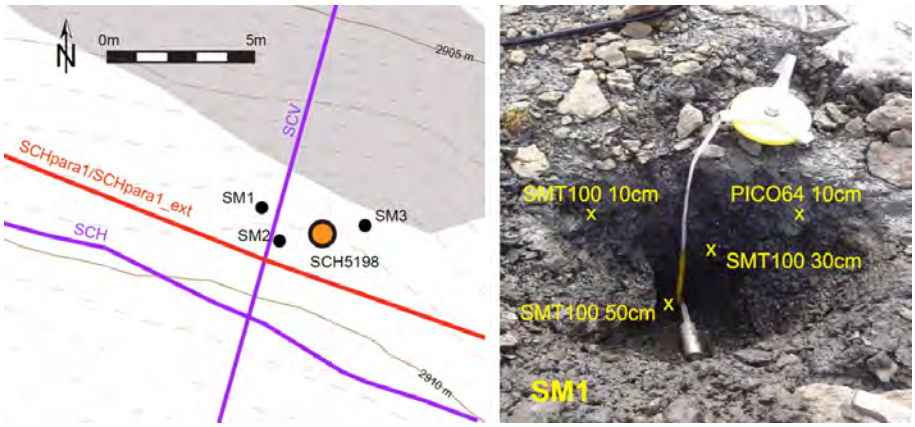


Figure 4.5: Map of the soil moisture sensor locations (SM1, SM2 and SM3, left) and installation depths of the soil moisture sensors at SM1 (Pellet, 2014).

The PICO64 sensor in contrary measures soil moisture contents with the time-domain reflectometry method (TDR). In this method, a pair of parallel metal rods is inserted into the soil. A step voltage pulse is sent along the parallel transmission lines and the signal is reflected from the ends of the metal rods. The time between sending and receiving the reflected signal is then measured. For a given length of the rods, the time interval is inversely related to the propagation velocity of the signal in the soil. Water has a particularly high dielectric constant (ε=80), as opposed to air (ε=1) or dry soil (ε=4), which permits the signal to propagate into the soil at a lower velocity. As a result, higher soil water contents lead to a higher time interval. The variation in the dielectric constant of a soil mainly depends on the soil water content. Therefore, usually no calibration of the sensor is needed. (Hillel, 2004) The accuracy of the PICO64 sensor is ± 0.01–$0.02\ m^3/m^3$ below 40% volumetric soil moisture content (IMKO, 2011).

The SISOMOP sensors were installed in 2007 at two adjacent locations in different depths of the uppermost 60 cm (Hilbich et al., 2011). The SMT100 and PICO64 sensors were installed within the SOMOMOUNT project as a replacement for the SISOMOP sensors (Pellet et al., 2014). The four sensors were installed in vicinity of the SISOMOP sensors at three different depths within the uppermost 50 cm.

In order to measure near surface soil moisture content at various locations, a mobile soil moisture sensor (ThetaProbe) was used. The ThetaProbe works on the basis of the TDR method. It is put directly in the soil and volumetric soil moisture can be measured instantly. Errors (usually an underestimation) arise if the probe is not inserted completely or if it is not completely surrounded by soil (e.g. when a small rock is hit and pushed downwards). Particularly at Schilthorn, where a the sandy soil inhibits lots of small rocks,

this is a problem. The accuracy of the ThetaProbe is $\pm 0.05\ m^3/m^3$. (Delta-T Devices, 2011)

The relation between dielectric constant and soil moisture is based on empirical data collected in many different soils (see Topp et al., 1980: "Electromagnetic Determination of Soil-Water Content - Measurements in Coaxial Transmission-Lines"). The TDR method can also be calibrated but by its mode of operation it is more accurate than the FDR.

4.2.2 Soil Samples

The gravimetric soil moisture content can be determined by sampling a specific volume of soil and measuring its moist weight after sampling and its dry weight after it was dried in an oven at 105° C for 24 hours. It is the only method to measure soil moisture content directly. The gravimetric soil moisture w is determined as following: (Hillel, 2004)

$$w = \frac{(\text{wet weight}) - (\text{dry weight})}{\text{dry weight}} \tag{4.6}$$

Furthermore, when the volume of the sample is known, the volumetric soil moisture θ can be inferred as follows (Hillel, 2004):

$$\theta = w\ \frac{\text{dry weight}}{\text{ring volume}} \tag{4.7}$$

As such, the gravimetric method is quite simple, yet it is laborious and time consuming. Furthermore, errors might occur at different working steps: When the sample is taken, attention needs to be given not to destroy its matrix (to retain the original volume and soil moisture content), which is quite difficult. The bag in which it is transported must be sealed sufficiently, in order to not lose moisture during the process of transport and storage. Finally, some water may still be present after drying, particularly for certain clays. If organic matter is present, it may be oxidized and decomposed during the drying process which adds to the weight loss. (Hillel, 2004)

For the present study, soil samples were taken and analysed in the laboratory as following:

(1) Preparations: The plastic bags for transport are weighted and labelled.
(2) Sampling: A suitable location for sampling is chosen (loose debris, not too many rocks). The sample cylinder is carefully pressed into the ground using a hammer. It is dug out and excessive soil at both cylinder ends is removed. The sample is completely removed from the cylinder and put in the plastic bag. Air is pressed out of the bag and it is sealed air-tight.

(3) Transport and Storage: Already in the field, the bag is put into a bigger transport bag to protect it from direct sunlight. It is transported to the institute within the next few days and stored in a cupboard.
(4) Drying preparations: Empty trays for the samples are labelled and weighted. The wet samples in the bags are weighted and completely emptied in the trays. The empty bags and the filled trays are weighted.
(5) Drying: The filled trays are put in the oven and dried at 105° C for 24 hours.
(6) Weighting: The filled trays with the dried samples are weighted and stored in the cupboard.

4.3 Meteorological Measurements

In this section, the measurements of the meteorological and snow properties are presented. Table 4.4 shows the meteorological parameters that were used for the analysis, listing the corresponding measurement method and data gaps in 2014.

Table 4.4: Overview of the meteorological data and corresponding data gaps in 2014.

Parameter	Sensor	Resolution	Missing Data
Air temperature (on site)	PT-100 Probe	1 hour	2014-09-19–2014-12-31
Snow depth (on site)	Ultrasonic Distance Sensor	1 hour	2014-07-25–2014-10-06
Precipitation (MeteoSwiss)			
Mürren (MUE)	Pluviometer	1 day	
Lauterbrunnen (LTB)	Pluviometer	1 day	
Interlaken (INT)	Pluviometer	1 hour	

4.3.1 Air Temperature and Snow Depth

At the location of SCH5198, a meteorological station records air temperature and snow depths. Air temperatures are measured hourly with a PT-100 probe in 2 m height. Snow depths are recorded hourly at the meteorological station using an ultrasonic distance sensor. Both instruments have gaps in the records of 2014. As the missing records of the snow depth measurements are limited to the summer months (mid-July to the beginning of October) and the analysis of the snow data is crucial during the spring snow melt, the data gap is not problematic. The air temperature records in contrary are missing from mid-September until the end of 2014, which is problematic for the interpretation of autumn meteorological events and freezing of the subsurface. Furthermore, the GERM simulation depends on complete time series of air temperature.

Therefore, the gaps in the temperature records are extrapolated from the MeteoSwiss climate station at Jungfraujoch (3580 m asl, distance 11.2 km), for which hourly temperature records are available. A simple regression analysis of the daily air temperatures for the period of July 1999 to September 2014 held following relationship:

$$T_{SCH} = 0.9874 \cdot T_{JUN} + 4.0174 \tag{4.8}$$

where T_{SCH} and T_{JUN} are the air temperatures (K) at Schilthorn and Jungfraujoch, respectively. The relationship holds a R^2 value of 0.9029, therefore explaining 90 % of the variability at Schilthorn. There were only few outliers in the records. They were recorded in the winter and are probably due to atmospheric inversion effects.

4.3.2 Precipitation

In contrary to air temperature, no precipitation is measured at the study site. Precipitation is needed for the interpretation of infiltration events and to run the runoff model. Therefore, daily precipitation sums are extrapolated from the MeteoSwiss climate stations Mürren (elevation 1645 m asl, distance 4 km) and Lauterbrunnen (elevation 818 m asl, distance 7 km) to the elevation of the study site (2900 m asl) using the following equation: (Mittaz et al., 2002)

$$P = P_{SCH} - \left[\frac{P_{SCH}}{P_{sumSCH}}(h_{SCH} - h) \cdot 0.31233\right] \tag{4.9}$$

where P is the precipitation at the reference climate station, P_{SCH} is the precipitation at Schilthorn, P_{sumSCH} is the annual precipitation sum at Schilthorn (estimated to be 2700 mm), h_{SCH} is the elevation of the study site and h is the elevation of the reference climate station. The factor of 0.31233 was determined by a mean increase function which was derived from an extrapolation of precipitation sums at Lauterbrunnen, Mürren and Kleine Scheidegg in October 1996 to September 1997 (Mittaz et al., 2002). In order to obtain hourly precipitation sums, the extrapolated daily sums from Mürren and Lauterbrunnen are scaled to hourly sums of the MeteoSwiss climate station in Interlaken (elevation 577 m asl, distance 13 km).

4.3.3 Snow Distribution

Spatial snow distribution in the area upslope the boreholes was mapped from photographs which were taken in the summit area. Photographs were taken on the 3rd of July, the 17th of July, the 1st of August and the 25th of August 2014. The mapping was conducted

manually, using prominent reference points and outcrops as a guidance. The spatial snow distribution map was used to interpret spatial differences in thaw and snow melt patterns.

4.4 Borehole Temperature Measurements

Ground temperatures are measured in three boreholes (see Figure 4.1) at two locations. While SCH5198 and SCH5000 were drilled perpendicular to the horizon, SCH5200 was drilled perpendicular to the slope (at 60° to the vertical). Temperatures are measured by NTC thermistors at 2-hour resolution. The sensor depths and data gaps of each borehole in 2014 are shown in Table 4.5.

Table 4.5: Overview of the boreholes ground temperature measurements and corresponding data gaps in 2014. (Vonder Mühll et al., 2004)

Borehole	Missing Data	Sensor Depths [m]
SCH5198		0.2, 0.4, 0.8, 1.2, 1.6, 2.0, 2.5, 3.0, 3.5, 4.0, 5.0, 7.0, 9.0, 10.0, 11.0, 13.0, 13.7
SCH5000		0.2, 0.4, 0.8, 1.2, 1.6, 2.0, 2.5, 3.0, 3.5, 4.0, 5.0, 7.0, 9.0, 10.0, 11.0, 13.0, 15.0, 20.0, 25.0, 30.0, 40.0, 50.0, 60.0, 70.0, 80.0, 85.0, 90.0, 95.0, 97.5, 100.0
SCH5200	1.6 m (2014)	0.0, 0.1, 0.2, 0.3, 0.4, 0.6, 0.8, 1.2, 1.6, 2.0, 2.5, 3.0, 3.5, 4.0, 5.0, 7.0, 9.0, 12.0, 17.0, 32.0, 42.0, 52.0, 62.0, 72.0, 77.0, 82.0, 87.0

No data gaps are visible in the ground temperature records, except for the thermistor at 1.6 m depth at SCH5200, which did not work at all in 2014. While the temperature measurements at SCH5198 and SCH5200 are regarded reliable, problems with some sensors are reported from SCH5000 (Noetzli, August 10, 2015, pers. communication). From mid-September onwards until at least May 2015, unusual temperature jumps, similar to atmospheric variations, are visible at depths between 2.5 and 7 m as well as between 50 and 85 m (data not shown). Furthermore, the temperature sensor at 11 m depth has been showing unusual temperatures for an even longer period. As the remaining sensor depths at SCH5000 and the other two boreholes show reasonable temperature values in the same period, it is assumed that either the temperature sensors are erroneous or that water has intruded the borehole pipe. In the data analysis, this has to be kept in mind.

The borehole temperatures were used to analyse the thermal impact of soil moisture and infiltration events. For this purpose, time series plots, contour plots and temperature envelopes for 2014 were generated. Additionally, the thermal regime at different depths was analysed using thermal orbits. These plots assume that ground temperatures can be

approximated with sinusoidal oscillations with a period of approximately one year whose amplitudes are dampened and phase shifted with depth. The shape of thermal orbits then depends on the mode of heat transport: When conductive heat transfer is present only, the plotting of two temperature series against each other results in an elliptical shape. The orbits can be distorted by phase changes, and other non-conductive heat transfer. As such, they can be used as a measure for the presence of non-conductive heat exchange. (Beltrami, 1996)

Zenklusen Mutter and Phillips (2012b) have found four characteristic shapes of thermal orbits relating to four types of thermal regimes in the permafrost of the Ritigraben torrent (Swiss Alps) which were taken as a basis for the analysis of the thermal regimes at Schilthorn:

(1) A linear relationship between two thermistors arises from a phase lag close to zero which is usually found in large boulders or between close thermistors.
(2) The so-called "butterfly" shape describes an orbit which runs through the 0° C intersection. It is the result of phase changes in spring and autumn and therefore shows non-conductive heat transfer.
(3) Regularly shaped ellipses are due to a purely conductive heat transfer.
(4) Irregular geometries which cannot be attributed to either one of the above shapes point towards non-conductive heat transfer.

4.5 Runoff Modelling

In this work, a glacio-hydrological model (Huss et al., 2008) was applied to simulate the evolution of the snow pack and the resulting runoff from the study area in spring and summer 2014. The Glacier Runoff Evolution Model (GERM) was initially developed to model runoff from highly glacierized catchments and to simulate glacier mass balances. It consists of a mass balance model to account for the glacier accumulation and ablation, an evaporation model, a runoff routing model and a module which accounts for the change in glacier surface topography and glacier retreat.

For this work, an adapted version of the model was taken to simulate the runoff of a small non-glacierized catchment in hourly time steps. Nestler et al. (2014) have successfully applied the model for a similar purpose. In the following, the model and model adaptations as well as the calibration process are described. A detailed description of the modelling process is outlined in Wicki (2015).

4.5.1 Mass Balance Module

Snow melt, which is modelled in the mass balance module, can be calculated using two different approaches. In the distributed temperature-index approach (Hock, 1999), the melt rate M (mm h^{-1} °C^{-1}) is calculated as following:

$$M = \begin{cases} \left(\frac{1}{n} F_M + r_{fsnow/osnow} I_{pot}\right) T & T > 0 \\ 0 & T \leq 0 \end{cases} \tag{4.10}$$

where F_M is a melt factor (mm h^{-1} °C^{-1}), n is the number of time steps per day, r_{fsnow} and r_{osnow} are radiation coefficients (m^3 W^{-1} °C^{-1} h^{-1}) differing for old and new snow, T is the air temperature in °C, and I_{pot} is the potential shortwave irradiance (W m^{-2}). Melt is only calculated for temperatures greater than 0° C.

The second approach calculates the cumulative mass balance B_{cum} (m w.e.) at every grid cell and every time step (t+1) using a simplified energy balance approach (Machguth et al., 2006):

$$B_{cum}(t+1) = B_{cum}(t) + \Delta t \left[min\left(0; -\frac{E}{L}\right) + P_{solid} \right] \tag{4.11}$$

where E is the average daily energy flux at the surface (W m^{-2}), L is the latent heat of fusion (334 kJ kg^{-1}) which contributes to the melting of snow and P_{solid} is the solid precipitation (m w.e.). Precipitation is solid, when the air temperature is below 0° C. Melt water from the snow cover as well as liquid precipitation run off immediately and the energy available for melt E is calculated as following (Oerlemans, 2001):

$$E = p(1-\alpha) I_{pot} + C_0 + C_1 T \tag{4.12}$$

where p is a reduction factor for incoming shortwave radiation accounting for atmospheric aerosols (p=0.8), α is the surface albedo, $I_{pot}$is the potential shortwave irradiance (W m^{-2}), and C_0 (W m^{-2}) and $C_1 T$ (W m^{-2} K^{-1}) represent the longwave radiation balance and turbulent heat fluxes.

Both approaches make use of the potential solar shortwave irradiance I_{pot}. It depends on the top of atmosphere solar radiation, the atmospheric transmissivity, the solar geometry and topographic characteristics and is calculated using a digital terrain model (DTM). (Hock, 1999)

After each time step, the snow depth at each grid cell is updated according to the melt or accumulation calculated. The model is thereby initiated with an initial snow

depth distribution on the basis of the first snow depth measurements. Further snow depth measurements are used for calibration of the mass balance module.

4.5.2 Runoff Routing Module

The runoff routing model consists of an interception, a fast and a slow reservoir. The interception reservoir contains the amount of water which is intercepted at the surface and directly evaporated to the atmosphere. It does not contribute to runoff and its volume $Vint_{max}$ is surface type dependent. If the amount of available water exceeds $Vint_{max}$, first the slow reservoir V_{slow} is filled according to the following equation:

$$^{+}\Delta V_{slow,i} = (P_{liq,i} + M_i) \cdot \left(1 - \left(\frac{V_{slow,i}}{V_{slow_{max},j,i}}^{2}\right)\right) \tag{4.13}$$

where $P_{liq,i}$ is the liquid precipitation, M_i is snow melt and $V_{slow_{max},j,i}$ is the storage capacity of the slow reservoir at cell (i) for a specific surface type (j). Depending on the filling level of the slow reservoir, a fraction of the infiltrating water $(P_{liq,i} + M_i - {}^{+}\Delta V_{slow,i})$ runs directly to the fast reservoir. The fast reservoir represents direct and near-surface runoff and its storage capacity is potentially unlimited. (Farinotti et al., 2011)

The slow and fast reservoirs are emptied as a function of the retention constant k_r:

$$Q_i = \sum_r \frac{V_{r,i}}{k_r} \tag{4.14}$$

where Q_i is the discharge at grid cell (i) and $V_{r,i}$ is the filling level of a specific reservoir (r) (slow or fast) at grid cell (i). In the fast reservoir, the retention constant k_r is surface-type dependent. (Farinotti et al., 2011)

At each grid cell (i) and for every time step, the water volume available for runoff Q_i and the consequent discharge hydrograph are calculated through the following equation (Farinotti et al., 2011; Huss et al., 2008):

$$Q_i = P_{liq,i} + M_i - ET_i - \sum_r \Delta V_{r,i} \tag{4.15}$$

where $P_{liq,i}$ is the liquid precipitation, M_i is snow melt, ET_i is evapotranspiration (calculated from the surface type, air temperature and topography, details not shown here) and $\Delta V_{r,i}$ is the storage change of reservoir (r).

4.5.3 Model Adaptations

Following model adaptations have been undertaken in order to serve the study purpose and to match the study area.

- In order to receive hourly runoff values, hourly precipitation and temperature data are needed.
- As the model does not include redistribution and preferential deposition of snow, the model is started using an initial snow depth distribution, derived from field measurements (see Figure 4.6).
- In the study area, only old snow (accumulated over the winter) and new snow (precipitated during the modelling period) are present. In the model, the initial snow distribution (old snow) is used as the initial glacier surface while the new snow is used as the snow parameter. The corresponding properties (albedo, density, etc.) need to be adjusted accordingly
- In order to account for the increasing infiltration depths and soil volumes due to an increasing active layer thickness, the volume of the slow reservoir is scaled as a function of active layer depth. A reduction factor is applied to the slow reservoir, whose effect diminishes with an increasing active layer thickness. The reduction factor is chosen in a way, that some water may still infiltrate the slow volume when the soil column is frozen throughout. The model assumes a homogeneous active layer depth in the whole subbasin which is a simplification.
- In order to be able to differentiate between loose debris and base rock, the surface category 'pasture' was used for loose debris and its properties were adapted accordingly.

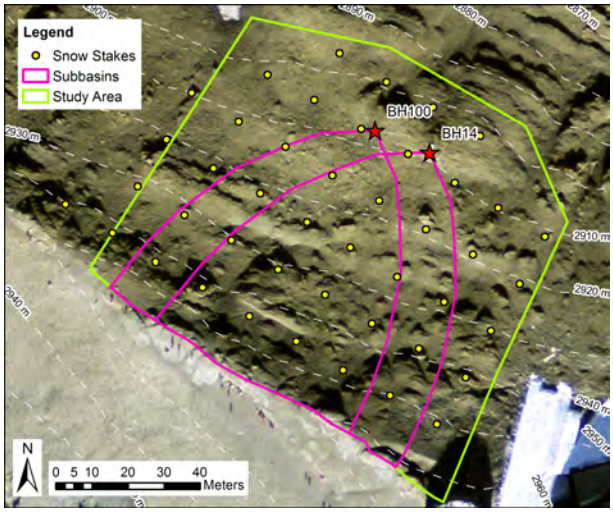


Figure 4.6: Overview of the study area (green polygon), the two subbasins (pink polygons) and the points of snow depth measurements for the GERM simulation.

4.5.4 Model Setup and Calibration

To run the GERM model, following parameters were set initially.

- Three modelling catchments were differentiated (see Figure 4.6): The study area encompasses the area in which the snow melt module was calibrated for. Two subbasins were used to delineate areas upslope of the two borehole locations.
- A precipitation correction factor was determined from the proportion of extrapolated to estimated annual precipitation sums. It was found that the precipitation extrapolation equation generally underestimates annual precipitation sums. The correction factor was determined to be 1.69.
- The surface types loose debris and bedrock were mapped from an aerial image (SWISSIMAGE, swisstopo). The maximum volumes of the slow reservoirs for loose debris and bedrock were set to 90 and 30 mm, respectively.
- The reduction factor to include the effect of permafrost for the two subbasins was adapted to match the temperature records at SCH5198 and SCH5000. The onset and end of the active layer growth at SCH5198 are set to the 20th of July and 10th of October, respectively. At SCH5000, thaw was much faster and they were set to the 2nd and 20th of August 2014. For both subbasins, a linear growth of the reservoir volume is assumed.

The model was initiated with spatial snow depth distribution which was measured on the 3rd of July. The parameters of the mass balance model were then adjusted so that the spatial snow depth distribution fitted to two additional snow depth measurements on the 17th of July and 1st of August. Maps of the snow cover distribution were used to validate the spatial melt out patterns of the models. A validation of the model performance is given in Section 6.4.

Chapter 5

Thermal Regime

In this chapter, the meteorological conditions, the snow evolution and the thermal regime at the boreholes are presented and discussed.

5.1 Meteorology and Snow Depths

Figure 5.1 shows daily mean air temperature and daily mean snow depths measured at the meteorological station as well as daily precipitation sums extrapolated from neighbouring meteorological stations for the year 2014. Until mid-May, temperatures are still below 0° C. During this time, precipitation falls as snow and leads to the build-up of the snow pack which reaches its maximum of 220 cm in mid-May. Remarkably, half of the snow pack is accumulated within one month in April and May.

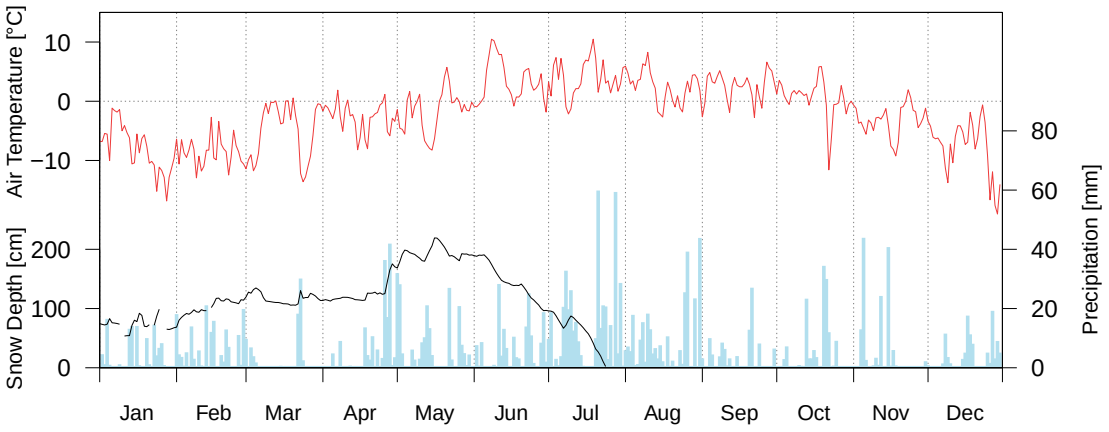


Figure 5.1: Daily mean air temperature (measured, red line), daily precipitation sums (extrapolated, blue bars) and daily mean snow depths (measured, black line) at Schilthorn in 2014.

Temperatures become positive afterwards and mostly stay above freezing throughout the summer until mid-October, periodically dropping below 0° C for short times. From mid-May to mid-August, they range between -1° C and 10° C. The high temperatures lead to a rapid melt-out of the snow pack which has vanished by the end of July. The snow melt period is most pronounced between mid-June and end of July and the rate of snow melt is accelerated towards the end of the period. During this time, many precipitation events take place, most of which fall as rain.

From mid-August, a change in the temperature regime can be observed. Temperatures now range between between -3° C and 5° C and more often drop below freezing. Yet, they are mostly above 0° C. During this time, less precipitation can be observed than in the preceding period. In mid-October, temperatures drop markedly down to -10° C for a short time. They stay mostly below freezing after and drop even further until the end of the year. For the end of the year, snow depth recordings exist but are not shown in this Figure.

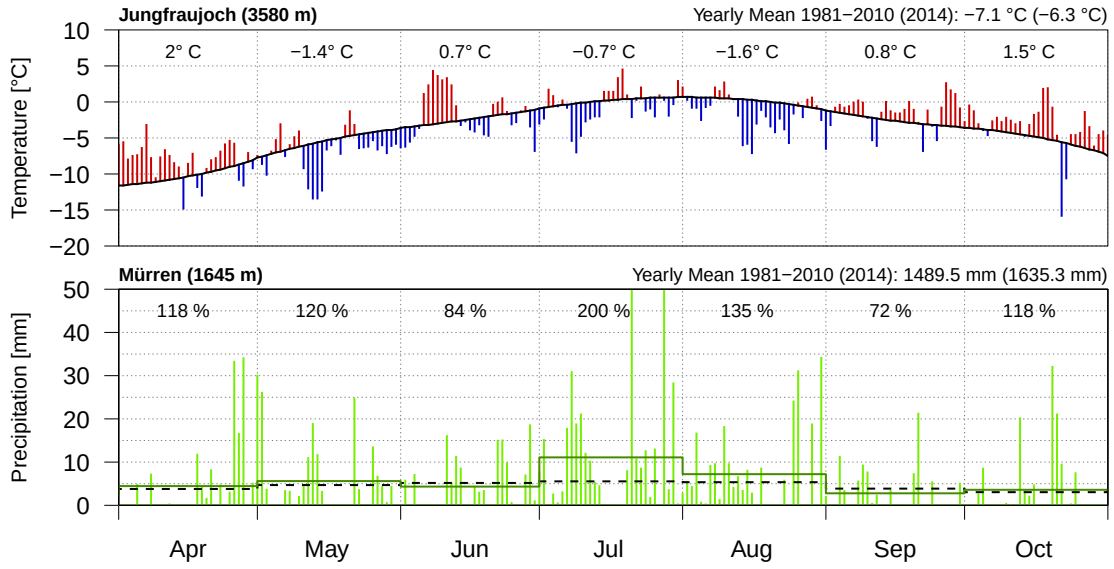


Figure 5.2: Top panel: Daily mean air temperature at Jungfraujoch (3580 m asl) for the reference period 1981-2010 (black line), superimposed by daily positive (red bars) and negative (blue bars) temperature deviations in the year 2014. The numbers indicate the monthly deviation of the year 2014 from the reference period. Lower panel: Monthly mean precipitation sums at Mürren (1645 m asl) for the period 1981-2010 (dashed black line) and for the year 2014 (dark green line) as well as daily precipitation sums in the year 2014 (bright green bars). The numbers indicate the monthly deviation of the year 2014 from the reference period.

In Figure 5.2, the meteorological conditions of summer 2014 are put into a climatological context. In order to cover 30-year periods of measurements, data of neighbouring stations is used for the comparison. Daily mean air temperature is taken from Jungfrau-

joch (3580 m asl, 10.4 km distance) and daily precipitation sums are taken from Mürren (1645 m asl, 4.5 km distance). Both datasets are compared to the corresponding daily and monthly means of the reference period 1981-2010. It is visible that May is much colder than usual whereas precipitation is slightly above average. The first half of June is unusually warm, leading to the onset of the rapid snow melt described before. This period is followed by a rather cold and wet period until the end of August, whereas the month of July receives double and August receives 135 % the amount of precipitation compared to the reference period. In contrary, September and October are warmer than usual, while September is too dry and October slightly too wet.

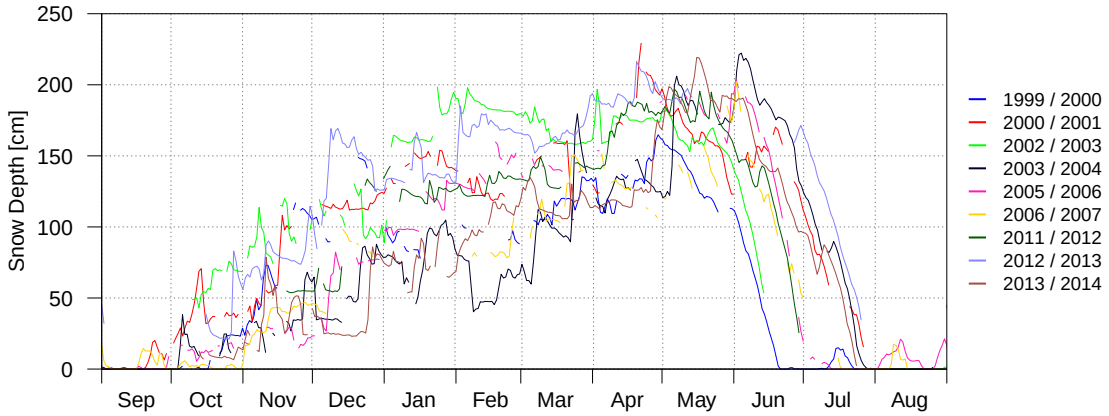


Figure 5.3: Time series of snow depth records in various years measured at the study site. Only cycles with few data gaps are shown.

A comparison of the snow depth evolution at Schilthorn in different years is shown in Figure 5.3. The figure shows the evolution from September to August, whereas only cycles with few data gaps are shown. It is visible that the snow pack usually starts to build up between September and October. Snow depth increases steadily until a maximum is reached between the months of April and June, usually ranging between 150 to 220 cm. Snow melt is fast and the snow pack has ablated within 2 months. By mid-June to the end of July, the meteorological station is snow-free.

The shape of the snow depth evolution is similar from year to year, however, the timing of the establishment a continuous (and insulating) snow cover, the onset of the snow melt period and the timing of the complete ablation at the study site may vary by up to 1.5 months from year to year. Compared to other years, the snow depth in winter 2013/2014 is below average for most of the accumulation period. At the end of April however, heavy snow falls lead to the accumulation of an additional 1 m of snow. The maximum snow depth of 220 cm, which is reached in mid-May, ranges at the top of the records. The snow melt period sets in after, whereas the rate snow melt is slightly lower and the site ablates quite late compared to the other years.

5.2 Spatial Snow Distribution in Summer 2014

The spatial snow distribution at the study site in summer 2014 is shown in Figure 5.4 as it was manually mapped from photographs of the area. The two borehole locations are indicated as red stars and the black polygon marks the area within which the snow distribution was mapped. On the third of July, most of the area is still snow covered and only some outcrops appear at the surface. Yet, the area just below the boreholes already starts to become snow free. A similar spatial pattern is visible on the 17th of July. In contrast to two weeks earlier, the snow-free parts are larger. By the 1st of August, SCH5198 and the meteorological station are snow free. At the same time, SCH5000 and SCH5200 are still covered by about 50 cm of snow.

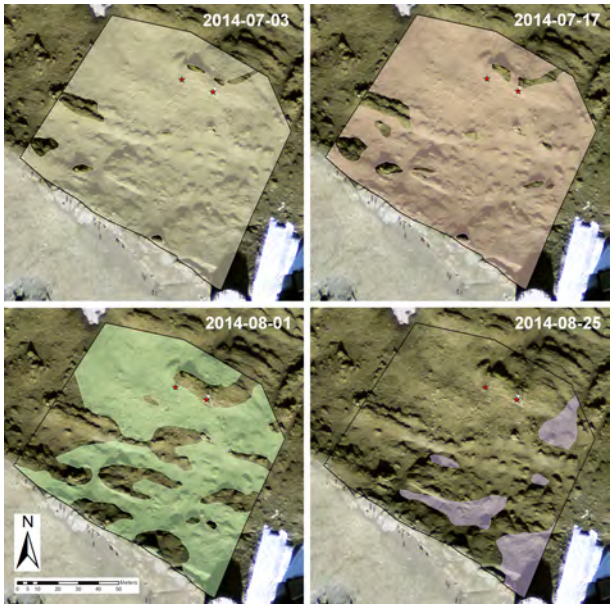


Figure 5.4: Spatial snow distribution in the study area mapped manually from photographs taken on the summit at the 3rd of July (top left), 17th of July (top right), 1st of August (bottom left) and 27th of August 2014 (bottom right). The coloured polygons denote the snow-covered areas and the black polygon denotes the area within which the snow distribution was mapped. The two stars show the locations of the boreholes.

At the 27th of August, most of the snow has vanished and only some patches remain in gullies and in a steep area below the crest. From this map and from field observations it is evident, that snow first ablates on the largest outcrops. Between the outcrops and in the gullies, the snow pack is probably thicker due to wind redistribution and receives less radiation due to shade. It is further visible that at the boreholes, the snow pack retreats from downslope. Furthermore, SCH5198 becomes snow free before the other boreholes. Finally, the period between the first patches become snow-free until all snow has melted can take up to 2 months.

5.3 Ground Temperatures

In the following, the thermal regimes at the three boreholes SCH5198, SCH5000 and SCH5200 are presented. First, time series and contour plots of the ground temperatures illustrate the temporal evolution of subsurface temperatures at the three boreholes in 2014 and over all measurement years. Secondly, some infiltration events are studied in more detail to assess their thermal impact at the boreholes. Finally, the thermal regimes of specific depths are studied in more detail using temperature envelopes and thermal orbits.

5.3.1 Temporal Evolution

In Figure 5.5, the thermal evolution at SCH5198, SCH5000 and SCH5200 is shown for the year 2014. Daily mean ground temperatures are shown at various sensors until 7 m depth. At SCH5198, minimum winter temperatures near the surface (-2.5° C) are reached between January and March. The temperature signal is lagged and amplitudes are dampened with depth; at 7 m depth, temperatures only fall down to -0.5° C and the minimum value is reached in June. After a steady temperature increase of near-surface layers from April until June, ground temperatures show step-wise increases between mid-May and July (see extract). These temperature jumps are delayed and dampened in amplitude at depth, however they happen rather simultaneously. By the end of June, zero-curtain conditions are reached. From mid-July, temperatures surpass 0° C at the surface and start to show large fluctuations. The highest temperatures are reached near the surface (over 7° C in August in 0.2 m depth). The onset of these fluctuations is again delayed with depth while at 5 and 7 m depth, temperatures never exceed 0° C. From mid-October, temperatures fall again below 0° C. While at 0.2 m the ground freezes immediately and temperatures drop well below -2° C at the end of October, zero-curtain conditions are observed between 0.8 and 2.5 m depth for several weeks in autumn before temperatures finally drop below freezing.

Similar patterns are visible at SCH5000: Minimum winter temperatures are reached at the end of March and temperature amplitudes are dampened and lagged with depth. Similarly to SCH5198, a stepwise increase in ground temperatures can be observed between mid-May and end of July until zero-curtain conditions are reached at the end of June. However, the amplitudes are smaller than at SCH5198. Ground temperatures start to show large fluctuations from August. Initially, these temperature fluctuations are dampened and lagged with depth, however this regime seems to change from mid-September: The depths of 0.8, 5 and 7 m show large temperature increases and stay well above 0° C until the end of the year. The depths of 0.2, 1.2 and 2.5 m show a similar behaviour as in SCH5198: Temperatures fall immediately well below 0° C at the surface, whereas at 1.2 and 2.5 m,

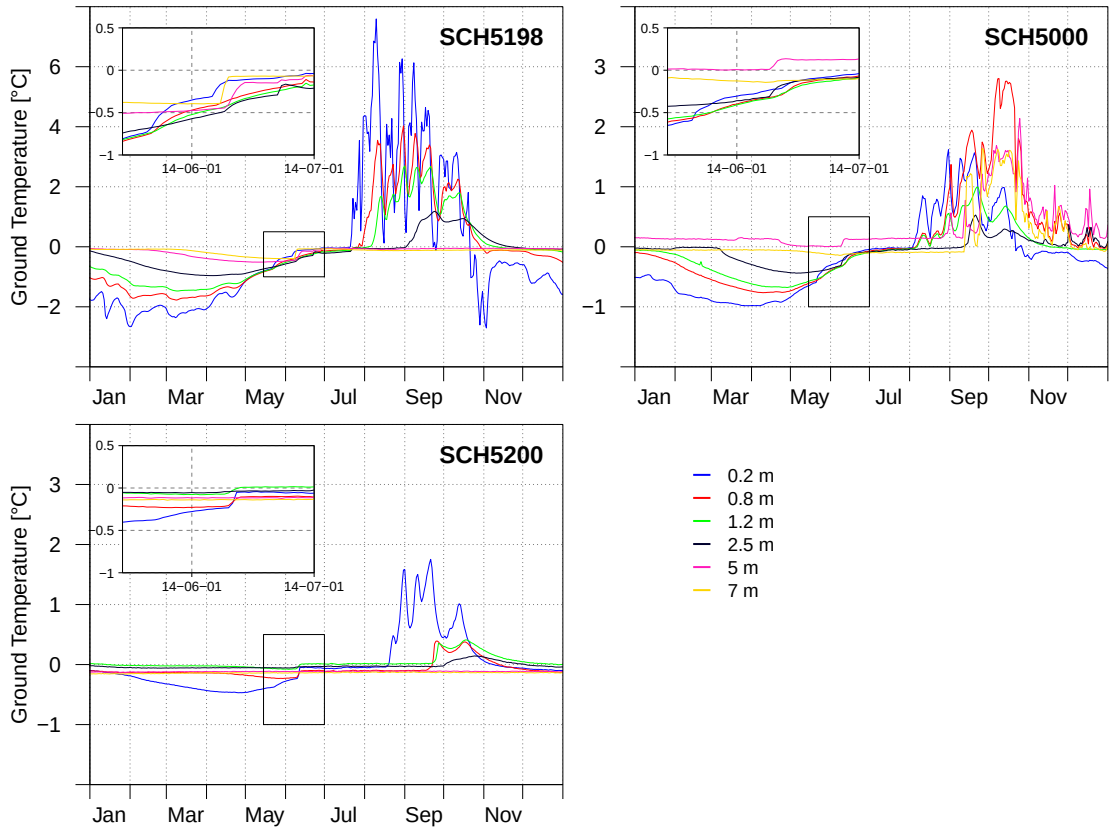


Figure 5.5: Temporal evolution of daily mean subsurface temperatures at various depths near the surface at SCH5198 (top), SCH5000 (middle) and SCH5200 (bottom) from January to December 2014.

zero-curtain conditions are observed for some weeks in autumn before temperatures finally fall below freezing. Overall, it seems that the thermal evolution at SCH5000 is delayed by about 0.5 to 1 month compared to SCH5198. Furthermore, the thermal variability is less than half that of SCH5198.

At SCH5200, the thermal evolution is even more different. Minimum temperatures in winter 2013/2014 only reach as low as -0.5° C near the surface in mid-April. Deeper layers only show few variations. In spring however, the same temperature jumps can be observed as in the other two boreholes, yet they are only visible until 1.2 m depth and are less pronounced. Zero-curtain conditions are reached in mid-June and last until mid-August at 0.2 m. At 0.8, 1.2 and 2.5 m, 0° C are not surpassed until the end of September and further below, the ground does not thaw at all. Ground temperatures at the surface reach zero-curtain conditions again from November but temperatures do not fall below freezing until the end of the year. Compared to the other boreholes, temperature variability is again much smaller at all depths. Furthermore, the temporal evolution is delayed by about 1 month compared to SCH5198. However, the temperature jumps in

spring towards zero-curtain conditions seem to happen simultaneously with the other boreholes.

Figures 5.6, 5.7 and 5.8 show contour plots of daily ground temperatures for the period of 2003 to 2014 at SCH5198 (full profile depth) and at SCH5000 and SCH5200 (uppermost 13 and 12 m, respectively). Full profiles for the latter two are shown in the Appendix A.1. At SCH5198, the maximum active layer depth in 2014 is about 5 m. It is rather small in comparison to the five precedent years (usually about 7 m) and compared to the maximum of almost 10 m measured in 2015. It is further visible that temperatures in summer 2014 were much colder in the upper profile than in most other years. At 3.5 m depth, early stages of talik formation can be observed.

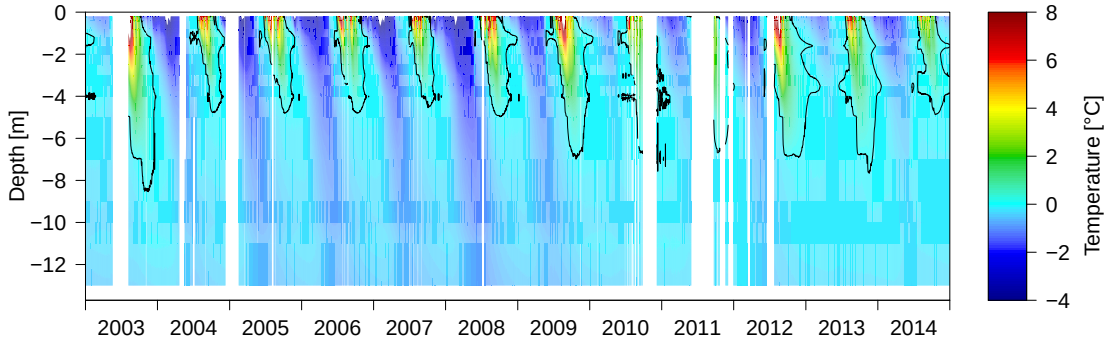


Figure 5.6: Contour Plot of the daily mean subsurface temperatures at SCH5198 in 2000 to 2014.

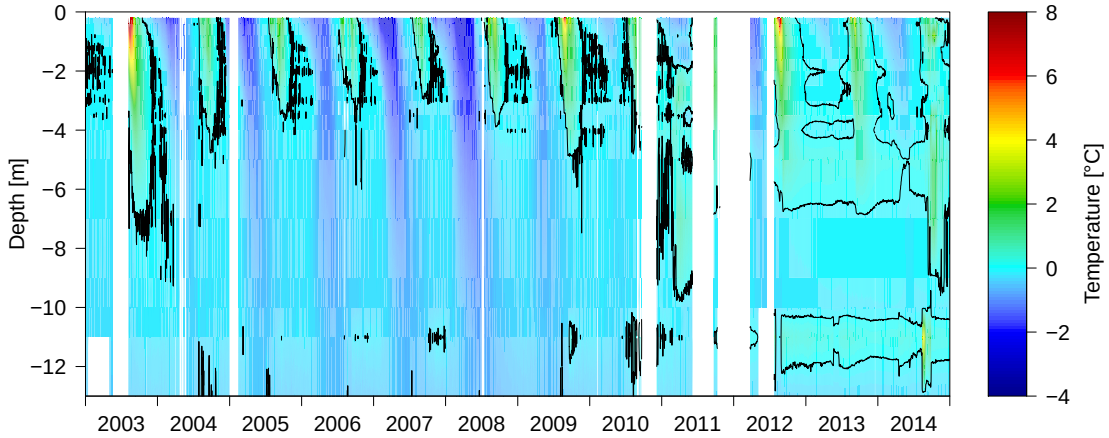


Figure 5.7: Contour Plot of the daily mean subsurface temperatures at SCH5000 in 2003 to 2014 (uppermost 13 m). The black line indicates the 0° C isoline.

At SCH5000, the determination of the active layer depth is more difficult, as some of the data seems to give implausible values. Particularly the depths of 11 m and 85 m seem too warm over all the year. Furthermore, from mid-September onwards, unusual temperature variations to up to +2° C can be observed between 3.5 to 9 m and 50 to 85 m depth. However, a visual comparison with SCH5200 may be useful for an estimate of the

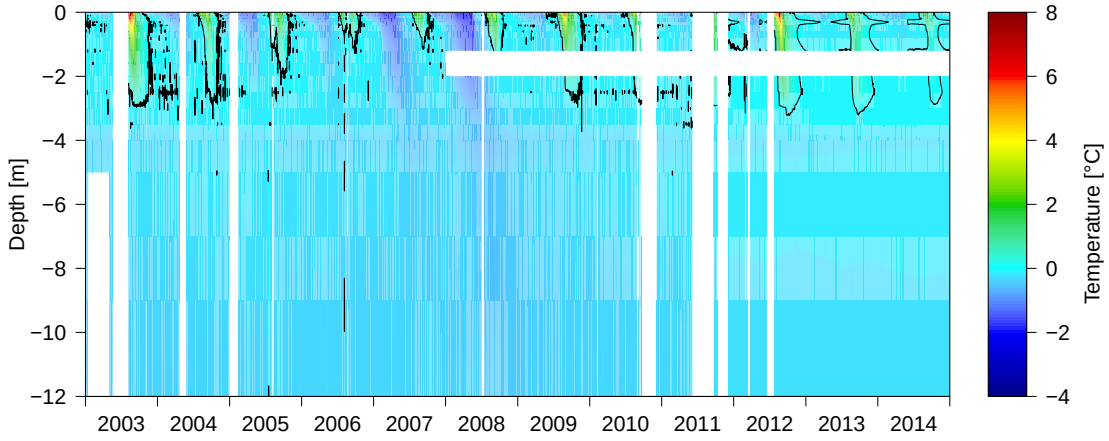


Figure 5.8: Contour Plot of the daily mean subsurface temperatures at SCH5200 in 2014 (uppermost 12 m). The black line indicates the 0° C isoline.

true thaw depth. At SCH5200, the thaw depth in 2014 is similar as in the preceding 5 years (3 m). At SCH5000, the thaw depth in the preceding years was 5.5–6.5 m. Therefore, 6 m is taken as a rough estimate for the thaw depth in 2014. Finally, temperatures in the whole profile of both boreholes were again colder than in other years.

5.3.2 Infiltration Events

In this section, compilations of air temperature (measured), precipitation (extrapolated), snow depth (measured), soil moisture (measured) as well as ground temperature (measured) are plotted as time series in hourly resolution. Soil moisture measurements were only available from August 2014. Particular infiltration events with thermal reactions at the boreholes are identified and discussed. The soil moisture evolution is discussed in more detail in Chapter 6.

In Figure 5.9, weather and snow conditions as well as ground temperature time series are shown during a time, when the ground is still snow-covered and frozen. Four events of step-wise ground temperature increase can be identified, as mentioned above. SM_1 shows sudden temperature increases at SCH5198 (0.2 to 1.2 m) and at SCH5000 (0.2 m) and a mere temperature increase at SCH5200 (0.2 m). These temperature increases take place simultaneously after a phase of intense snow melt (not shown). The lower thermistors show a slightly delayed and dampened reaction. At SM_2, a series of sudden temperature jumps are observed at different times and depths during a period of high air temperatures and strong snow melt. At SCH5198, the upper three thermistors show temperature jumps of up to +0.15° C at the 7th of June. At the 10th of June, a similar reaction can be seen at 1.2 to 2.5 m depth. At SCH5000, initial temperature jumps are visible at the 10th of June in 1.2 to 2.5 m depth. Additionally, the depths of 0.2 to 0.8 m show temperature

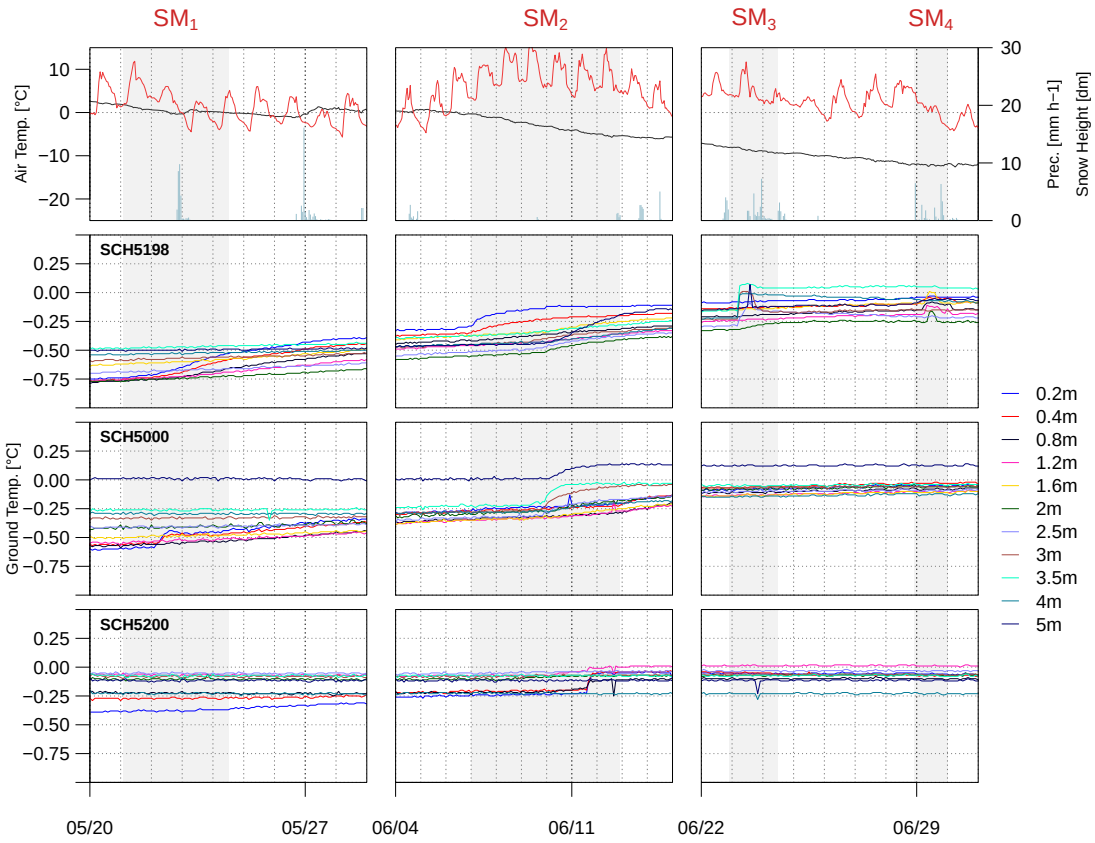


Figure 5.9: Data compilation showing infiltration events during spring. Top panel: Hourly air temperature values (red line), hourly precipitation sums (blue bars) and hourly snow depth values (black line). Other panels: 2-hourly ground temperature values at various depths. The grey background represents the duration of infiltration events (with the corresponding label at the top).

reactions three days later. At SCH5000, the uppermost 1.2 m show sharp temperature increases at the 11th of June. At both SM_3 and SM_4, liquid precipitation events and snow melt take place simultaneously. Significant temperature reactions are only visible at SCH5198. At SM_3, the thermistors between 2 and 5 m show sudden temperature increases, followed by slight decrease, while the upper sensors are still slightly below 0° C. At SM_4, the uppermost 2 m show short term temperature increases above 0° C, followed by zero-curtain conditions.

Figures 5.10 and 5.11 show temperature reactions in relation to infiltration events during snow-free conditions which are primarily related to precipitation. At R_1, precipitation falls when there is still about 20 cm of snow. At the same time, the uppermost 1.6 m at SCH5198 start to show temperatures above 0° C. No temperature reaction is visible at SCH5000 and SCH5200 where the snow cover is still thicker. At R_2, an intense rainfall event coincides with the short-term temperature jumps at 0.8 and 1.2 m. Still no reaction is visible at the other boreholes where the snow cover is still present. R_3 shows

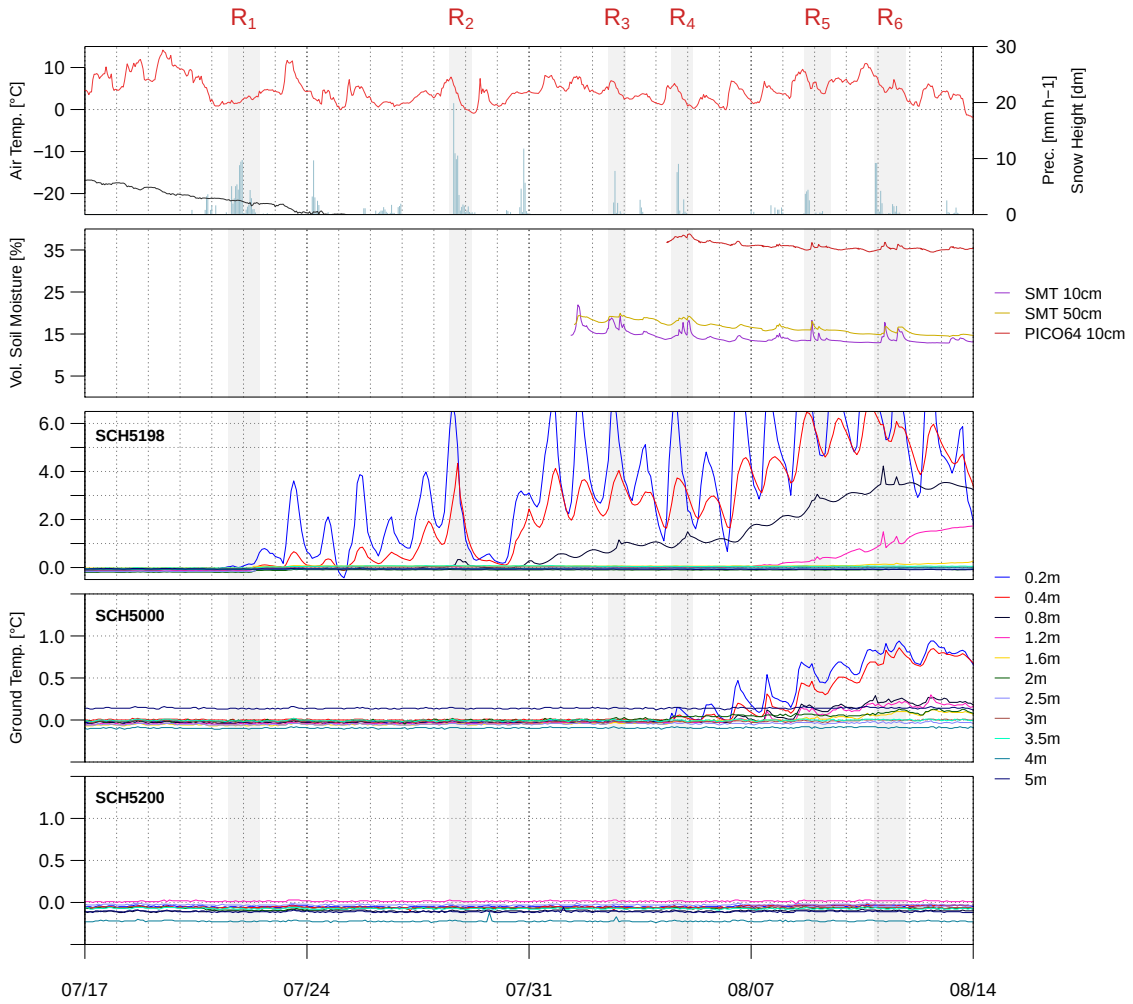


Figure 5.10: Data compilation showing infiltration events during summer. Top panel: Hourly air temperature values (red line), hourly precipitation sums (blue bars) and hourly snow depth values (black line). Second panel: Hourly volumetric soil moisture contents of the SMT and PICO64 sensors (red, brown and purple line). Other panels: 2-hourly ground temperature values at various depths. The grey background represents the duration of infiltration events (with the corresponding label at the top). Black dashed lines correspond to points of manual ERT measurements.

a precipitation event in the evening of the 2nd of August. A short-time peak of +0.1° C is visible in 0.8 m depth at SCH5198, while the other boreholes show no reaction. A similar temperature reaction is visible two days later at R_4 in 0.8 m depth (SCH5198). At SCH5000, the uppermost sensors are now thawed but show no such reaction.

Temperature reactions to infiltration events seem to increase hereinafter in amplitude and in depth. At R_5, a short precipitation event leads to saturated conditions during the night. Short-term peaks of +0.1° C are visible at 0.8 and 1.2 m depth (SCH5198) and slightly earlier at 0.2 to 1.2 m depth (SCH5000). R_6 marks two precipitation events in the

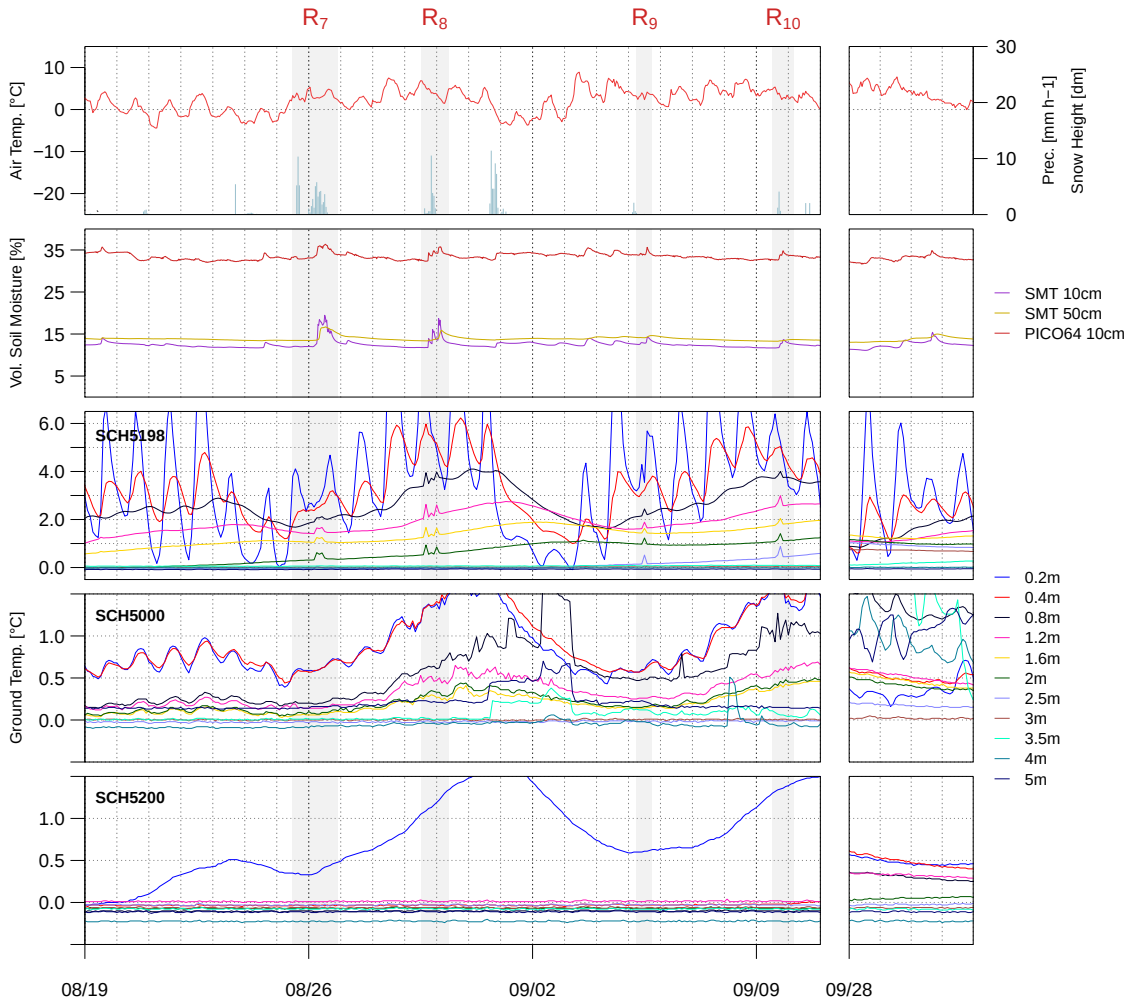


Figure 5.11: Data compilation showing infiltration events during late summer and autumn. Top panel: Hourly air temperature values (red line), hourly precipitation sums (blue bars) and hourly snow depth values (black line). Second panel: Hourly volumetric soil moisture contents of the SMT and PICO64 sensors (red, brown and purple line). Other panels: 2-hourly ground temperature values at various depths. The grey background represents the duration of infiltration events (with the corresponding label at the top). Black dashed lines correspond to points of manual ERT measurements.

early morning and afternoon of the 11th of August which is accompanied by two short-time temperature peaks of up to +0.6° C between 0.4 and 1.2 m depth (SCH5198) and 0.2 to 1.2 m depth (SCH5000). At R_7, a long and intensive precipitation event leads to elevated soil moisture contents during several hours. At SCH5198, temperature peaks of up to +0.3° C happen simultaneously between 0.8 and 2 m depth. Interestingly, no such temperature reaction can be seen at the other two boreholes. A second intensive rainfall event three days later (R_8) shows three distinct peaks in the soil moisture record. All three peaks are represented in the temperature record as short-time peaks of up to +0.6° C in 0.8

to 2.5 m depth (SCH5198). No such simultaneous peaks can be seen at the other boreholes. At SCH5000, temperature variations are visible but appear to be rather random. At R_9 only a small peak in the soil moisture record is visible. Yet, short-term temperature peaks of up to +0.4° C are visible between 0.8 at 2.5 m depth (SCH5198) whereas at the other boreholes, no reaction can be observed. Finally, R_{10} marks the last infiltration event with significant ground temperature reactions. While the soil moisture records and the precipitation data point to only a small rainfall event, short-term temperature peaks of up to +0.5° C can be seen between 0.8 and 2.5 m depth. Again, temperature variations are more irregular at SCH5000 and are not visible at all at SCH5200.

5.3.3 Thermal Regimes

Figure 5.12 shows temperature envelopes (minimum, mean and maximum temperatures in 2014, aggregated daily mean temperatures) of the three boreholes until 20 m depth. At SCH5198, temperature at the surface ranges from about -2.5 to 7.5° C. This annual temperature range decreases with depth, yet the bottom of the borehole does not reach the depth of zero annual amplitude. Temperatures below 0° C are reached all year around from 5 m downwards, which marks the limit of the active layer. The mean ground temperature line is nearly straight and the thermal offset relatively small.

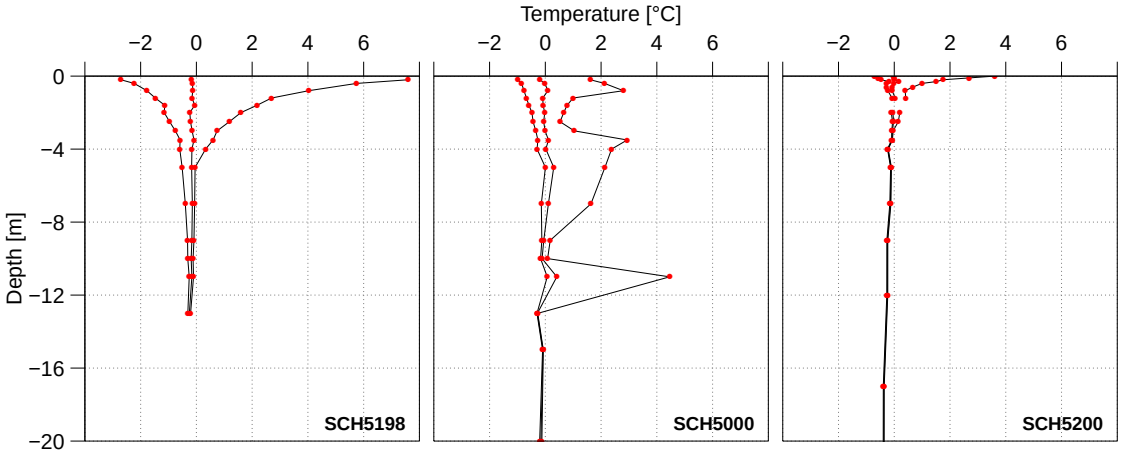


Figure 5.12: Temperature envelopes showing minimum, mean and maximum temperatures (aggregated daily mean temperatures) of the top 20 m at the three boreholes SCH5198 (left), SCH5000 (middle) and SCH52000 (right) for the period 2014-01-01 to 2014-12-31

At SCH5000, the temperature profile seems quite distorted, due to the reasons mentioned above. In particular the sensors at 0.4 and 0.8 m, between 2.5 and 9 m as well as at 11 m show partly considerably warmer temperatures which exceed the temperatures at similar depths at SCH5198 and SCH5200 by several degrees Celsius. It is therefore not possible to determine reliable values for the depth of zero annual amplitude, active layer

depth or the thermal offset. From the minimum temperature profile however, which seems more reliable, it can be stated that the overall temperature variability is smaller than at SCH5198.

The maximum temperature range at SCH5200 can be observed at the very surface (0 m) and spans from -0.7 to almost 4° C. The annual temperature variability decreases rapidly with depth and at 3 m depth, the annual temperature variation is less than 0.1° C. It is also from 3 m downwards, where summer temperatures do not exceed freezing and thus marks the limit of the active layer. The temperature offset is again very small and the overall temperature variability is much smaller than at SCH5198 and SCH5000.

Figure 5.13 shows typical thermal orbits as they were found at the three boreholes. Panels A, B, C, D and F are similar to the classification scheme of Zenklusen Mutter and Phillips (2012b) (see Section 4.4) while Panel E is only seen at Schilthorn. Panels A to C show three types of the butterfly shape. Panel A shows a butterfly with high variability particularly on the positive limb (type "Butterfly high variability"). This shape is typically observed in near-surface layers and is due to a high day-to-day variability and the presence of non-conductive heat transfer. In Panel B, the irregularities are much smaller but still, the orbit goes through the 0° C-intersection, inhibiting phase changes (type "Butterfly low variability"). These depths are still within the active layer, but disturbances by other non-conductive forms of heat transfer than phase changes are small.

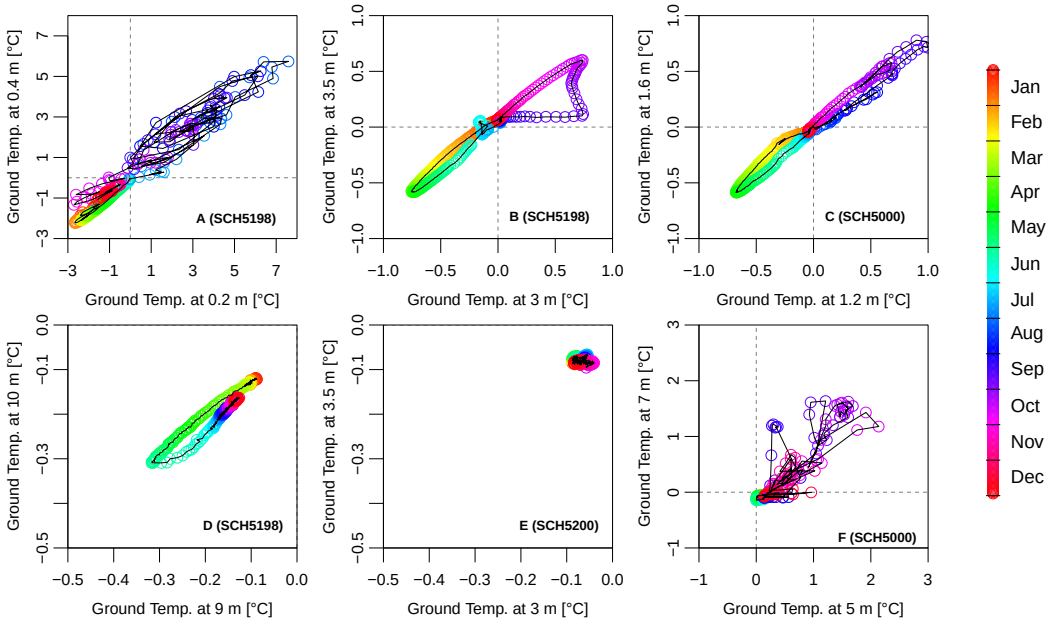


Figure 5.13: Typical shapes of thermal orbits at the three boreholes for the period 2014-01-01 to 2014-12-31. The six panels show the types "Butterfly high variability" (A), "Butterfly low variability" (B), "Butterfly linear" (C), "Ellipse" (D), "Spot" (E) and "Irregular" (F).

In Panel C, both limbs are quite flat, showing a nearly linear relationship (type "Butterfly linear"). This indicates a fast transfer of heat within the active layer. Conductive heat transfer only can be seen in Panel D, where the shape is very similar to a regular ellipse (type "Ellipse"). In panel E, variability is too small to be detected and the orbit covers only a tiny surface (type "Spot"). This depth is below the ZAA and is also characterised by conductive heat transfer only. Finally, Panel F shows a form which does not seem to show regular patterns and a much higher temperature variability at lower sensors. This is typically due to the presence of non-conductive heat transfer, due to talik formation or due to bad temperature data. Table 5.1 lists the shapes between all sensor depths at each borehole within the upper 13 m of the profiles. Corresponding plots of thermal orbits are shown in Appendix A.1.

Table 5.1: Classification of the shapes of the thermal orbits at each sensor pair for each borehole (within the upper 13 m of the profiles). The type "Butterfly" is abbreviated as "BF" and "variabilty" is abbreviated as "var.". Depths are shown in meters.

Initial	SCH5198		SCH5000		SCH5200	
Depth	Depth	Shape	Depth	Shape	Depth	Shape
0.0					0.1	BF high var.
0.1					0.2	BF high var.
0.2	0.4	BF high var.	0.4	BF high var.	0.3	BF high var.
0.3					0.4	BF low var.
0.4	0.8	BF high var.	0.8	BF high var.	0.6	BF low var.
0.6					0.8	BF low var.
0.8	1.2	BF high var.	1.2	BF high var.	1.2	BF low var.
1.2	1.6	BF high var.	1.6	BF linear	2.0	BF low var.
1.6	2.0	BF low var.	2.0	BF linear		
2.0	2.5	BF low var.	2.5	BF low var.	2.5	BF low var.
2.5	3.0	BF low var.	3.0	BF low var.	3.0	BF low var.
3.0	3.5	BF low var.	3.5	Irregular	3.5	Spot
3.5	4.0	BF low var.	4.0	Irregular	4.0	Spot
4.0	5.0	Irregular	5.0	Irregular	5.0	Spot
5.0	7.0	Irregular	7.0	Irregular	7.0	Spot
7.0	9.0	Ellipse	9.0	Irregular	9.0	Spot
9.0	10.0	Ellipse	10.0	Irregular	12.0	Spot
10.0	11.0	Ellipse	13.0	Irregular		
11.0	13.0	Ellipse				

From the thermal orbits it can be inferred, that at SCH5198, non-conductive heat transfer processes are the most effective in the uppermost 1.6 m and their impact declines thereafter. Between 5 and 7 m, irregular shapes indicate the presence of non-conductive

forms of heat transfer, however their impact is small and zero-curtain conditions are not reached. Further below, conductive heat transfer is the only mode of energy exchange. It can thus be concluded, that non-conductive heat transfer through water infiltration is the highest in the uppermost 1.6 m and significant further below until 5 m depth. Between 5 and 7 m depth, water infiltrates and refreezes, however only little transport of energy is observed. Below 7 m depth, no water infiltration is visible.

At SCH5000, thermal orbits can only be reliably discussed until about 2.5 m depth due to the problems with the thermistors (see Section 4.4). In this range, non-conductive heat transfer is present and the variability decreases downwards. In contrary to SCH5198, the thermal orbits are rather flat, which points towards downwards infiltration events and an absence of lateral water inflow. At SCH5200 however, such rather linear relationships are not observed. At this borehole, non-conductive heat transfer is visible until the maximum depth of zero-curtain conditions at 2.5 m, however they are most intensive in the uppermost 1 m. From 3 m on downwards, only conductive heat transfer is observed. This points towards water infiltration until 3 m depth while most water infiltration occurs in the uppermost 1 m.

5.4 Discussion

From the temperature records, infiltration events into frozen and unfrozen grounds can be differentiated. In frozen conditions, temperature jumps towards zero-curtain conditions are related to the refreezing of infiltration water and subsequent release of latent heat. This effect was already shown at the study site in a modelling study by Scherler et al. (2010). According to the authors, water (mainly originating from the melting snow cover) infiltrates the ground and refreezes due to the frozen conditions. Consequently, the freezing water releases latent heat and leads to a warming of the corresponding soil layer. The heat is transported downwards via heat conduction which can be observed as a dampened and delayed temperature increase in deeper layers. The formation of ice impedes further water infiltration until enough water pressure is built up at the surface to cause further water infiltration and the onset of a new infiltration/refreezing cycle.

In the field observations, the temperature jumps happen simultaneously at multiple boreholes, which is attributed to periods of strong snow melt. This supports the findings of Scherler et al. (2010), that enough water pressure (high snow melt rates) needs to be built up in order to trigger water infiltration. The observations further show temperature shifts at some depths, while upper lying layers are still frozen and do not show a similar temperature increase (see SM_2 at SCH5198 and SCH5000). After some time, temperatures increase in upper layers too. It is suggested that this is due to preferential flow through

lateral infiltration from upslope. In contrary to the model results, no temperature decrease after the refreezing and conduction of heat downwards is observed in the field data of 2014. As a consequence, zero-curtain conditions are reached earlier and fewer temperature shifts are observed. This suggests, that the model overestimates heat conduction downwards during this period.

Once zero-curtain conditions are reached, no refreezing takes place. However, short-term temperature jumps can be observed simultaneously with the infiltration of relatively warm rain water. It is thus suggested that these short-term temperature peaks represent the advection of sensible heat in the ground. However, the impact of these temperature jumps is only short-term and diminishes after soil moisture contents have reached precedent values.

In general, the thermal variability at SCH5198 is much higher than at SCH5000 and SCH5200 in both frozen and thawed conditions. Moreover, the short-term temperature reactions related to the advection of sensible heat are only observable at SCH5198. At SCH5000/SCH5200 in contrary, no such temperature reaction is observable. Despite this higher sensibility to thermal impacts at SCH5198, active layer depths are similar at both SCH5198 and SCH5000.

This differences in the thermal regimes of the boreholes point towards a higher thermal conductivity at SCH5198 which may be due to different soil thermal properties at this borehole. However, the borehole set up may contribute significantly to the different thermal regimes. While the borehole of SCH5198 is not covered, the boreholes of SCH5000 and SCH5200 are covered with a PVC pipe. This pipe may considerably alter the thermal conductivity between the soil and the thermistors. Furthermore, the short-term temperature reactions at SCH5198 could be due to the infiltration of water into the borehole. As such, the borehole would act as a large macropore which facilitates the infiltration of soil water and leads to the (simultaneous) short-term temperature peaks.

The meteorological conditions of summer 2014 were rather cold and wet and a lot of soil moisture was available for non-conductive heat transfer. Compared to summer 2003 however, which was hot and dry (Schär et al., 2004), active layer depths are relatively shallow. This suggests that non-conductive heat transfer rather alters the active layer growth as opposed to conductive heat transfer, which mainly controls the active layer thickness.

Chapter 6

Hydrological Regime

In this chapter, the soil moisture conditions at Schilthorn are assessed. First, soil moisture sensor data is presented, followed by photographs and field observations, soil samples, and the modelling results of the GERM runoff model. Finally, the hydrological regimes are discussed in more detail.

6.1 Soil Moisture Sensors

The volumetric soil moisture (daily mean contents) of the SISOMOP, SMT and PICO64 sensors in 2014 are shown in Figure 6.1. No data is available in spring and early summer. Yet, it is visible that soil moisture content slightly decreases in winter and shows no day-to-day variation. In August, initial soil moisture contents are high but decrease thereafter. Day-to-day variability is high during this time. In late October, soil moisture decreases rapidly until stable low values are reached in November.

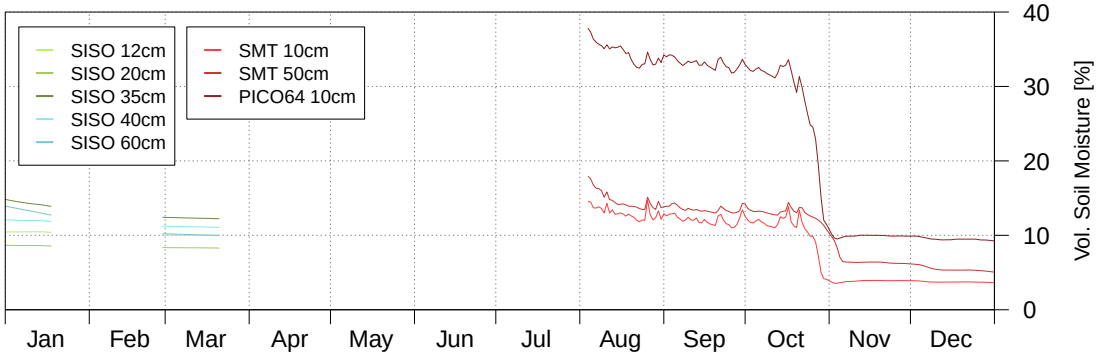


Figure 6.1: Daily mean volumetric soil moisture content of the SISOMOP (abbreviated as "SISO"), SMT and PICO64 sensors for the year 2014.

Hourly volumetric soil moisture values of the SMT and PICO64 sensors as well as hourly precipitation and air temperature are shown for the summer months 2014 in Figure 6.2. The Figure does not show the first few days of measurements which show unusually high variations in soil moisture which might be due to the installation of the sensors (Pellet, December 17, 2015). At the beginning of the measurements, soil moisture levels are generally high, continuously decreasing by 3 to 5 vol. % until the 10th of August. During this time, the sensors are already snow-free but still in the vicinity of upslope snow patches. The temporal variability is high, showing distinct daily cycles.

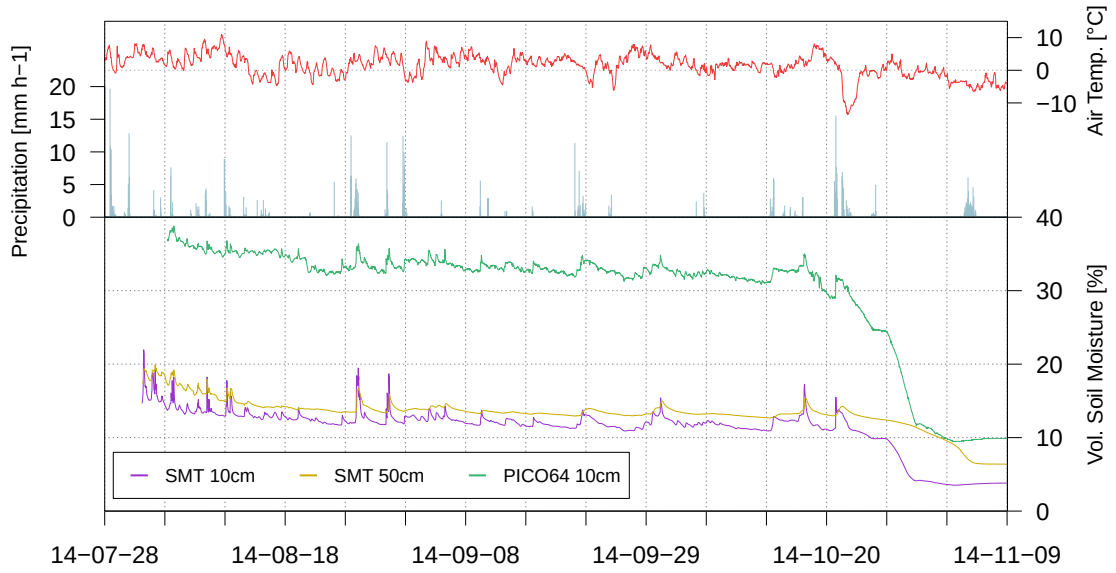


Figure 6.2: Vol. soil moisture at 10 and 50 cm depth measured by the SMT and PICO64 sensors in summer 2014.

From mid-August until mid-October, soil moisture levels rest roughly at the same level. They show sharp increases in response to precipitation events followed by an initially faster, later slower decrease in volumetric soil moisture. Peak levels of saturation are generally lower than during the precedent period, however strong and long lasting precipitation events may lead to saturation levels which are comparable to the previous peaks. Particularly the peak level of the 26th of August 2014 may be close to saturation, as during this precipitation event, surface runoff was observed in the field at some locations in the slope (yet not at the sensor location). The lowest saturation levels are reached after long periods of dry weather. After mid-October, a sharp decrease in soil moisture levels is visible in response to a pronounced temperature drop and subsequent freezing of the soil. Soil moisture drops to 5 to 10 vol. % and stays at this level onwards.

Differences between the sensors are visible as a function of location and depth. The PICO64-sensor shows much higher soil moisture levels (30-40 vol. %) than the SMT sensors (10-20 vol. %), probably owing to the different locations. It is further visible, that the sensor at 50 cm depth has a reduced variability compared to the sensors at 10 cm depth.

Also, initial reaction and peak of saturation are delayed at 50 cm depth compared to the upper sensors.

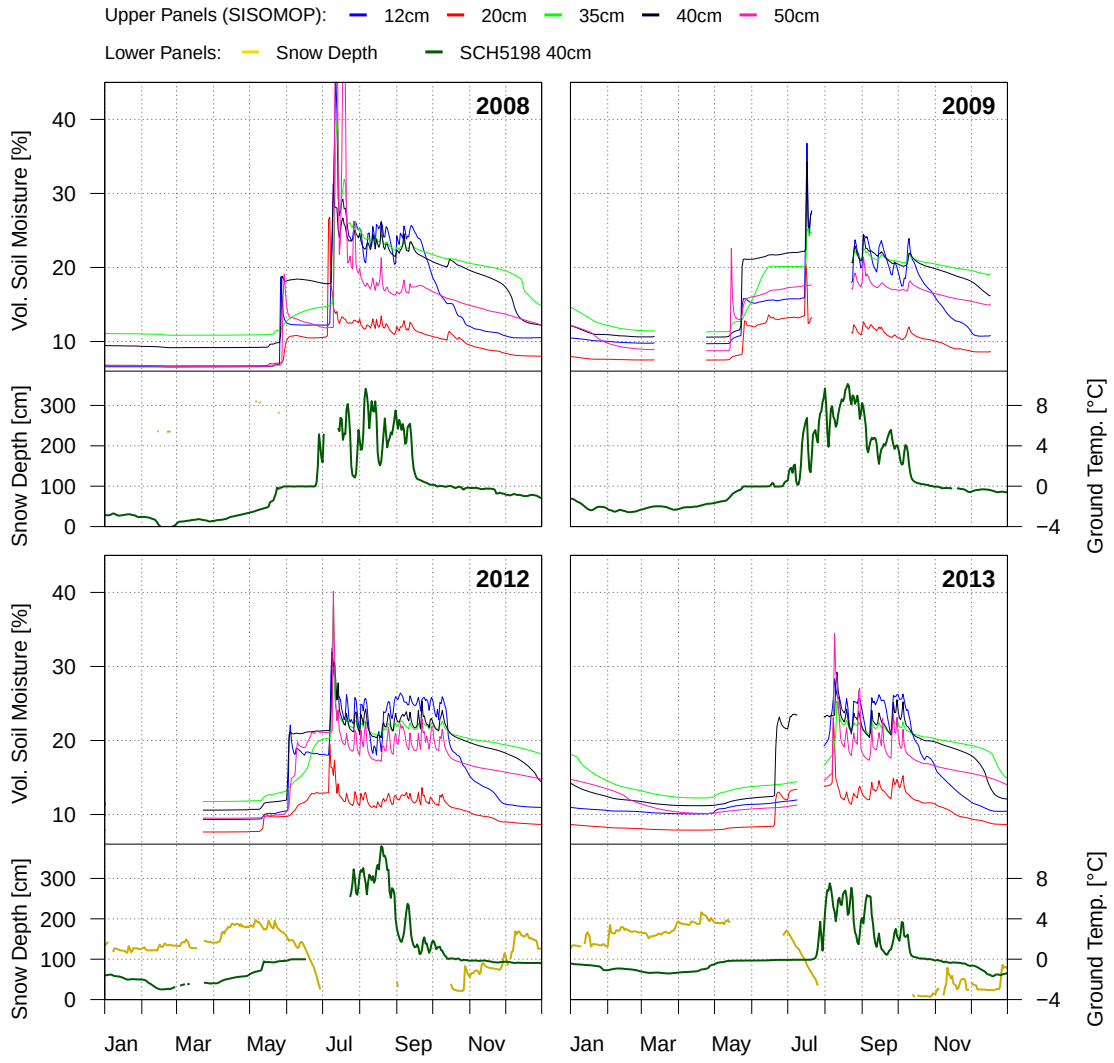


Figure 6.3: Upper Panels: Seasonal variation of volumetric soil moisture (daily mean values) at various depths measured by the SISOMOP sensors in the years 2008, 2009, 2012 and 2013. Lower Panels: Snow depths and ground temperatures at SCH5198 (40 cm depth) in the corresponding years.

Figure 6.3 shows seasonal variations of volumetric soil moisture measured by the SISOMOP sensors. The four panels show years of only few record gaps and depict the depths of 12 cm, 20 cm, 35 cm, 40 cm and 50 cm. Additionally, snow depths and ground temperatures at SCH5198 at 40 cm depth are shown (almost no snow depth records are available for the years 2008 and 2009). In winter, soil moisture levels drop to the range of 7 to 12 vol. % and remain at this level for several weeks showing no day-to-day variability in response to ground freezing. In spring, soil moisture levels shift sharply to 10 to 20 vol. % which coincides with the onset of snow melt and sudden ground temperature increases

towards 0° C. A second larger soil moisture increase can be observed after zero-curtain conditions have been reached at the borehole. While some depths show a relatively slow but steady increase, others increase by up to +10 vol. % within a day, often inhibiting a short-term peak level which is even higher. Soil moisture levels hereinafter show little day-to-day variability and rest at a constant level for 1 to 1.5 months.

This period is followed by a third sharp increase in volumetric soil moisture, leading to the highest levels of soil moisture of the year (15 to 30 vol. %). The sharp increase is usually accompanied by a very short peak reaching up to 40 vol. %. Furthermore, it coincides with the complete ablation of the snow pack and the coupling of the ground to atmospheric conditions. Within the following 10 to 15 days, soil moisture levels gradually decrease until they reach a level of 10-25 vol. % showing medium day-to-day variability. In the following period which lasts until autumn, soil moisture values generally stay at a stable level however showing irregular day-to-day variability. At the end of this phase, soil moisture levels drop again until they reach winter levels and the day-to-day variability diminishes.

6.2 Field Observations

In this section, field observations of different near-surface soil moisture conditions are presented. Figure 6.4 shows surface runoff during times of strong snow melt (31st of July 2014, afternoon). During this time, thaw depths are still shallow and both locations lie within 10 m of an upslope snow patch. While the larger rocks and boulders at the surface are dry, the soil matrix seems to be wet. Surface runoff appears above and just below outcrops and is concentrated in local depressions.



Figure 6.4: Photographs of near-surface soil moisture during field observations. Left image: Surface runoff in a small depression below a bedrock outcrop crossing SCHpara2 (at 22 m). Right image: Surface runoff over a bedrock outcrop below SCHpara2 (at 10–14 m).



Figure 6.5: Photographs of near-surface soil moisture occurrence during field observations. Left image: Wet surface below an ablating snow patch at SCHpara2 (at 5–12 m). Right image: Surface runoff at the same location and time (SCHpara2, 8 m).



Figure 6.6: Photographs of near-surface soil moisture occurrence during field observations. Left image: Soil wetness below an ablating snow patch near SCH5198 along SCHpara1_ext. Right image: Surface runoff along SCHpara1_ext (56 m) during a precipitation event.

Figure 6.5 shows the presence of near-surface soil moisture just below an ablating snow patch at the same day and near the location of above. On the image, it is visible that the area just below the snow patch is wetter than the surrounding area. At the outcrop in the left of the image, the water seems to be diverted downslope to the left. The close up of the scene (right image) shows that the ground is very wet and it even produces surface runoff.

On figure 6.6, a close up near SCH5198 along the SCHpara1 profile line is visible where the active layer was 0.8 m at that time. It is located just below an ablating snow patch and further infiltration of melt water is impeded. SCH5198 is located on a small plateau which regularly showed saturated conditions when it was still in vicinity of upslope snow patches (end of July until beginning of August 2014). On the right image, surface runoff is visible at the end of the SCHpara1_ext profile line (20 days later). At the time, a

long and intensive precipitation event led to saturated soils. There were no snow patches upslope the photograph location.

6.3 Soil Samples

In Figure 6.7, volumetric soil moisture contents derived from soil samples (dots) and measured with the ThetaProbe soil moisture sensor (stars) are presented. The colours of the points denote the day, at which the samples were taken. It is visible that the variability within a profile line can be quite large, particularly along SCHpara1 and SCHpara2, which however is attributed to the presence of upslope snow patches. Furthermore, the ThetaProbe and soil samples seem to agree quite well, as visible at SCHpara2, where soil samples and hand probe measurements were conducted on the same day. More specifically, the ThetaProbe produces the same spatial variability as the soil samples.

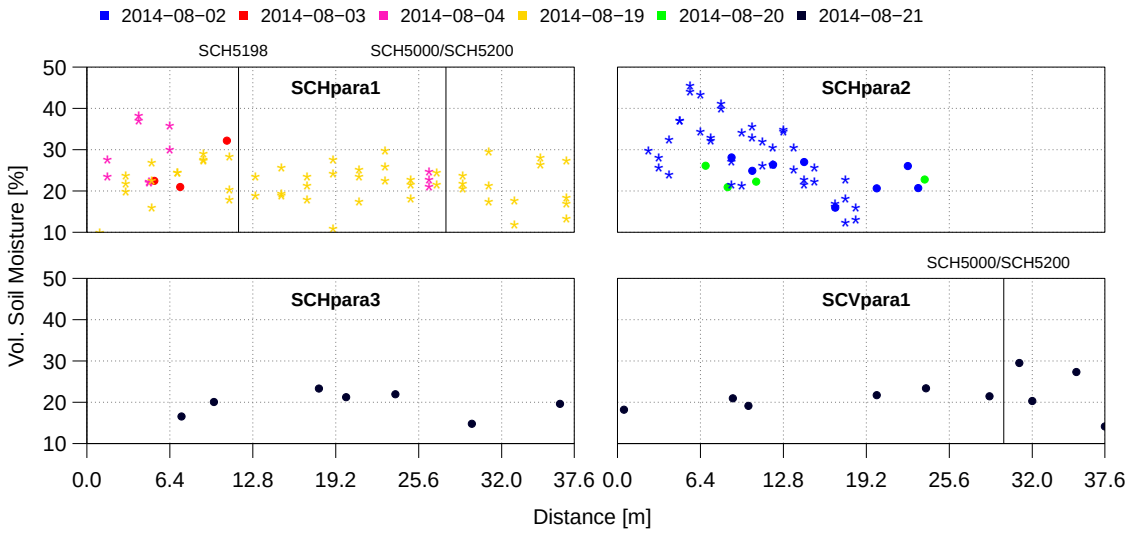


Figure 6.7: Volumetric soil moisture content of soil samples (dots) and the hand probe (stars) taken along the ERT profile lines.

6.4 Runoff Modelling

In this section, the model results of the GERM simulation are presented. As mentioned above, the model was run for two subbasins and two different mass balance models. In the following, only the results of the degree day model and the subbasin above SCH5198 are discussed, as all four combinations of the mass balance models and subbasins yield similar results. For a complete discussion, see Wicki (2015).

Figure 6.8 shows the spatial snow depth distribution at four time points in summer 2014 as it was modelled by the GERM model (degree day model). Similar distribution

patterns is modelled as the one observed in the field (see Figure 5.4): The first patches to become snow free are some prominent outcrops, which initially had smaller snow depths due to the redistribution of snow. In contrary, some snow patches still persist in the end of August in small gullies and in a steep part near the crest. Furthermore, at the boreholes, the snow pack retreats upslope. However, in comparison to the snow depth measurements (data not shown), the model underestimates the snow depths at the 17th of July in the whole study area by as much as 0.5 m. This might be due to an underestimation of the amount of snow accumulation during a snow fall event in this period.

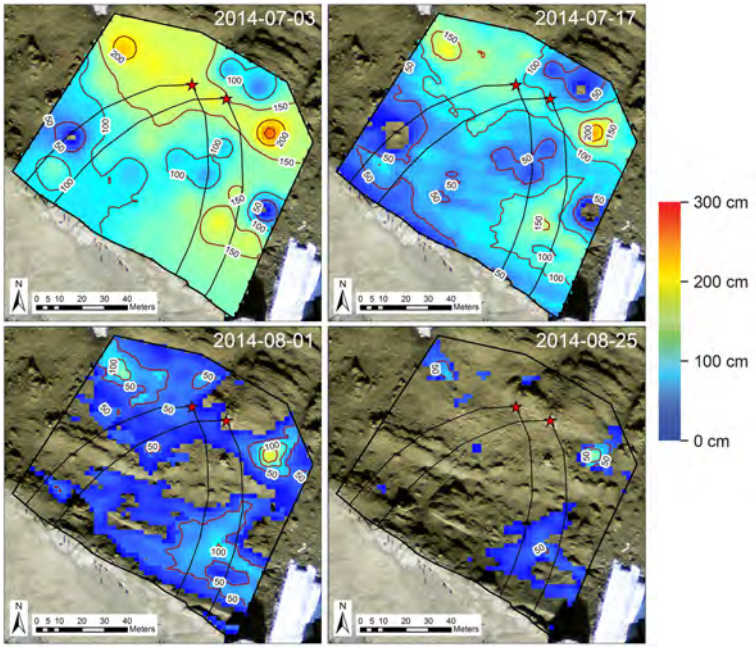


Figure 6.8: Spatial snow depth distribution as simulated by GERM (degree day model) at the 3rd of July (top left), 17th of July (top right), 1st of August (bottom left) and 25th of August 2014 (bottom right). The black polygons denote the subbasins and study area and the red stars show the locations of the boreholes.

The model results of the runoff module are presented in Figure 6.9. The lower panel shows hourly runoff values (black line) and daily SWE values (green line) for the subbasin above SCH5198. The upper panel shows hourly temperature and precipitation data which were used to drive the model. It is visible that during times of strong snow melt (i.e. when SWE decreases), runoff shows daily cycles as a function of air temperature. Furthermore, base runoff (delayed runoff) builds up and increases as a function of the duration and intensity of a specific snow melt phase. With an increasing base runoff, daily runoff peaks increase too. This can be attributed to the filling of the slow reservoir which only receives a fraction of the total runoff. It is further visible that when temperatures drop below 0° C, runoff decreases considerably. During these times, snow may even accumulate during precipitation events. When runoff is produced from snow melt only, peak flows are typically reached at the end of strong snow melt phases. In general, precipitation events

are highly variable in both timing and intensity and reach the highest overall runoff values. Snow melt events in contrary show regular peaks and troughs while the maximum runoff values are considerably smaller than the maximum runoff values of precipitation events.

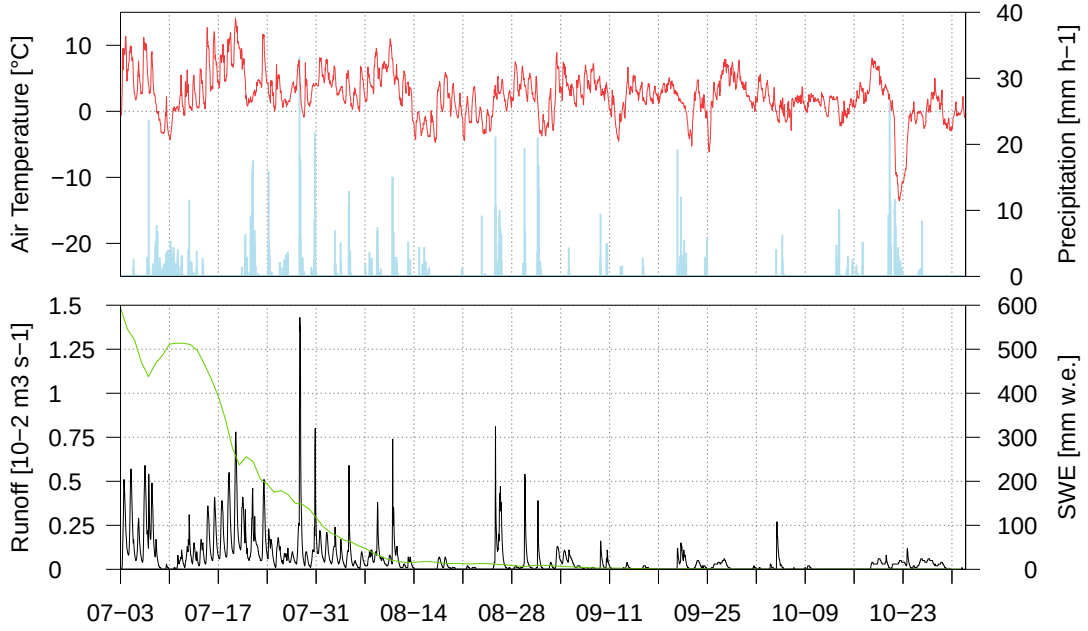


Figure 6.9: Top panel: Hourly temperature values (measured, red line) and hourly precipitation sums (extrapolated and adjusted, blue bars) at the study site. Bottom panel: Hourly runoff generated from a catchment above the study site (modelled by GERM, black line) and hourly snow water equivalent of the snow pack in same catchment (modelled by GERM, green line).

When most of the snow in the catchment has ablated, runoff is mainly produced as a function of the duration and intensity of liquid precipitation events. Compared to snow melt induced runoff, runoff from precipitation events happens rather irregularly, may vary greatly from event to event and can produce higher peak flows. However, as most precipitation events are of short duration and soil water drains quickly, usually no base flow can build up. Towards the end of the modelling period, the percolation of rain water is even enhanced, as the permafrost implementation in the model assumes a higher infiltration capacity, due to higher active layer thickness (as discussed in Section 4.5). If liquid precipitation events coincide with snow melt pulses, the curves are simply added (no interaction between the snow pack and the rainwater is included in the model).

Figure 6.10 shows a comparison of hourly runoff values with hourly volumetric soil moisture contents of the SMT and PICO64 sensors. The runoff values of the model cannot be directly compared to the soil moisture values as they represent a different process. Yet, in the model, runoff is the fraction of soil water which is not stored in the slow reservoir. It can thus be related to the fraction of soil water which is not stored in the soil matrix, i.e.

the bulk water in the pores and the surface runoff. The bulk water in the pores in return makes up most of the peak volumetric soil moisture contents measured by the sensors. The runoff values (minus surface runoff) can thus be connected with the peak values of the soil moisture sensors. The comparison shows, that the runoff values correspond well with the timing of peak soil moisture values. Furthermore, it well reproduces the relative heights of the peak flows.

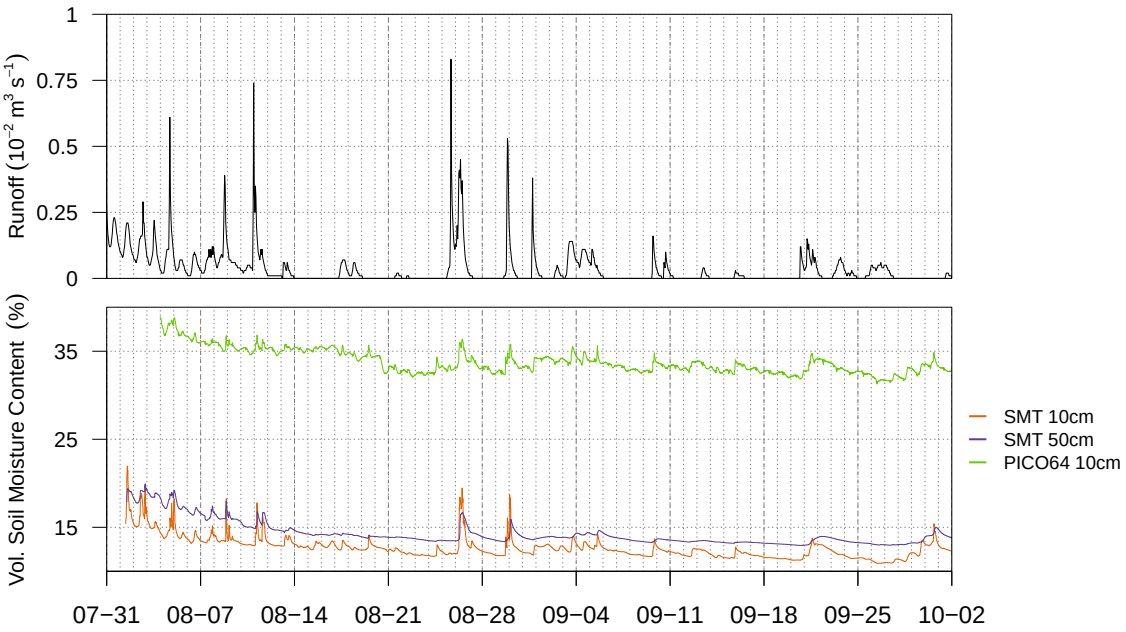


Figure 6.10: Hourly runoff modelled by GERM (upper panel) and hourly values of volumetric soil moisture measured by the SMT and PICO64 sensors in summer 2014 (lower panel).

6.5 Discussion

From the soil moisture sensor data it is evident, that soil moisture conditions change considerably over the year. Four regimes can be distinguished, as they were already identified by Hilbich et al. (2011). In the following, these regimes are discussed and complemented with the results of this study. The naming of the periods corresponds to the naming of Hilbich et al. (2011).

Period I (Dry Snow Period) lasts from the establishment of a continuous and insulating snow cover in autumn until the onset of snow melt in spring. The soil moisture contents continuously decrease until minimum values are reached after 2 to 4 months, which is attributed to the freezing of soil water. On the matrix level, the soil therefore mainly consists of a mixture of ice, air and water. While the fraction of air depends on the soil moisture content at the end of autumn, the liquid water content (present as adsorbed

water on the soil particles) is temperature dependent. Towards the end of the period, temperature starts to increase again in response to higher air temperatures. However, no such increase is visible in the soil moisture records. It is supposed that this is owed to the effect of hysteresis (e.g. Spaans, E. J. A. and Baker, 1996; Tian et al., 2014).

Period II (Meltwater Infiltration Period) lasts from the onset of snow melt until zero-curtain conditions are reached in the ground. It is usually of short duration (0.5 to 1 month). In this period, strong snow melt is accompanied by a continuous increase in soil moisture and step-wise increases in ground temperatures. At the onset of this period, the pores are probably mainly filled with ice and air, while some liquid water is present as adsorbed water on the soil particles. As the snow cover reaches 0° C throughout its depth profile, snow melt water may percolate the entire column and reach the base. Initially, this melt water refreezes at the surface due to the still negative temperatures and basal ice layers are formed. These were observed in the field when trenches were dug in the snow and reported in other studies at the study site (Scherler et al., 2010). Consequently, snow melt water is ponded and runs off along the surface (HOF1).

After a certain water pressure is built up, water eventually infiltrates the top soil layers, refreezes and leads to a step-wise temperature increase as discussed in Section 5.4. In the soil moisture records this can be observed as a more or less sudden soil moisture increase (infiltration event) followed by a continuous soil moisture increase of smaller amplitude (increase of liquid water content due to ground temperature increase). However, while various step-wise temperature increases in ground temperature suggest various infiltration events, the soil moisture records do only show one large initial followed by a smaller but steady soil moisture increase. It is therefore suggested that initially, some pore air was replaced by water (initial soil moisture increase). In the following, only little water can further infiltrate and most of the soil moisture increase is due to ground ice melt. Finally, the ground temperature data suggests preferential flow as some deeper lying thermistors show earlier temperature increases than upper lying layers. For this, no further evidence was found in the soil moisture records as the sensors only measure soil moisture contents in the uppermost 60 cm.

Period III (Zero-Curtain Period) lasts from the onset of zero-curtain conditions in near-surface ground layers until the snow cover has vanished and ground temperatures are directly coupled to atmospheric conditions. During this period, snow melt continues to be strong while soil moisture values increase gradually or instantaneously to much higher soil moisture levels. As both the ground and the water from the snow pack are at 0° C, infiltrating water does no longer refreeze at the surface and in the ground (no temperature jumps are observable during this period). Consequently, the hydraulic conductivity is mainly a function of the progress of ice melt and the soil moisture content.

During the Zero-Curtain Period, no daily variation and a continuous increase in the soil moisture contents can be observed. This stands in contrast to the high variability of the water supply from the snow pack which usually peaks in the afternoon of warm days and is lowest during the night or during cold periods. From this follows that water drains very slowly, only little air is present in the soil (saturated conditions), and that the soil moisture content is a function of the ice content (inversely related). As a result, surface runoff (SOF1) occurs at local depressions below the snow cover during times of intense snow melt. Surface runoff has been observed and ripple sounds have been noticed at certain locations along snow trenches that have been dug to install the ERT profile lines. As the ice content decreases, the amount of bulk water in the pores increases. Consequently, water most probably also flows downslope laterally (SSF1). The highest hydraulic conductivities and thus the highest flow rates can be expected towards the end of the period and near the soil surface, where the ice melt is most advanced and the pores are thus better connected.

Period IV (Snow-Free Period) is during the time of snow-free conditions. It is characterized by a high variability in ground temperatures and soil moisture contents, which is attributed to the direct coupling to atmospheric conditions. During this period, ground temperatures are above 0° C and the soil moisture contents reach their annual maxima. Therefrom follows, that on a matrix scale no ice is present and the pores are filled with water and air in highly variable composition. Two main sources of soil moisture can be distinguished: First, a soil column may be influenced by lateral inflow of upper lying snow patches, particularly at the beginning of the snow-free period as the snow cover retreats heterogeneously. In this case, soil moisture shows daily variation with peak values in the afternoon. Secondly, infiltration of rain water leads to higher soil moisture contents during precipitation events.

Highest soil moisture values (probably close to saturation) are reached at the beginning of the Snow-Free Period during times of strong snow melt as well as throughout the period during intense and long lasting precipitation events. Runoff model results in contrary suggest that snow melt intensities are considerably lower than those of precipitation events. The saturated conditions during the time of snow melt water infiltration can therefore be attributed to the relatively shallow thaw depths which lead to the ponding of water near the surface. As a consequence, bulk water is present even in near-surface soil layers. Later in the period, when upper lying snow patches have vanished and thaw depths have increased, more water is needed to saturate the whole soil column and lead to saturated conditions even near the surface. Therefore, only intense and long lasting precipitation events lead to saturated conditions near the surface.

The same effect can be seen for the troughs in the soil moisture records. In general, soil moisture contents drop quickly, owing to the rather low matric potential of the sandy gravel. As such, low levels in soil moisture are reached shortly after the water supply through snow melt or precipitation has stopped. At the beginning of the period, when the thaw depth is shallow and lateral inflow of snow melt water from upper lying snow patches dominate, the troughs in the soil moisture records are the highest. This can be explained by high replenishment rates (daily replenishment) as well as a ponding effect and an effective capillary rise of soil water towards the soil surface. After the disappearance of upper lying snow patches and the increase of the thaw depths, the troughs in the soil moisture records reach the lowest values. This is explained by high infiltration depths (and thus ineffective capillary rise to the surface) as well as low replenishment rates (irregular precipitation events). Ultimately, lowest soil moisture values are reached after long periods of dry conditions due to evaporation at the surface.

Chapter 7

Resistivity Regime

In the following, the results of the ERT measurements are presented. First, some general characteristics of apparent and specific resistivities of the SCH profile line are presented. It is followed by specific resistivity and resistivity change plots of various profiles to illustrate the spatial distribution of soil moisture under different geological, meteorological and soil moisture conditions. Finally, the results are discussed in more detail.

7.1 Apparent Resistivity

In Figure 7.1, the apparent resistivities at four near-surface locations (first depth level) along the SCH profile line are shown for summer 2014. The four locations correspond with the locations of the boreholes whereas the red and green lines correspond to the locations of SCH5198 and SCH5000/SCH5200, respectively. SCH measurements were usually conducted at 08:00 h. They are compared to the volumetric soil moisture measurements (SMT and PICO64). In general, resistivities are high between the onset of the measurements until mid-August. They then drop by about 50 Ohm m and stay at this level until the end of October, when they start to increase again. Resistivities at SCH5000/SCH5200 are generally higher than at SCH5198.

At the beginning of the measurements, when soil moisture is still high and shows daily cycles, only little day-to-day variability is seen in the ERT data. This might be due to the fact that measurements are conducted always at 08:00 h and therefore usually cover the same time frame of the daily soil moisture cycle. Day-to-day variability becomes higher after this initial phase and reflects all major and some smaller precipitation events. While soil moisture contents increase, resistivities decrease. Furthermore, phases of drying-up are represented as phases of gradually increasing apparent resistivities.

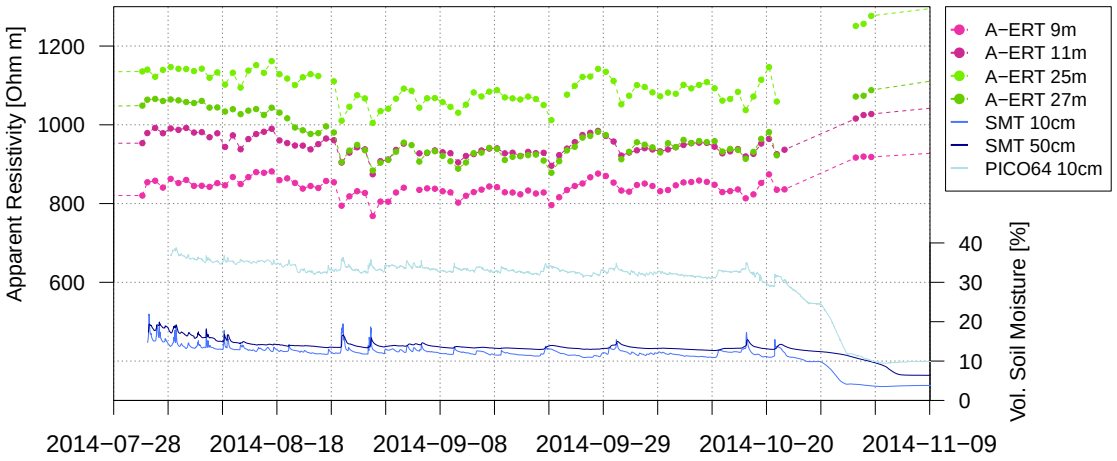


Figure 7.1: Apparent resistivities at four near-surface locations along the SCH profile line in vicinity of the boreholes in summer 2014 (upper part) opposed by soil moisture measurements of the SMT and PICO64 sensor (lower part).

7.2 Specific Resistivity

Figure 7.3 shows inverted specific resistivities along two virtual boreholes in vicinity of SCH5198 and SCH5000/SCH5200. The squares show the minimum and maximum, the circles show the 25- and 75-%-quartiles and the triangles show the median of all resistivity values at a specific depth of investigation. The data covers the period of the 31st of July to the 15th of October 2014. At SCH5198, surface resistivities are in the range of 800-1200 Ohm m. From 2 m depth downwards, they sharply decrease and reach minimum values in 4 m depth ranging from 500 to 600 Ohm m. Resistivities increase again further down and reach maximum values in 10 m depth ranging from 1300 to 1500 Ohm m. This bulging shape to the left side (decreasing resistivity) suggests a layer of fine grained material on top of bedrock. Variability is the highest in the top 2 m and stays constant downwards.

At SCH5000/SCH5200, resistivities range from 1000 to 1400 Ohm m at the surface. In 2 m depth, they sharply increase to a range of 1200 to 1800 Ohm m. From there on downwards, the median stays the same but the variability constantly decreases until in 5 m depth, from where resistivities range from 1500 to 1600 Ohm m. In comparison to SCH5198, resistivities are generally higher, particularly between 2 and 9 m depth. This suggests, that bedrock is much closer to the surface, only overlain by a small layer of debris. Noticeably, a region of high resistivity variability exists between 2 and 4 m depth as opposed to SCH5198, where the variability stays rather constant with depth.

Logarithmic percentage changes in specific resistivity along two virtual boreholes in vicinity of SCH5198 and SCH5000/SCH5200 are shown in Figure 7.3. Percentage changes are calculated from successive measurement pairs within the period of the 31st of July to

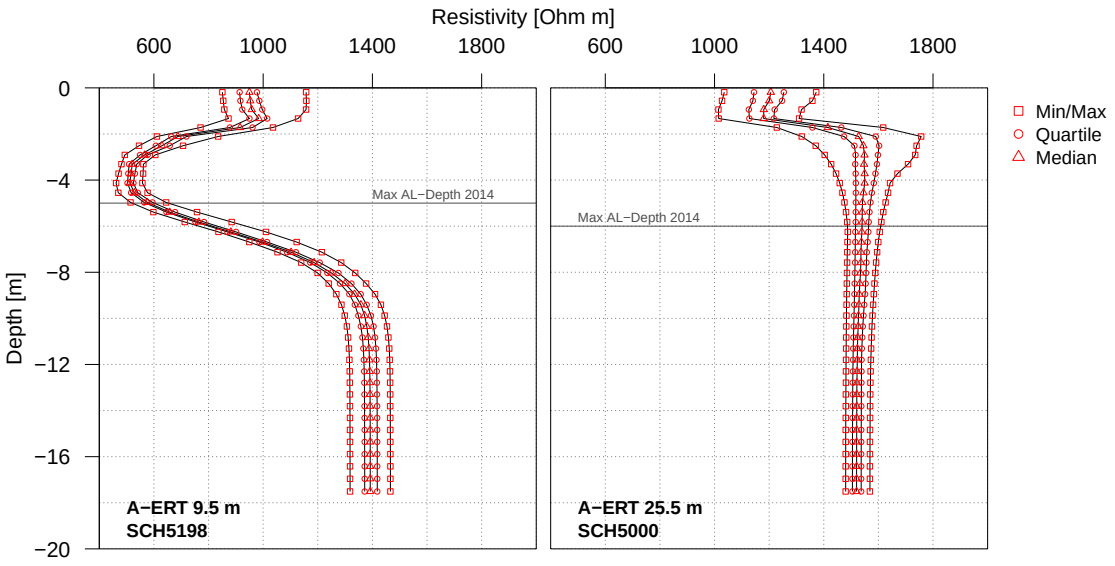


Figure 7.2: Specific Resistivities along two virtual boreholes in the vicinity of SCH5198 (left) and SCH5000 (right). The triangles show the median, the circles show the 25- and 75-quartiles and the squares show the minimum and maximum values for a specific depth of investigation. The data covers daily measurements during the period of the 31st of July to the 15th of October 2014.

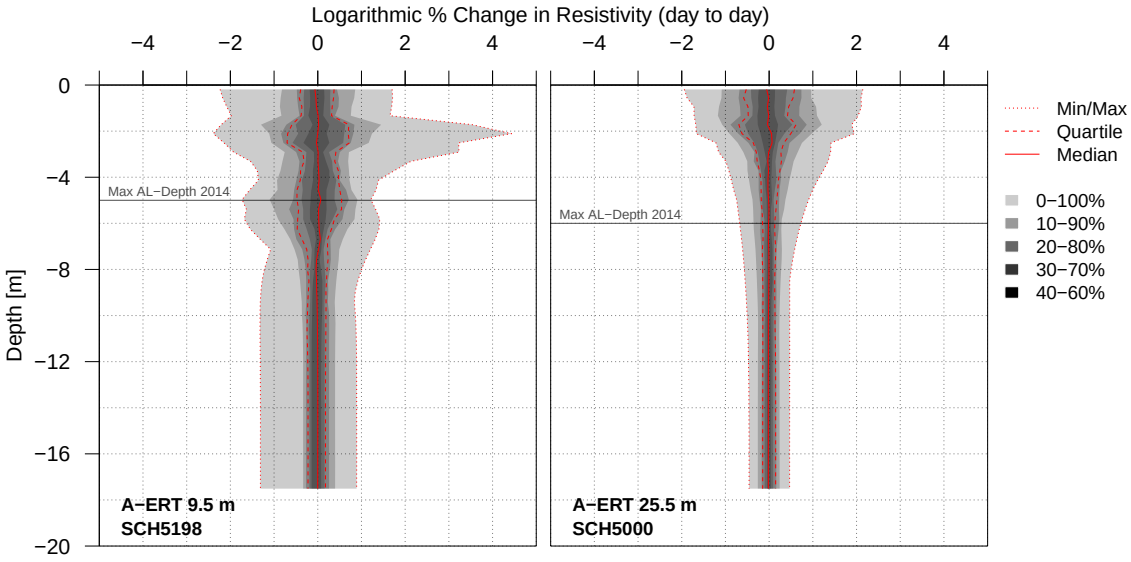


Figure 7.3: Logarithmic percentage change in specific resistivity of successive measurements along two virtual boreholes in the vicinity of SCH5198 (left) and SCH5000/SCH5200 (right). The different levels of transparency of grey represent each a 10-%-percentile, whereas the dotted, dashed and solid lines represent the minimum/maximum, 25/75-%-percentiles and the median, respectively. The data covers daily measurements during the period of the 31st of July to the 15th of October 2014.

the 15th of October. During this period, measurements were conducted daily. The different levels of transparency of grey represent each a 10-%-percentile of all measurements at a specific depth of investigation. The red lines correspond to the minimum and maximum values, the 25 and 75-%-quartiles as well as the median. High day-to-day changes can be attributed to water infiltration and outflow.

At SCH5198, day-to-day changes are highest in the upper 6 m and decrease below, ranging usually from -2 to +2 % with extreme values at 2 m depth of up to +4 %. Peaks are visible at 2 and 5 m depth, whereas below 8 m depth, the range of day-to-day-changes becomes uniform. At SCH5000/SCH5200 in contrary, day-to-day changes are highest in the upper 3 m, ranging from up to -2 to +2 %. Uniform day-to-day changes are reached below 7 m. In general, large day-to-day changes reach further down at SCH5198.

7.3 Electrical Resistivity Tomograms

In this section, specific resistivity tomograms and resistivity change plots of the SCHpara and SCVpara profile lines are presented, in order to assess the spatial distribution patterns of different soil moisture regimes and conditions. Furthermore, resistivity change plots of the SCH profile line during the identified infiltration events (see Figures 5.10 and 5.11) are presented to assess the spatial soil moisture patterns during these events.

7.3.1 Specific Resistivities of all Profile Lines

An inverted resistivity tomogram of the SCH profile line is shown in Figure 7.4. The locations of the boreholes SCH5198 and SCH5000 are marked with black lines. The lowest resistivity values are found near the surface and in a zone of particularly low resistivities in the left part of the profile. In this zone, resistivity values between 300 and 500 Ohm m reach down as low as 6 m depth. SCH5198 is located within this zone, whereas at SCH5000, resistivities at the same depth are generally higher (ranging between 1500 and 1700 Ohm m). According to Hauck (2001), the differences in resistivity at the boreholes are due to thick layer of fine grained debris at the location of SCH5198. In the middle part of the profile, a second zone of low resistivities exists, probably also corresponding to a body of fine grained debris. In the right part of the profile, resistivities at depth are generally higher and the bedrock is close to the surface.

In Figure 7.5, inverted resistivity tomograms of the SCHpara and SCVpara profile lines are shown. The black lines mark the positions of the boreholes SCH5198, SCH5000 and SCH5200, and the red arrows show the crossing points of other profile lines. SCHpara1_ext shows a similar picture as the one in Figure 7.4. The lowest resistivity values

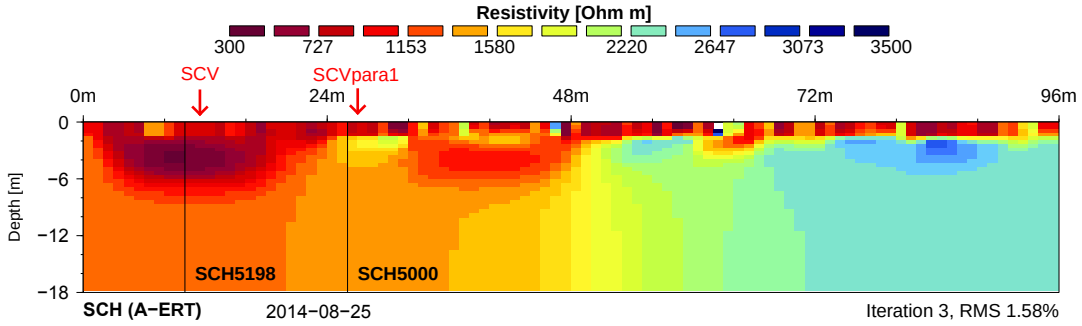


Figure 7.4: Inverted resistivity tomogram of the A-ERT profile line. The two black lines mark the positions of the boreholes SCH5198 and SCH5000

are found at the surface and in vicinity of SCH5198. However, resistivity values seem slightly lower than in Figure 7.4 which might be due to the inversion process.

SCHpara2 is measured about 25 m upslope and parallel to the SCH profile line (see Figure 4.1). Again, the lowest resistivities are found at the surface, suggesting a layer of finer grained material on top of bedrock. In contrary to the SCH profile line however, the bedrock is closer to the surface and the layer of fine-grained material is only 1 to 2 m thick. One zone of particularly high resistivities is found between 10 and 15 m horizontal distance at 2 m depth. In this area, the profile line runs over an outcrop. Between 27 and 30 m, a second zone of high resistivities is located near the surface. This corresponds to a zone of big boulders and the high resistivities can be attributed to the higher air content.

SCHpara3 is located between the SCH and SCHpara2 profile lines (see Figure 4.1). The right half of the profile is similar to the previous profile lines where a layer of less resistive fine-grained material of about 1 m thickness lies above more resistive bedrock. In the left part of the profile, a strong high resistive anomaly can be observed at the surface between 8 and 11 m horizontal distance. This zone corresponds to a zone of big boulders and the high air content may be responsible for the high resistivities. Just below lies a zone of very low resistivities ranging down to 300 Ohm m. This may either be a zone of finer grained material or an inversion artefact due to the very high resistivity contrast.

SCVpara1 runs perpendicular to the previous profile lines and crosses all of them along the profile line (see Figure 4.1). At its lower end, it crosses the boreholes SCH5000 and SCH5200. Between 0 and 4.8 m, the profile line runs over an outcrop covered by a layer of fine-grained debris on top. Between 4.8 m and the boreholes, the profile line crosses a mixed zone of fine-grained material and blocky parts. From the boreholes downwards, the surface material is fine-grained. These field observations are clearly seen in the ERT tomogram, where the outcrop and blocky material appear as high resistive areas and the fine-grained material as more conductive.

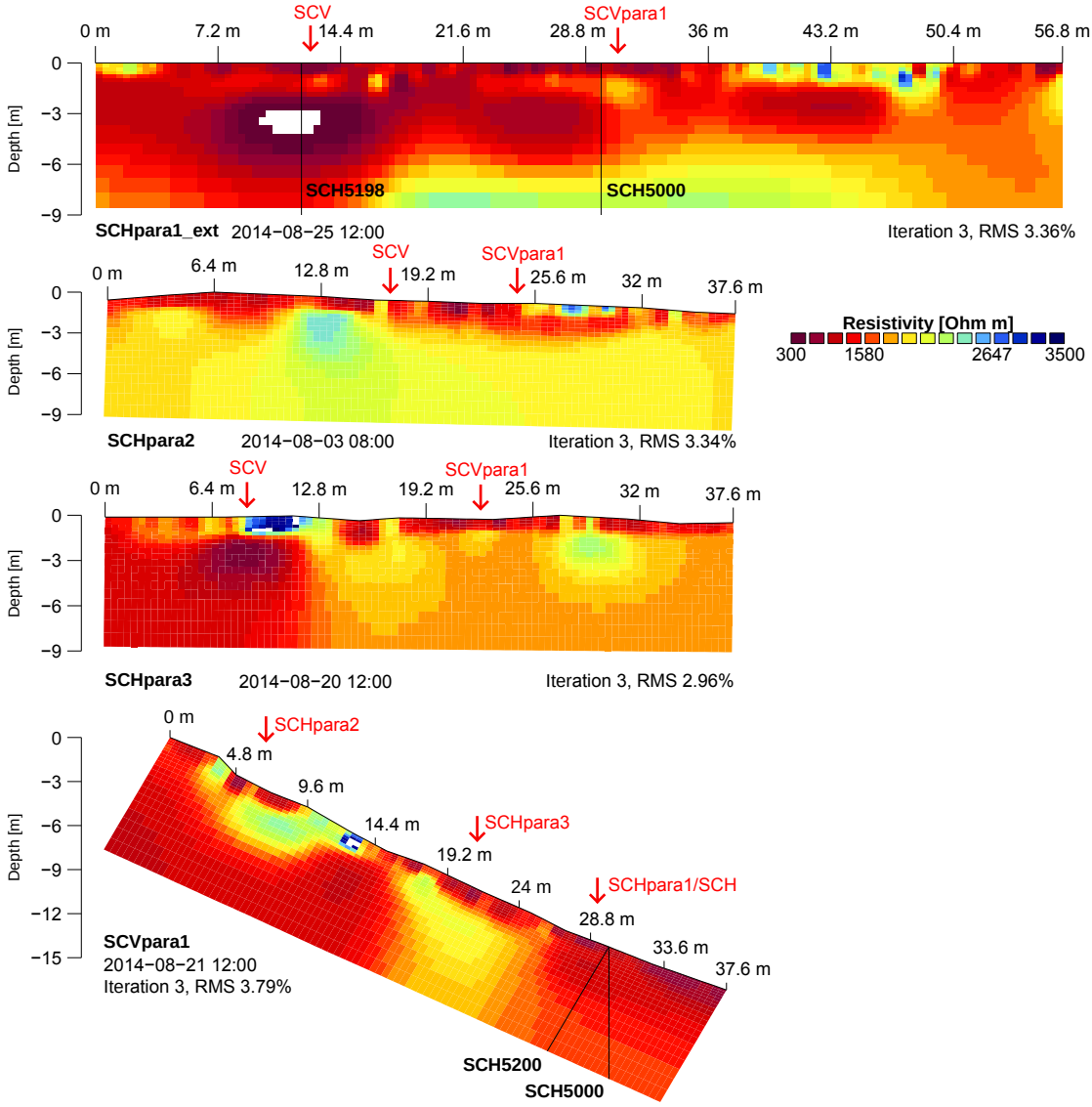


Figure 7.5: Inverted resistivity tomograms of the SCHpara and SCVpara profile lines. The black lines mark the positions of the boreholes SCH5198, SCH5000 and SCH5200. The red arrows indicate the crossing points of the profile lines.

7.3.2 SCHpara and SCVpara Resistivity Change

In the following, specific resistivity tomograms and logarithmic percentage change in specific resistivities are shown for different profile lines of the SCHpara and SCVpara profiles. The inversions of the SCHpara and SCVpara profile lines were carried out using a time-lapse inversion scheme. The resistivity change plots are discussed with regard to the meteorological, soil moisture, runoff and ground temperature data to attribute the signals to infiltration events or changes in the ground ice content.

Figure 7.6 shows three ERT measurements along the SCHpara1 profile line. The top panel shows a specific resistivity tomogram of the 3rd of August 2014, which was rather

dry and cold. Most of the profile was still covered with snow (indicated by the blue lines) and only a small part of the profile was snow-free. The snow-free part was very moist from the melting of the upslope snow pack: Surface runoff was observed between 6 and 10 m and the soil samples show high water contents (32 vol. %) in this area. At SCH5198, ground was thawed until 0.8 m depth whereas at SCH5000/SCH5200, the near-surface layers were still frozen.

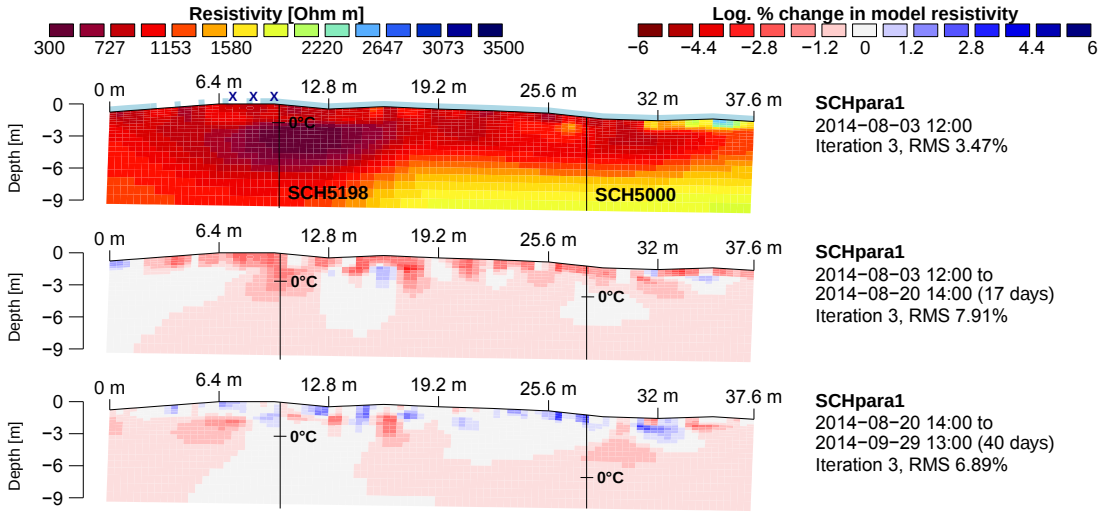


Figure 7.6: Resistivity tomogram at SCHpara1 (top panel) and logarithmic percentage change in specific resistivity at three points in summer 2014 (other panels). The black lines indicate the positions of the boreholes SCH5198 and SCH5000. The solid and dashed blue lines at the surface show snow covered and upslope snow covered areas, the blue crosses show areas with surface runoff.

The middle panel shows the resistivity change to the 20th of August 2014 (17 days), which was again rather dry and cold. The whole profile was snow free by then. At SCH5198 and SCH5000/SCH5200, ground had thawed until 2 m depth. Although less soil moisture content was observed near the surface, resistivity decreased in most of the profile, and the strongest decrease (up to -3 %) can be observed near the surface (upper 1 to 2 m). It corresponds well to the depth of the active layer measured at all three boreholes and is thus attributed to the melting of ground ice. Furthermore, it can be stated that at the 3rd of August, most snow melt water infiltration was restricted to the uppermost layers.

The lowest panel shows the resistivity change from the middle panel to the 29th of September 2014 (40 days). Both dates inhibit similar meteorological conditions (rather warm and dry). Ground had thawed until more than 2.5 m at all boreholes. Increasing resistivity (up to +4 %) can be observed within the upper 1 to 2 m, whereas at some locations, zones of resistivity decrease can be observed below the surface layer. The resistivity increase is explained by a drying of the near-surface layers, the zones of resistivity decrease are attributed to ground ice melt.

Figure 7.7 shows two ERT measurements along the SCHpara1_ext profile line. The upper panel shows a specific resistivity tomogram of the 25th of August 2014 at 12:00 h, which was dry. Only the very left part of the profile line is covered with snow. Both SCH5198 and SCH5000 show an active layer thickness of about 2 m. The lower panel shows the resistivity change to the 26th of August 2014 at 10:00 h (22 hours). It was conducted during a long and intensive precipitation event (R_7, see Figure 5.11). Surface runoff was observed near SCH5198 and in the very right of the profile. Resistivities decreased in the whole profile ranging up to -3 % and down to 6 m depth. The resistivity decrease was more pronounced at SCH5198 than at SCH5000. This difference in resistivity can be attributed to higher infiltration rates at SCH5198 due to the thicker layer of unconsolidated material present here (see Figure 7.4).

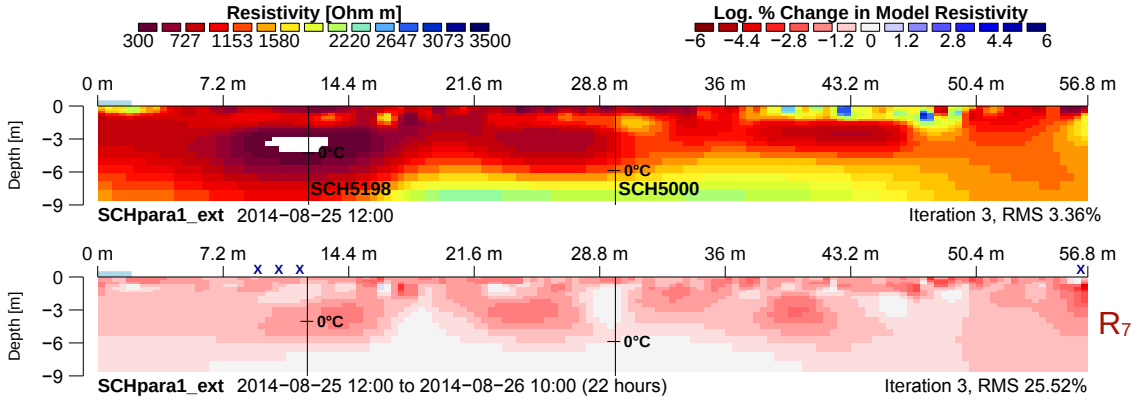


Figure 7.7: Resistivity tomogram at SCHpara1_ext (top panel) and logarithmic percentage change in specific resistivity at two points in summer 2014 (lower panel). The black lines indicate the positions of the boreholes SCH5198 and SCH5000. The blue line at the surface shows snow covered, the blue crosses show areas with surface runoff.

Two ERT measurements along the ERTpara2 profile line are shown in Figure 7.8. The top panel shows a specific resistivity tomogram of the 2nd of August 2014 at 08:00 h, which was warm and dry. Both ends of the profile are snow-covered (indicated by the blue lines), whereas in the first half, a part of the profile is below an upslope snow patch (dashed blue line). The middle part is snow-free and has presumably been snow free for at least some days. At SCH5198, ground has thawed until 0.8 m depth, whereas at SCH5200/SCH5000 (snow covered), the whole profile is still frozen.

The lower panel shows the resistivity change to the same day at 14:00 h (6 hours). Due to the warm weather, snow melt is strong and the soil moisture measurements located 25 m downslope the ERT profile show a sharp increase by as much as 3 vol. %. Furthermore, surface runoff is visible at 12.8 and 22 m. The temperature profile at the boreholes does not show considerable changes. Resistivities decrease considerably by up to -4.5 % in the upper 1 to 2 m of the snow-free areas which is related to the infiltration of snow melt

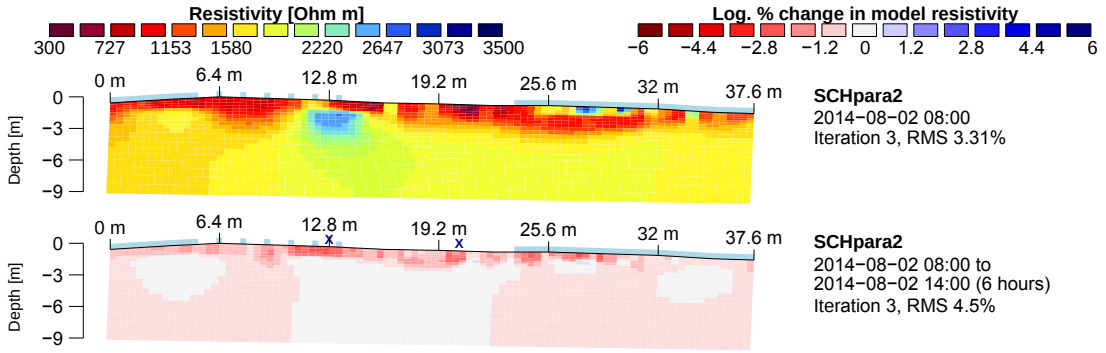


Figure 7.8: Resistivity tomogram at SCHpara2 (top panel) and logarithmic percentage change in specific resistivity at two points in summer 2014 (lower panel). The solid and dashed blue lines at the surface show snow covered and upslope snow covered areas, the blue crosses show areas with surface runoff.

water. Most soil moisture change can be observed in a thin soil layer which lies atop an outcrop (10–14 m horizontal distance) and which receives a lot of snow melt water from the upslope snow patch. Next to it, water drains deeper but the soil shows less saturation. Below the snow covered parts, only little changes are observable, which can be attributed to no or little saturation changes due to ponding by ice or already saturated conditions before.

On Figure 7.9, three ERT tomograms along the ERTpara3 profile line are presented. The upper panel represents a specific resistivity tomogram of the 20th of August 2014, which was dry and cold. Soil moisture records do not show elevated moisture records; soil samples of the following day show volumetric soil moisture contents of 15 to 25 vol. %. Only a small part of the profile was snow-covered. SCH5198 and SCH5000 were both thawed until 2 m depth.

The middle panel shows the resistivity change to the 27th of August 2014 (7 days). It was conducted right after a strong precipitation event, yet soil moisture values indicate that most of the upper soil moisture had already drained. The ground temperature regime was similar to the precedent measurement. Resistivity however had decreased considerably in up to 3 to 4 m depth. Less resistivity decrease and thus smaller soil moisture content increase is observed in zones of bedrock and at the former location of the snow patch.

The lower panel shows the resistivity change from the middle panel to the 30th of September 2014 (34 days). The weather was dry and cold and the soil moisture records were in a similar range. The boreholes show an increased active layer depth but slightly colder (yet positive) temperatures in the surface layers. Resistivities have increased in most of the upper 1 m of the profile, which can be related to the drying of these layers. Between 6.4 and 12 m horizontal distance, a resistivity increase of up to +3 % can be observed until 3 m depth, which corresponds to a drying of a zone of loose debris. In the

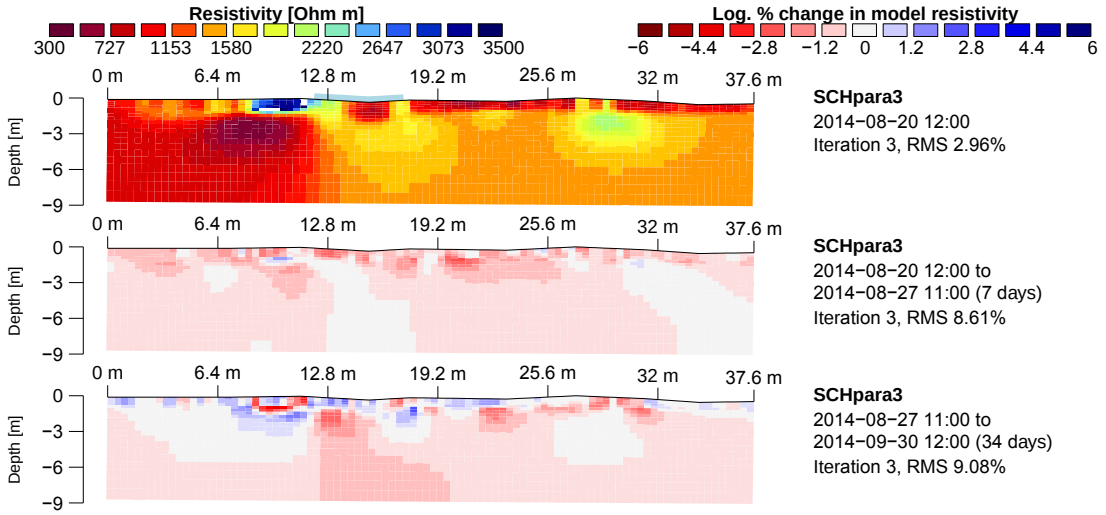


Figure 7.9: Resistivity tomogram at SCHpara3 (top panel) and logarithmic percentage change in specific resistivity at three points in summer 2014 (other panels). The solid blue line at the surface shows snow covered areas.

rest of the profile, resistivity decrease is visible at depth, which corresponds to the thawing of the active layer.

Figure 7.10 shows plots of three ERT measurements along the SCVpara1 profile line. The upper panel shows a specific resistivity tomogram of the 24th of August 2014, which was relatively cold and dry. A slight increase in soil moisture is visible due to the melting of a few cm of snow which had fallen in the preceding days. SCH5198 and SCH5200 show an active layer depth of 2 m.

On the second panel, the resistivity change to the 26th of August is visible (2 days), which was measured during a long and intensive precipitation event (R_7, see Figure 5.11). Strong resistivity decrease of up to -3 % can be seen in the whole profile. In the upper part of the profile, resistivity decrease reaches as low as 3 m. In the middle part, the pattern is more complex whereas the resistivity decrease partly reaches even further down. In the lowest part, water infiltration is restricted to the uppermost 1 to 2 m. At the boreholes, it reaches as low as 2 to 3 m.

The lower panel shows the resistivity change of the middle panel to the 30th of September 2014 (37 days). Soil moisture values are slightly more elevated due to the melting of a shallow layer of snow. At both boreholes, the active layer has reached its maximum thickness (5 and 3 m at SCH5000 and SCH5200, respectively). On the resistivity change plot, large resistivity decreases are visible throughout the profile, however they are mostly restricted to the middle part. It is suggested that this is due to the higher active layer depth and the corresponding more efficient infiltration of snow melt water. No significant changes are visible near the boreholes.

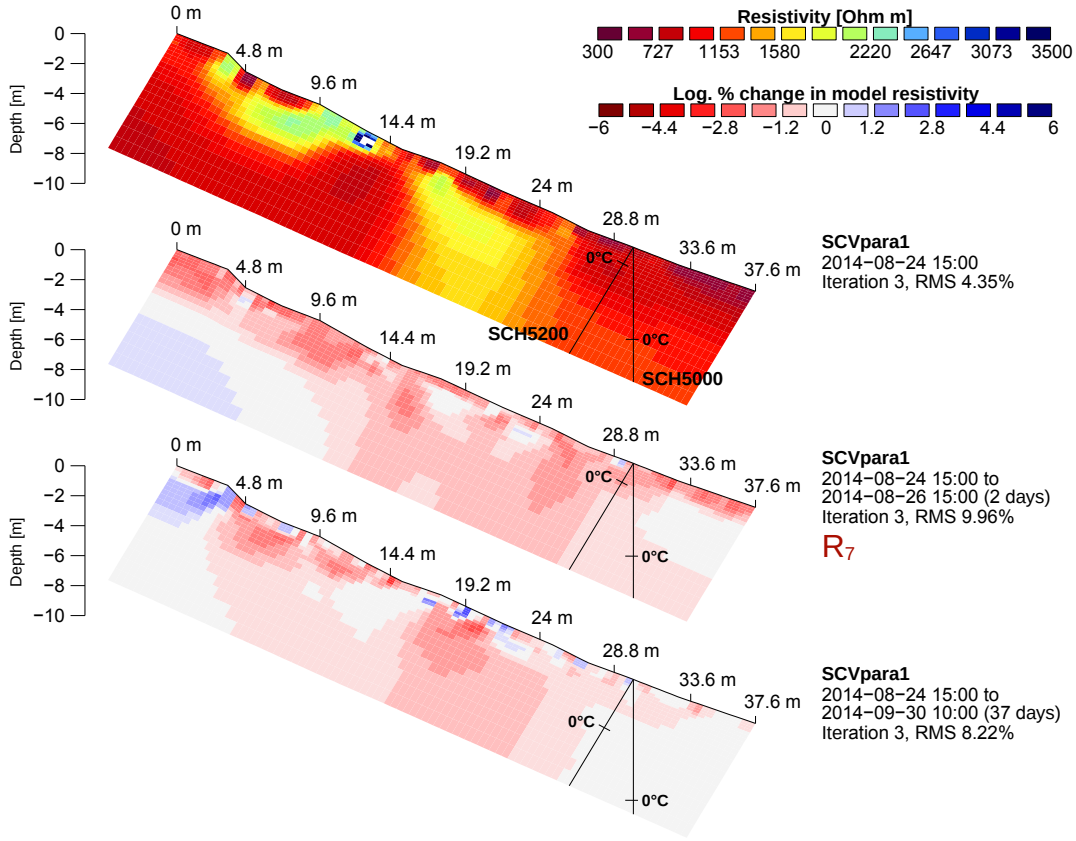


Figure 7.10: Resistivity tomogram at SCVpara1 (top panel) and logarithmic percentage change in specific resistivity at three points in summer 2014 (other panels). The black lines indicate the positions of the boreholes SCH5200 and SCH5000

7.3.3 SCH Resistivity Change

On Figure 7.11, specific resistivity tomograms and plots of logarithmic percentage change in specific resistivity are shown for the A-ERT profile line (SCH). The resistivity change plots coincide with infiltration events of snow melt or rain water. The red labels next to the resistivity change plots correspond with the event labels of figures 5.10 and 5.11. Measurements were usually conducted at 08:00 h, the first measurement (31st of July 2014) took place 16:00 h. In the following, the spatial patterns of resistivity changes particularly around the boreholes and the meteorological and moisture conditions are discussed in more detail. For details to the labelled infiltration events, see Section 5.3.2.

The first measurements show the resistivity difference from the 31st of July (16:00 h) to the 1st of August 2014 (08:00 h). During this time, most of the profile was still snow covered, except for a short stretch around SCH5198. The warm and dry weather led to strong snow melt in the afternoon of the 31st of July (not covered by the soil moisture data). The active layer is about 0.8 m at SCH5198, whereas at SCH5000, all the profile is still frozen. A zone of strong resistivity increase is visible between 0 and 14 m stretching

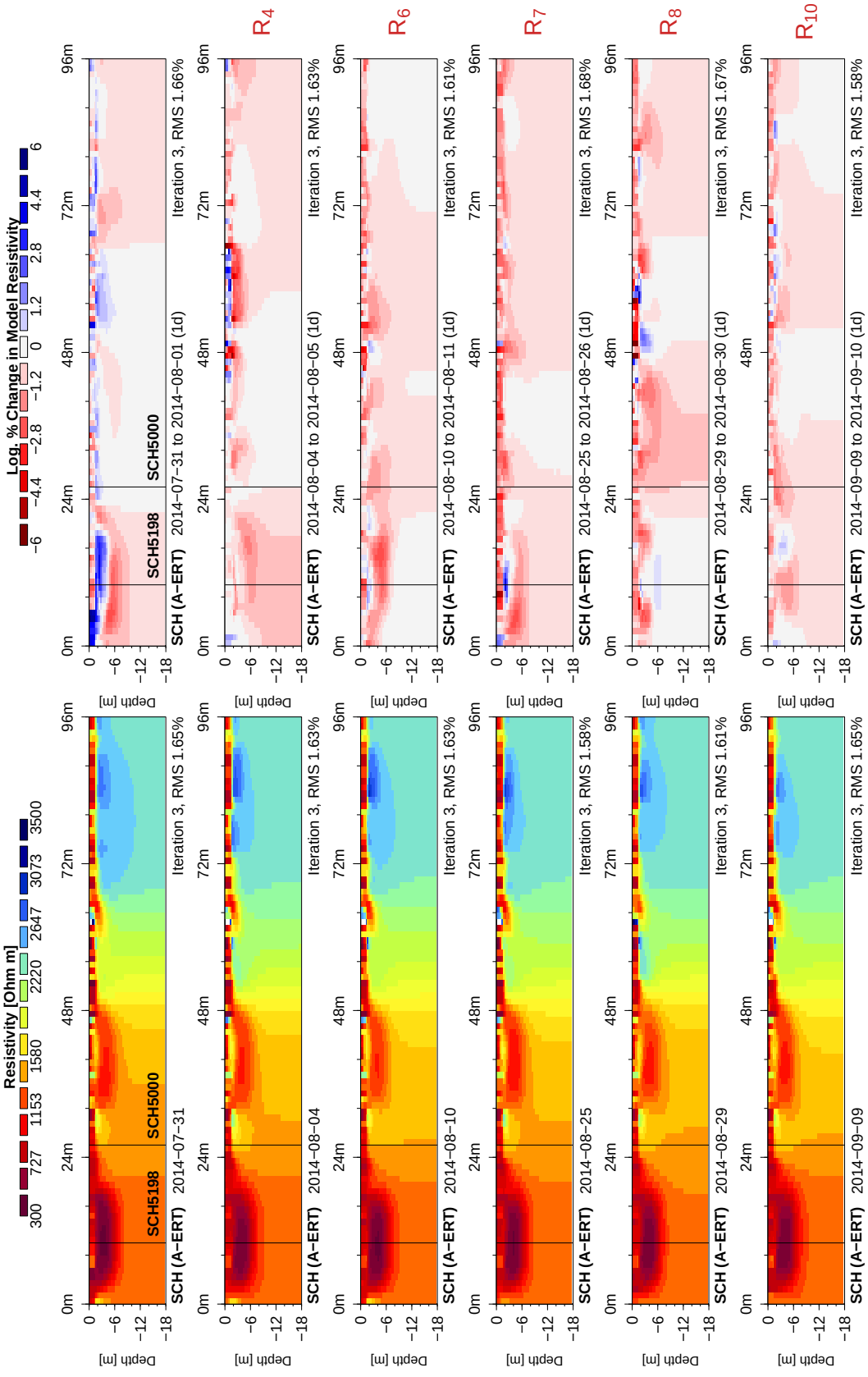


Figure 7.11: Specific resistivity tomograms (left column) and logarithmic percentage change in specific resistivity (right column) of the A-ERT profile line SCH. The black lines indicate the locations of the boreholes, the red labels on the right correspond with the labels of the infiltration events defined above.

to about 4 m depth which can be attributed to the drainage of snow melt water. Below this zone, strong resistivity decrease can be seen, which however might be an inversion artefact due to strong resistivity contrasts. A second zone of strong resistivity increase exists between 52 and 60 m reaching as low as 6 m. In the rest of the profile, resistivity decrease and thus melt water infiltration during the snow melt event is visible within the uppermost 1 to 2 m.

The second set of measurements was conducted at the 4th and 5th of August 2014 and covers the infiltration event R_4. A zone of resistivity decrease up to -4 % is visible around SCH5198 until 8 m depth although the active layer reaches only as low as 2 m. Other zones of resistivity decrease are seen in the rest of the profile ranging down as low as 4 m. At SCH5000/SCH5200, no particular resistivity changes are visible, while only the near-surface layers are thawed.

The third set of measurements shows the resistivity difference between the 10th and the 11th of August 2014 which corresponds to the infiltration event R_6. A strong precipitation event in the first half of the 11th of August leads to saturated conditions during the second measurement. A zone of strong resistivity decrease of up to -4.5 % and extending to about 7 m depth is again visible around SCH5198, where the active layer thickness is about 1.2 m. At SCH5000/SCH5200 infiltration less pronounced and shallower, while the active layer reaches deeper until 1.6 m. In the rest of the profile, resistivity decrease can be seen in the uppermost 2 m down to 4 m depth.

The resistivity difference between the 25th the 26th of August 2014 is depicted in the fourth set of measurements which corresponds to the infiltration event R_7. A remarkably strong and long lasting precipitation event leads to highly saturated conditions on the second date of measurements. Again, a zone of particularly high resistivity decrease is found near SCH5198, extending down to 7 m and depth and amounting up to -3 % (active layer depth 2 m). At SCH5000/SCH5200, the resistivity decrease is again shallower and less pronounced (active layer depth 2 m). In the rest of the profile, resistivity decrease is most pronounced in the uppermost 2 to 4 m.

The fifth set of measurements shows the resistivity difference between the 29th and the 30th of August 2014 which covers the infiltration event R_8. A strong precipitation event during the night leads to saturated conditions early on the 30th of August 2014. On the resistivity change plot it is visible that most of the resistivity decrease is concentrated to the uppermost 2 to 4 m. No particular patterns are visible around the boreholes.

The last set of measurements covers the resistivity difference between the 9th and the 10th of September 2014 which corresponds to the infiltration event R_{10}. A relatively weak precipitation event over night leads to higher soil moisture contents on the 10th

of September. On the resistivity change plot it can be seen, that resistivity decrease is less pronounced than at previous events. Nevertheless they reach down as low as 7 m at SCH5198 and 6 m at SCH5000 while active layer depths are at 2.5 and 4 m, respectively.

7.4 Discussion

In this section, the spatial soil moisture distribution patterns are discussed in more detail. First, general distribution patterns are discussed followed a discussion of the soil moisture conditions at the boreholes.

7.4.1 Spatial Soil Moisture Distribution

With the ERT measurements, two soil conditions corresponding to the sol moisture regimes discussed in Section 6.5 could be studied. First, when the surface is still snow covered and the soil is at zero-curtain conditions (corresponding to Period III), only little additional soil moisture infiltrates the ground during times of strong snow melt. This can be seen for example on Figure 7.8 in the snow-covered areas which show only little resistivity change in contrast to snow-free areas. Furthermore, infiltration is restricted to the top most meters. This is in accordance with the findings of the soil moisture records which for this period show little daily soil moisture variation and for which saturated conditions were suggested. Spatially, these conditions apply to snow covered areas while in the transition areas to snow-free conditions, larger resistivity changes as observed in the snow-free areas can be detected.

During snow-free conditions (corresponding to Period IV) in contrary, high variation in soil moisture conditions can be observed in relation to the infiltration of snow melt or precipitation water. During this period, two impeding layers can be distinguished. First, the active layer impedes water flow due to a highly decreased hydraulic conductivity as part of the pore space is ice filled. As the active layer grows over the turn of the snow-free period, the infiltration depth of a soil column increases too. This is in agreement with the the soil moisture records and field observations which show higher near-surface water contents when the active layer is still shallow. The second impeding layer is the base rock topography. It becomes effective, when the active layer drops below the base rock surface. When the base rock surface is locally higher than the surrounding base rock or active layer surface, more water is concentrated near the surface compared to the surrounding area, as seen in the ERT data. However, both the active layer depth and the base rock topography do not completely prevent water to infiltrate further downwards and some water movement can be observed below these limits. Due to the pore ice content in frozen

soil and the smaller pore space in the bedrock, the hydraulic conductivity and thus the water flow are highly reduced.

Particularly during the snow melt period, the spatial variability of soil moisture conditions can be tremendous in relation to the complex melt-out pattern of the snow cover. During this time, the snow cover has a strong control over thaw depths and consequently the infiltration depths of soil moisture. Furthermore, it is a major source of soil moisture during this time. After most of the snow cover has ablated, the geological conditions and hillslope water flow are the dominant control factor for the spatial distribution of soil moisture.

7.4.2 Situation at the Boreholes

From the resistivity change plots it is visible that the highest day-to-day resistivity changes at SCH5198 and therefore most infiltration of soil water was limited to the uppermost 5 to 6 m which roughly corresponds to the bedrock depth. Maximum resistivity decreases are found around 2 and 5 m depth. Maxima in the resistivity change are attributed to laterally flowing water as such layers are expected to bear the highest soil moisture contents and thus the highest resistivity decreases. The maximum at 2 m is thought to be the lateral flow depth during the time of snow melt infiltration from upslope snow patches early in summer, when thaw depths are still shallow. The maximum at 5 m depth is attributed to the lateral flow depth in mid to late summer, when the active layer has reached the bedrock depth and most lateral flowing water flows downslope above the bedrock topography.

Further below, the variability in resistivity changes decreases continuously until a depth of 7 m, which is assumed to be the maximum depth of water infiltration. At this depth, only little water infiltrates due to the presence of pore ice and due to the impeding effect of the base rock. Further below, the day-to-day resistivity changes are small and attributed to temperature changes. These findings are in accordance with the analysis of the thermal orbits (see Section 5.3.3), which suggest a maximum infiltration depth of 7 m and a continuous decrease of non-conductive heat exchange with depth.

Finally, as most of the water infiltration takes place within the relatively thick layer of loose debris, the soil water at depth has probably a relatively long resting time due to the high pore volume and no direct evaporative loss. At the surface in contrary, higher resistivities are found although the material seems to be similar. This might be an indicator for a higher air content in the pores due to a larger size of individual pores (lower compaction, therefore lower retention capacity due to a smaller specific surface) and a higher evaporative loss of soil moisture as it is directly coupled to atmospheric conditions.

The highest day-to-day resistivity changes at SCH5000/SCH5200 are found within the uppermost 2 m which again corresponds to the bedrock depth. It is also at this depth, where the maximum in day-to-day resistivity changes are found. It is thus assumed that water mostly runs along the bedrock topography near the surface. Below, the variability in resistivity changes decreases until about 5 m depth which is assumed to be the maximum infiltration depth of soil water. Further below, resistivities still vary, however to a much smaller extent and probably due to temperature changes only.

Again, most water infiltration and lateral flow occurs in the layer of fine debris. In contrary to SCH5198 however, the water is impeded close to the surface due to the shallow bedrock depth. As a consequence, water is concentrated near the surface which leads to higher soil moisture values at the surface. This is in accordance with near-surface apparent resistivities which show a higher variability in relation to precipitation/evaporation cycles (see Figure 7.1). At depth, conditions are relatively dry due to the low pore volume of the bedrock.

Chapter 8

General Discussion

In the following, the findings of the three preceding chapters are wrapped up and a synthesis on the thermal impact of soil moisture is drawn. In general, it is suggested that the energy balance at the surface and the subsequent conduction of heat in the ground are the most dominant factors in the thermal regime. However, the conduction of energy is mediated by soil moisture through latent and sensible heat fluxes and through the change of soil properties. In the following, their relative impact is discussed in more detail.

The greatest effect of soil moisture on the thermal regime was found through latent heat effects. These are most obvious during frozen conditions: As water infiltrates and refreezes in the subsurface, latent heat is released and increases the ground temperature. When the snow cover is still present, this is an important process for preconditioning the melt ground ice near the surface. It is assumed that this process continues to be effective at the base of the growing active layer. As such, water infiltrates in the ground at the base of the active layer and contributes to the active layer growth. As the temperature released is directly related to the amount of water which infiltrates and refreezes, this effect is more pronounced in subsurfaces with a higher matric potential. Furthermore, it is more effective where the ice content is lower. However, it is only present as long as water is able to refreeze and thus as long as the ground is below 0° C. It is thus believed that it rather preconditions active layer growth and that the complete melt of ground ice and thus the exceedance of zero-curtain conditions is only reached through the conduction of heat.

In autumn, the reverse is observable: When ground temperatures fall below 0° C, soil water starts to freeze and consequently releases latent heat. This energy needs to be conducted out of the soil in order for the soil to become frozen and for the ground temperature to further fall. As a result, periods of zero-curtain conditions are observable at the boreholes and the propagation of the freezing front is delayed.

During unfrozen conditions, latent heat effects are mainly observed near the surface: Water in the pores of near-surface soil layers is evaporated which acts as an effective heat sink. Consequently, less energy is available for conduction in the ground. This effect is more pronounced where the surface is wetter, which is the case at the beginning of the summer when the active layer is still shallow. At SCH5000/SCH5200 however, where the base rock is near the surface and water is concentrated near the surface throughout the year, it is believed that the wetter surface effectively reduces the propagation of energy in the ground. This may partly explain the reduced thermal variability at this borehole.

Sensible heat effects in contrary are much smaller. They are attributed to the infiltration of rain water. Temperature records show short-term increases which coincide with peak soil moisture contents and decrease again to precedent values simultaneously with the percolation of the rain water. Such temperature variations were mainly observed at SCH5198, while at the other boreholes, they only occurred early in the summer. This may be due to slower infiltration velocities and consequently longer resting times due to a higher matric potential at SCH5198. Secondly, the heat flow at SCH5000/5200 might be reduced due to a lower thermal diffusivity (due to different soil properties, see below). In this context, the role of the borehole casing needs to be assessed critically. While SCH5000 and SCH5200 are covered with a PVC pipe, SCH5198 is not covered. At SCH5000/SCH5200 this could contribute to the lower thermal conductivity between the soil and the thermistors. At SCH5198, water could infiltrate the borehole which then facilitates water flow downwards and to the thermistors.

Finally, soil moisture has an impact on the thermal properties of the soil. With an increasing soil moisture content, thermal conductivity and thermal diffusivity increase as well. This effect may significantly contribute to the differences in the thermal behaviour of the boreholes. Due to a higher matric potential of the thick loose debris cover at SCH5198, more water is retained at depth. Consequently, heat is conducted more effectively in depth leading to a higher thermal variability. At SCH5000/SCH5200 in contrary, the relatively dry bedrock has an opposing effect which could lead to a relatively low thermal variability.

The relative importance of these thermal effects can be highly variable, as shown by different studies in the arctic. While some studies found higher thaw depths in drier years due to reduced evaporation (Boike et al., 2008) or higher thaw depths in wetter years due to an increased thermal conductivity (Wright et al., 2009), others found no influence of soil moisture at all (Westermann et al., 2010). Wollschläger et al. (2010) demonstrated that the effects of soil moisture may even vary on small spatial scales. The effectiveness of the different thermal effects of soil moisture is shown to depend strongly on the soil's texture, the geologic setting and on the presence of hillslope water flow processes. In Alpine

Permafrost, where soils are very homogeneous and hillslope flow processes are complex, the spatial variability and thermal impact of soil moisture can therefore be tremendous.

Chapter 9

Conclusion

In the following, the main conclusions are drawn. Furthermore, an outlook for further work is given.

9.1 Conclusion

In this study, first the temporal evolution and spatial distribution patterns of soil moisture in mountain permafrost soils was assessed. A seasonal cycle of soil moisture conditions with four distinct regimes could be identified. In winter, ground freezes and soil moisture drops to the lowest annual values. During this time, no infiltration takes place. During the time of snow melt, two distinct periods of soil moisture increase can be detected. While the first increase is rather small and attributed to the infiltration of water into frozen ground, the second is larger and attributed to infiltration of water into ground at zero-curtain conditions. The fourth period denotes the time when the snow cover has completely ablated. In this period, soil moisture contents are highly variable, directly coupled to the atmosphere and show the highest annual values. These findings are in correspondence with another study at Schilthorn by Hilbich et al. (2011).

The presence of a snow cover was found to have great impact on the soil moisture regime. It insulates the ground from atmospheric conditions, prevents ground ice melt and is a major source of water during the time of snow melt. When the ground is snow covered two states of the ground are differentiated. Under frozen conditions, the infiltration and refreezing of soil water leads to variable hydraulic conductivities. As ice contents are still high, only little water may infiltrate and most water runs off at the surface. However, evidence for preferential flow into deeper soil layers was found. Under zero-curtain conditions in contrary, ice contents continuously decrease and soil moisture contents increase in response. However, hydraulic conductivity is still low and infiltration depths shallow.

Under snow-free conditions when the ground has thawed, soil moisture contents are directly coupled to atmospheric conditions. They may reach the highest values due to low ice contents and have the highest infiltration depths. The spatial snow melt pattern at Schilthorn was found to be very heterogeneous. While first outcrops ablate as early as the end of June, some snow patches remain until August. This rather complex distribution pattern leads to a high spatial variability in the soil moisture conditions.

During snow-free conditions, the thaw depth and bedrock topography were found to effectively control infiltration depths. While some infiltration into frozen ground and bedrock takes place, most water infiltrates until this surface and runs off along it. Shallow thaw depths or bedrock surfaces result in a concentration of laterally flowing water near the surface. At the soil moisture sensors this effect is visible at the beginning of the snow-free season, when thaw depths are shallow and the sensor location is influenced by upslope snow patches. During this time, daily peaks in the snow melt lead to high soil moisture contents near the surface. Later in the summer, when the active layer has grown and upslope snow patches have diminished, only long lasting and intense precipitation events may lead to saturated conditions near the surface, although precipitation intensities may be much higher than snow melt rates. In general, water flows out quickly and low values are reached shortly after the replenishment by snow melt or precipitation has stopped. Low values are higher at the beginning of the season, when daily replenishment and shallow thaw depths lead to high near-surface water contents. The lowest low values are reached after long dry periods (evaporative loss) and with high thaw depths (ineffective capillary rise).

At the boreholes, different geological settings lead to particularly different soil moisture conditions. At SCH5198, the layer of loose debris (sandy soil) extends to 5 m depth which results in an enhanced water retention capacity and lateral inflow of soil water at depth. At the surface however, conditions are relatively dry due to the quick percolation of the soil water into deeper layers and a less effective capillary rise from depth. The borehole temperatures show a relatively high thermal variability. Furthermore, distinct temperature peaks in relation to rain water infiltration events can be identified. This study suggests that the high thermal variability is due to an enhanced thermal conductivity and diffusivity at depth in relation to the relatively high water contents.

At SCH5000/SCH5200 in contrary, the layer of loose debris is only 2 m in thickness. Water is therefore ponded at the bedrock surface and is mainly concentrated in the uppermost 2 m throughout the summer, leading to rather wet conditions near the surface. Below the bedrock surface, water may infiltrate but the conditions are rather dry in comparison to SCH5198, due to the low total pore volume in the bedrock. It is suggested that the relatively dry conditions at depth are partly responsible for the overall smaller

thermal variability compared to SCH5198 (lower thermal conductivity and diffusivity). Furthermore, as soil moisture is concentrated near the surface, evaporation is more effective and leads to a reduced amount of heat which is conducted into the ground. However, SCH5000 and SCH5200 are insulated with a PVC pipe in contrast to SCH5198, which is uninsulated. The role of the borehole casing was not assessed in this study and may have a significant influence on the thermal variability.

In general, it was found that the impact of soil moisture on the thermal regime is most pronounced through latent heat effects. In frozen conditions, the refreezing of soil water leads to the release of latent heat and consequently to ice melt and ground temperature increase. It effectively preconditions the soil for active layer growth. In unfrozen conditions in contrary, evaporation is an effective heat sink and may reduce the amount of heat conducted in the ground. Secondly, soil moisture may effectively change ground thermal properties such as the thermal conductivity and diffusivity which has a considerable impact on the thermal regime. Finally, sensible heat fluxes in contrary are attributed to rain water infiltration and only of short duration. They are regarded as negligible. However, non-conductive heat transfer was found to only alter the thermal regime while heat conduction is dominant in the active layer growth. The spatial distribution of soil moisture strongly depends on the snow conditions, the geological setting as well as hillslope water flow processes. At Schilthorn and in alpine permafrost soils in general, they can be spatially very heterogeneous. The relative impact of soil moisture on the thermal regime may therefore change on small scales and therefore partly explain the thermal differences between the three boreholes at Schilthorn.

9.2 Outlook

In order to verify the hypotheses stated above, further analyses are necessary. This study has shown that with a smaller spacing and information about the meteorological, snow and soil moisture conditions, small scale hydrological processes can effectively be identified. In order to complete the assessment of the soil moisture regimes, measurements along a small spaced ERT line throughout the year could be very useful. Furthermore, a complete set of measurements by the soil moisture sensors, which was missing for certain periods in 2014, would be valuable.

At the field site, water flow in the subsurface is measured by the self-potential method (Wege, September 29, 2014). The results of this method are promising and the intensity of subsurface water flow could be identified in a first study. In future studies, this data could be useful to verify the hypotheses on hillslope water flow processes.

The different casings of the boreholes could considerably alter the thermal regimes at the boreholes through insulation at SCH5000/SCH5200 and through water intrusion and preferential flow within the borehole at SCH5198. In order to be able to directly compare the two boreholes and to directly assess the thermal influence of soil moisture, an assessment of the casing's influence is necessary. This could be achieved by modelling the conductive heat flow through the material of the borehole casing.

Finally, a comparative simulation of the mass and heat exchange at both boreholes could be used to verify and quantify the different soil moisture effects on the thermal regime. The coupled heat and mass transfer model for soil-plant-atmosphere systems (COUP model) proved to be useful for this purpose. The additional information on seasonal soil moisture variation and lateral flow processes are a necessary precondition to be able to precisely model the soil moisture processes at the boreholes.

Bibliography

Archie GE, The electrical resistivity log as an aid to determining some reservoir characteristics. 1942, *Transactions of the American Institute of Mining, Metallurgical, and Petroleum Engineers* **146**: 389–409.

Arenson LU, Hauck C, Hilbich C, Seward L, Yamamoto Y and Springman SM, Sub-surface Heterogeneities in the Murtèl - Corvatsch Rock Glacier, Switzerland. In *63rd Annual Canadian Geotechnical Conference and the 6th Canadian Permafrost Conference*, Alta. 2010.

Beltrami H, Active Layer Distortion of Annual Air/Soil Thermal Orbits. 1996, *Permafrost and Periglacial Processes* **7**: 101–110.

Binley A, Cassiani G, Middleton R and Winship P, Vadose zone flow model parameterisation using cross-borehole radar and resistivity imaging. 2002, *Journal of Hydrology* **267**(3-4): 147–159, ISSN 00221694, doi:10.1016/S0022-1694(02)00146-4.

Binley A, Hubbard SS, Huisman JA, Revil A, Robinson DA, Singha K and Slater LD, The emergence of hydrogeophysics for improved understanding of subsurface processes over multiple scales. 2015, *Water Resources Research* **51**(6): 3837–3866, doi:10.1002/2015WR017016.

Boike J, Roth K and Overduin PP, Thermal and hydrologic dynamics of the active layer at a continuous permafrost site Taymyr Peninsula, Siberia. 1998, *Water Resources Research* **34**(3): 355–363.

Boike J, Wille C and Abnizova A, Climatology and summer energy and water balance of polygonal tundra in the Lena River Delta, Siberia. 2008, *Journal of Geophysical Research* **113**(G3), doi:10.1029/2007JG000540.

Brunet P, Clément R and Bouvier C, Monitoring soil water content and deficit using Electrical Resistivity Tomography (ERT) – A case study in the Cevennes area, France. 2010, *Journal of Hydrology* **380**(1-2): 146–153, ISSN 00221694, doi:10.1016/j.jhydrol.2009.10.032.

Bundesgeoportal, Landeskarte 1:25'000. https://map.geo.admin.ch. 2015, online; accessed 10th of October 2015.

Daily W, Ramirez A, Binley A and LeBrecque D, Electrical resistance tomography. 2004, *The Leading Edge* **23**(5): 438–442, ISSN 1070-485X, doi:10.1190/1.1729225.

Daily W, Ramirez A, LaBreque D and Nitao J, Electrical resistivity tomography of vadose water movement. 1992, *Water Resources Research* **28**(5): 1429–1442.

Delaloye R and Lambiel C, Evidence of winter ascending air circulation throughout talus slopes and rock glaciers situated in the lower belt of alpine discontinuous permafrost (Swiss Alps). 2005, *Norsk Geografisk Tidsskrift - Norwegian Journal of Geography* **59**(2): 194–203, ISSN 0029-1951, doi:10.1080/00291950510020673.

Delta-T Devices, *ThetaProbe soil moisture sensor type ML2x user manual ML2x-UM-1.21: User manual*. 2011.

Dobinski W, Permafrost. 2011, *Earth-Science Reviews* **108**(3-4): 158–169, ISSN 00128252, doi:10.1016/j.earscirev.2011.06.007.

Farinotti D, Usselmann S, Huss M, Bauder A and Funk M, Runoff evolution in the Swiss Alps: projections for selected highalpine catchments based on ENSEMBLES scenarios. 2011, *Hydrological Processes* **25**.

French H and Binley A, Snowmelt infiltration: monitoring temporal and spatial variability using time-lapse electrical resistivity. 2004, *Journal of Hydrology* **297**(1-4): 174–186, ISSN 00221694, doi:10.1016/j.jhydrol.2004.04.005.

French HK, Hardbattle C, Binley A, Winship P and Jakobsen L, Monitoring snowmelt induced unsaturated flow and transport using electrical resistivity tomography. 2002, *Journal of Hydrology* **267**(3-4): 273–284, ISSN 00221694, doi:10.1016/S0022-1694(02)00156-7.

French HM, *The Periglacial Environment*. John Wiley & Sons Ltd, West Sussex, 3rd edition edn. 2007.

Gruber S and Haeberli W, Mountain Permafrost. In Margesin R (ed.) *Permafrost Soils*, Soil Biology, pp. 33–44, Springer-Verlag, Berlin and Heidelberg. 2010.

Gruber S and Hoelzle M, The Cooling Effect of Coarse Blocks Revisited: A Modeling Study of a Purely Conductive Mechanism. In Kane DL and Hinkel KM (eds.) *Ninth International Conference on Permafrost*, pp. 557–651, Institute of Northern Engineering, University of Alaska, Fairbanks and Alaska. 2008.

Haeberli W, Noetzli J, Arenson L, Delaloye R, Gärtner-Roer I, Gruber S, Isaksen K, Kneisel C, Krautblatter M and Phillips M, Mountain Permafrost: Development and Challenges of a Young Research Field. 2010, *Journal of Glaciology* **56**(200): 1043–1058, ISSN 00221430, doi:10.3189/002214311796406121.

Harris C, Arenson LU, Christiansen HH, Etzelmüller B, Frauenfelder R, Gruber S, Haeberli W, Hauck C, Hölzle M, Humlum O, Isaksen K, Kääb A, Kern-Lütschg MA, Lehning M, Matsuoka N, Murton JB, Nötzli J, Phillips M, Ross N, Seppälä M, Springman SM and Vonder Mühll D, Permafrost and climate in Europe: Monitoring and modelling thermal, geomorphological and geotechnical responses. 2009, *Earth-Science Reviews* **92**(3-4): 117–171, ISSN 00128252, doi:10.1016/j.earscirev.2008.12.002.

Harris C, Vonder Mühll D, Isaksen K, Haeberli W, Sollid JL, King L, Holmlund P, Dramis F, Guglielmin M and Palacios D, Warming permafrost in European mountains. 2003, *Global and Planetary Change* **39**(3-4): 215–225, ISSN 09218181, doi:10.1016/j.gloplacha.2003.04.001.

Hartge KH and Horn R, *Einführung in die Bodenphysik*. Enke, Stuttgart, 2 edn. 1991, ISBN 3-432-89682-4.

Hauck C, *Geophysical methods for detecting permafrost in high mountains*. Ph.D. thesis, ETH, Zürich. 2001.

Hauck C, Frozen ground monitoring using DC resistivity tomography. 2002, *Geophysical Research Letters* **29**(21), doi:10.1029/2002GL014995.

Hauck C and Kneisel C (eds.) *Applied geophysics in periglacial environments*. Cambridge University Press, Cambridge and UK and New York. 2008, ISBN 9781107406193.

Hilbich C, Fuss C and Hauck C, Automated Timelapse ERT for Improved Process Analysis and Monitoring of Frozen Ground. 2011, *Permafrost and Periglacial Processes* **22**(4): 306–319.

Hilbich C, Hauck C, Hoelzle M, Scherler M, Schudel L, Völksch I, Vonder Mühll D and Mäusbacher R, Monitoring mountain permafrost evolution using electrical resistivity tomography: A 7-year study of seasonal, annual, and long-term variations at Schilthorn, Swiss Alps. 2008, *Journal of Geophysical Research* **113**, doi:10.1029/2007JF000799.

Hillel D, *Introduction to environmental soil physics*. Elsevier Academic Press, Amsterdam and Boston. 2004, ISBN 978-0-12-348655-4.

Hock R, A distributed temperature-index ice- and snowmelt model including potential direct solar radiation. 1999, *Journal of Glaciology* **45**: 101–111, ISSN 00221430.

Hoelzle M, *Permafrost und Gletscher im Oberengadin. Grundlagen und Anwendungspeispiele für automatisierte Schätzverfahren.* Mitteilungen der Versuchsanstalt für Wasserbau, Hydrologie und Glaziologie, Prof. Dr. D. Fischer, Zürich. 1994.

Hoelzle M, Energiebilanz am Schilthorn. Personal Communication. October 28, 2015.

Hoelzle M and Gruber S (eds.), *Borehole and Ground Surface Temperatures and Their Relationship to Meteorological Conditions in the Swiss Alps.* 2008.

Hoelzle M, Mittaz C, Ezelmüller B and Haeberli W, Surface Energy Fluxes and Distribution Models of Permafrost in European Mountain Areas: an Overview of Current Developments. 2001, *Permafrost and Periglacial Processes* **12**: 53–68.

Huss M, Farinotti D, Bauder A and Funk M, Modelling runoff from highly glacierized alpine drainage basins in a changing climate. 2008, *Hydrological Processes* **22**(19): 3888–3902, doi:10.1002/hyp.7055.

Imhof M, Pierrehumbert G, Haeberli W and Kienholz H, Permafrost Investigation in the Schilthorn Massif, Bernese Alps, Switzerland. 2000, *Permafrost and Periglacial Processes* **11**: 189–206.

IMKO, *TRIME-PICO 64/32 Manual: Instruction manual.* 2011.

Kane DL, Hinkel KM, Goering DJ, Hinzman LD and Outcalt SI, Non-conductive heat transfer associated with frozen soils. 2001, *Global and Planetary Change* **29**(3-4): 275–292, ISSN 09218181, doi:10.1016/S0921-8181(01)00095-9.

Kane DL and Stein J, Water Movement Into Seasonally Frozen Soils. 1983, *Water Resources Research* **19**(6): 1547–1557.

Keller F, Frauenfelder R, Gardaz JM, Hoelzle M, Kneisel C, Lugon R, Phillips M, Reynard E and Wenker L (eds.), *Permafrost Map of Switzerland.* 1998.

Kneisel C, Hauck C, Fortier R and Moorman B, Advances in geophysical methods for permafrost investigations. 2008, *Permafrost and Periglacial Processes* **19**(2): 157–178, doi:10.1002/ppp.616.

Krauss L, Hauck C and Kottmeier C, Spatio-temporal soil moisture variability in Southwest Germany observed with a new monitoring network within the COPS domain. 2010, *Meteorologische Zeitschrift* **19**(6): 523–537, doi:10.1127/0941-2948/2010/0486.

Loke MH, *Tutorial: 2-D and 3-D electrical imaging surveys.* 2001.

Machguth H, Paul F, Hoelzle M and Haeberli W, Distributed glacier mass-balance modelling as an important component of modern multi-level glacier monitoring. 2006, *Annals of Glaciology* **43**: 335–343.

Mittaz C, Imhof M, Hoelzle M and Haeberli W, Snowmelt Evolution Mapping Using an Energy Balance Approach over an Alpine Terrain. 2002, *Arctic, Antarctic, and Alpine Research* **34**(2): 274–281.

Nestler A, Huss M, Ambartzumian R and Hambarian A, Hydrological Implications of Covering Wind-Blown Snow Accumulations with Geotextiles on Mount Aragats, Armenia. 2014, *Geosciences* **4**(3): 73–92, ISSN 2076-3263, doi:10.3390/geosciences4030073.

Noetzli J (ed.) *Permafrost in Switzerland 2008/2009 and 2009/2010*, vol. 10/11 of *Glaciological Report (Permafrost)*. Cryospheric Commission of the Swiss Academy of Sciences (SCNAT). 2013.

Noetzli J, Schilthorn - Wasser im Rohr von SCH_5000? Personal Communication. August 10, 2015.

Noetzli J, Gruber S, Kohl T, Salzmann N and Haeberli W, Three-dimensional distribution and evolution of permafrost temperatures in idealized high-mountain topography. 2007, *Journal of Geophysical Research* **112**(F2), doi:10.1029/2006JF000545.

Noetzli J, Hilbich C, Hauck C, Hoelzle M and Gruber S, Comparison of Simulated 2D Temperature Profiles with Time-Lapse Electrical Resistivity Data at the Schilthorn Crest, Switzerland. In Kane DL and Hinkel KM (eds.) *Ninth International Conference on Permafrost*, pp. 1293–1298, Institute of Northern Engineering, University of Alaska, Fairbanks and Alaska. 2008.

Noetzli J, Naegeli B and Vonder Mühll D (eds.) *Permafrost in Switzerland 2004/2005 and 2005/2006*, vol. 6/7 of *Glaciological Report (Permafrost)*. Cryospheric Commission of the Swiss Academy of Sciences (SCNAT). 2009.

Oerlemans J, *Glaciers and climate change*. Swets & Zeitlinger BV, Lisse. 2001.

Pellet C, *Soil moisture monitoring station Schilthorn documentation*. 2014.

Pellet C, Calibration of Soil Moisture Sensors. Personal Communication. December 17, 2015.

Pellet C, Hauck C, Hilbich C and Marmy A, Soil water and ice content validation for permafrost models using direct and indirect measurement approaches. In *Book of Abstracts of EUCOP4 - 4th European Conference on Permafrost.*, Évora and Portugal. 2014.

Pellet C, Hilbich C, Marmy A and Hauck C, Soil moisture data for the validation of permafrost models using direct and indirect measurement approaches at three alpine sites. 2015, *Frontiers in Earth Science* .

PERMOS, Borehole Data Browser. http://shinypermos.geo.uzh.ch/app/BoreholeDataBrowser/. 2015, online; accessed 21st of December 2015.

Reynolds JM, *An introduction to applied and environmental geophysics*. Wiley-Blackwell, Chichester and West Sussex and Malden and Mass, 2nd ed edn. 2011, ISBN 978-0-471-48535-3.

Rist A and Phillips M, First results of investigations on hydrothermal processes within the active layer above alpine permafrost in steep terrain. 2005, *Norsk Geografisk Tidsskrift - Norwegian Journal of Geography* **59**(2): 177–183, ISSN 0029-1951, doi: 10.1080/00291950510020574.

Rosset E, Hilbich C, Schneider S and Hauck C, Automatic filtering of ERT monitoring data in mountain permafrost. 2013, *Near Surface Geophysics* **11**(1983), doi:10.3997/1873-0604.2013003.

Schär C, Vidale PL, Lüthi D, Frei C, Häberli C, Liniger MA and Appenzeller C, The role of increasing temperature variability in European summer heatwaves. 2004, *Nature* **427**(6972): 328–332, ISSN 0028-0836, doi:10.1038/nature02230.

Scherler M, Hauck C, Hoelzle M and Salzmann N, Modeled sensitivity of two alpine permafrost sites to RCM-based climate scenarios. 2013, *Journal of Geophysical Research: Earth Surface* **118**(2): 780–794, doi:10.1002/jgrf.20069.

Scherler M, Hauck C, Hoelzle M, Stähli M, Völksch and Ingo, Meltwater Infiltration into the Frozen Active Layer at an Alpine Permafrost Site. 2010, *Permafrost and Periglacial Processes* **21**(4): 325–334.

Schlaeger S, Huebner C and Becker R, Simple soil moisture probe for low cost measurement applications. In Kaatze U, Kupfer and Hübner C (eds.) *6th Conference on Electromagnetic Wave Interaction with Water and Moist Substances*. 2005.

Slater L, Zaidman MD, Binley AM and West LJ, Electrical Imaging of Saline Tracer Migration for the Investigation of Unsaturated Zone Transport Mechanismus. 1997, *Hydrology and Earth System Sciences* **1**(2): 291–302.

Spaans, E J A and Baker JM, The Soil Freezing Characteristic: Its Measurement and Similarity to the Soil Moisture Characteristic. 1996, *Soil Science Society of America Journal* **60**: 13–19.

Spreafico M, Weingartner R, Barben M and Ryser A, *Hochwasserabschätzung in schweizerischen Einzugsgebieten*, vol. 4 of *Berichte des BWG, Serie Wasser*. Bern. 2003.

Stähli M, Jansson PE and Lundin LC, Preferentail Water Flow in a Frozen Soil - A Two-Domain Model Approach. 1996, *Hydrological Processes* **10**: 1305–1316.

Tian H, Wei C, Wei H and Zhou J, Freezing and thawing characteristics of frozen soils: Bound water content and hysteresis phenomenon. 2014, *Cold Regions Science and Technology* **103**: 74–81, ISSN 0165232X, doi:10.1016/j.coldregions.2014.03.007.

TRICON Geophysik und Systemtechnik GmbH, Munich, Geoelektrik: Grundlagen. http://tricon-online.de/html/geoelektrik.html. 2015, online; accessed 21st of October 2015.

Truebner, *SMT100 soil moisture sensor: Fact sheet*. 2012.

van Everdingen R, *Multi-language glossary of permafrost and related ground-ice terms*. Boulder. 2005.

Vonder Mühll D, Hauck C and Lehmann F, Verification of geophysical models in Alpine permafrost using borehole information. 2000, *Annals of Glaciology* **31**.

Vonder Mühll D, Noetzli J, Makowski K and Delaloye R (eds.) *Permafrost in Switzerland 2000/2001 and 2001/2002*, vol. 2/3 of *Glaciological Report (Permafrost)*. Cryospheric Commission of the Swiss Academy of Sciences (SCNAT). 2004.

Wege S, *Self potential measurements to detect meltwater streams in permafrost soils at the Schilthorn*. Ph.D. thesis, University of Bonn, Bonn. September 29, 2014.

Westermann S, Wollschläger U and Boike J, Monitoring of active layer dynamics at a permafrost site on Svalbard using multi-channel ground-penetrating radar. 2010, *The Cryosphere* **4**(4): 475–487, ISSN 1994-0424, doi:10.5194/tc-4-475-2010.

Wicki A, *GERM Schilthorn. Application of the Glacier Runoff Evolution Model at Schilthorn (Bernese Alps)*. 2015.

Williams PJ and Smith MW, *The Frozen Earth*. Cambridge University Press, Cambridge and United Kingdom. 1989.

Wollschläger U, Gerhards H, Yu Q and Roth K, Multi-channel ground-penetrating radar to explore spatial variations in thaw depth and moisture content in the active layer of a permafrost site. 2010, *The Cryosphere* **4**(3): 269–283, ISSN 1994-0424, doi:10.5194/tc-4-269-2010.

Wright N, Hayashi M and Quinton WL, Spatial and temporal variations in active layer thawing and their implication on runoff generation in peat-covered permafrost terrain. 2009, *Water Resources Research* **45**(5): n/a, doi:10.1029/2008WR006880.

Zenklusen Mutter E and Phillips M, Active Layer Characteristics At Ten Borehole Sites In Alpine Permafrost Terrain, Switzerland. 2012a, *Permafrost and Periglacial Processes* **23**(2): 138–151, doi:10.1002/ppp.1738.

Zenklusen Mutter E and Phillips M, Thermal Evidence of Recent Talik Formation in Ritigraben Rock Glacier: Swiss Alps. In Hinkel KM (ed.) *Tenth International Conference on Permafrost. Resources and Risks of Permafrost Areas in a Changing World*, vol. 1 of *International Contributions*, The Northern Publisher, Salekhard. 2012b.

Appendix A

Appendix

A.1 Borehole Temperatures

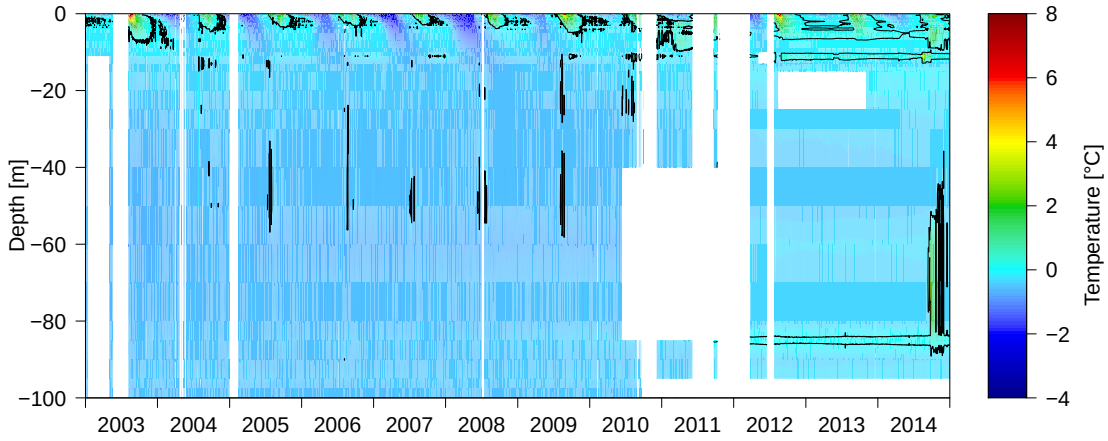


Figure A.1: Contour Plot of the daily mean subsurface temperatures at SCH5000 in 2003 to 2014. The black lines indicate the 0° C isoline.

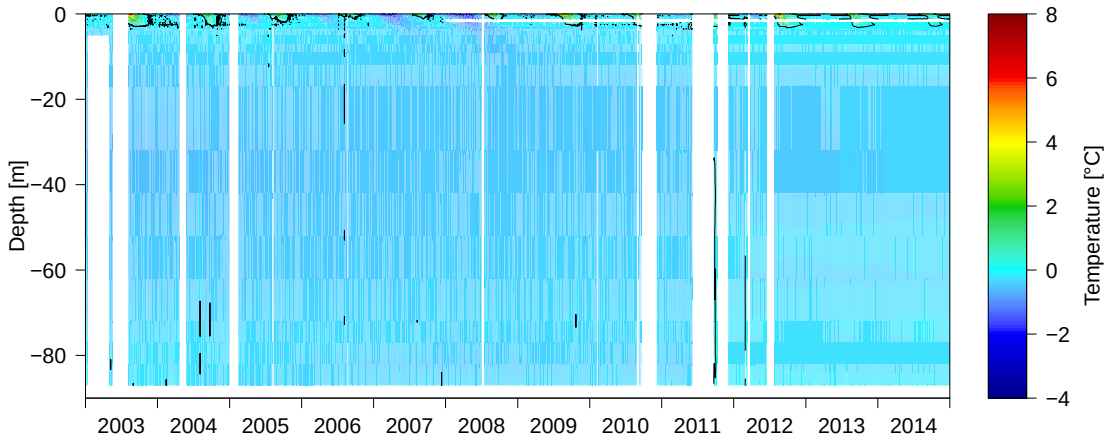


Figure A.2: Contour Plot of daily mean subsurface temperatures at SCH5200 in 2003 to 2014. The black lines indicate the 0° C isoline.

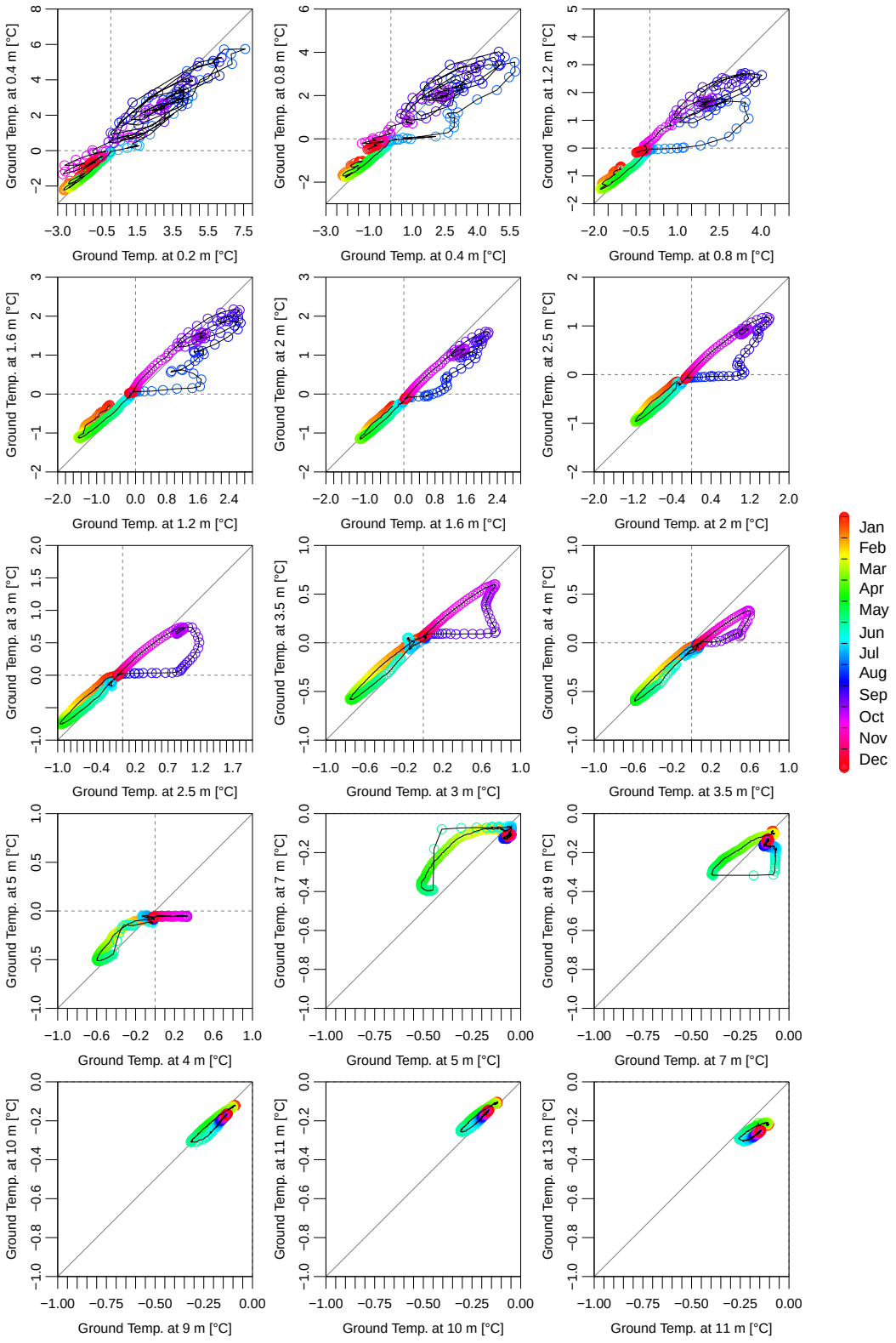


Figure A.3: Thermal Orbits for daily mean temperatures in the year 2014 at SCH5198 for all temperature sensors.

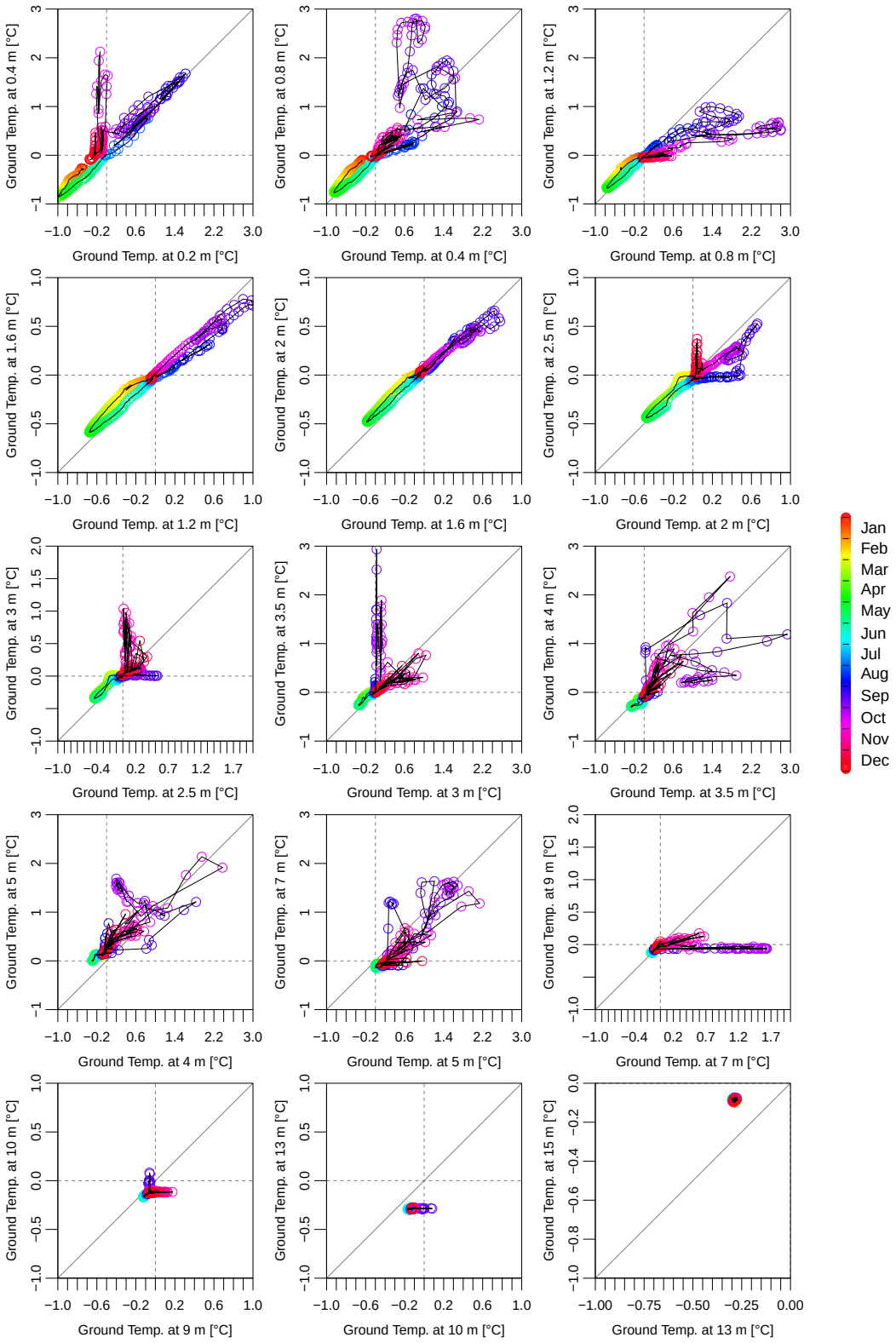


Figure A.4: Thermal Orbits for daily mean temperatures in the year 2014 at SCH5000 for the upper 15 m.

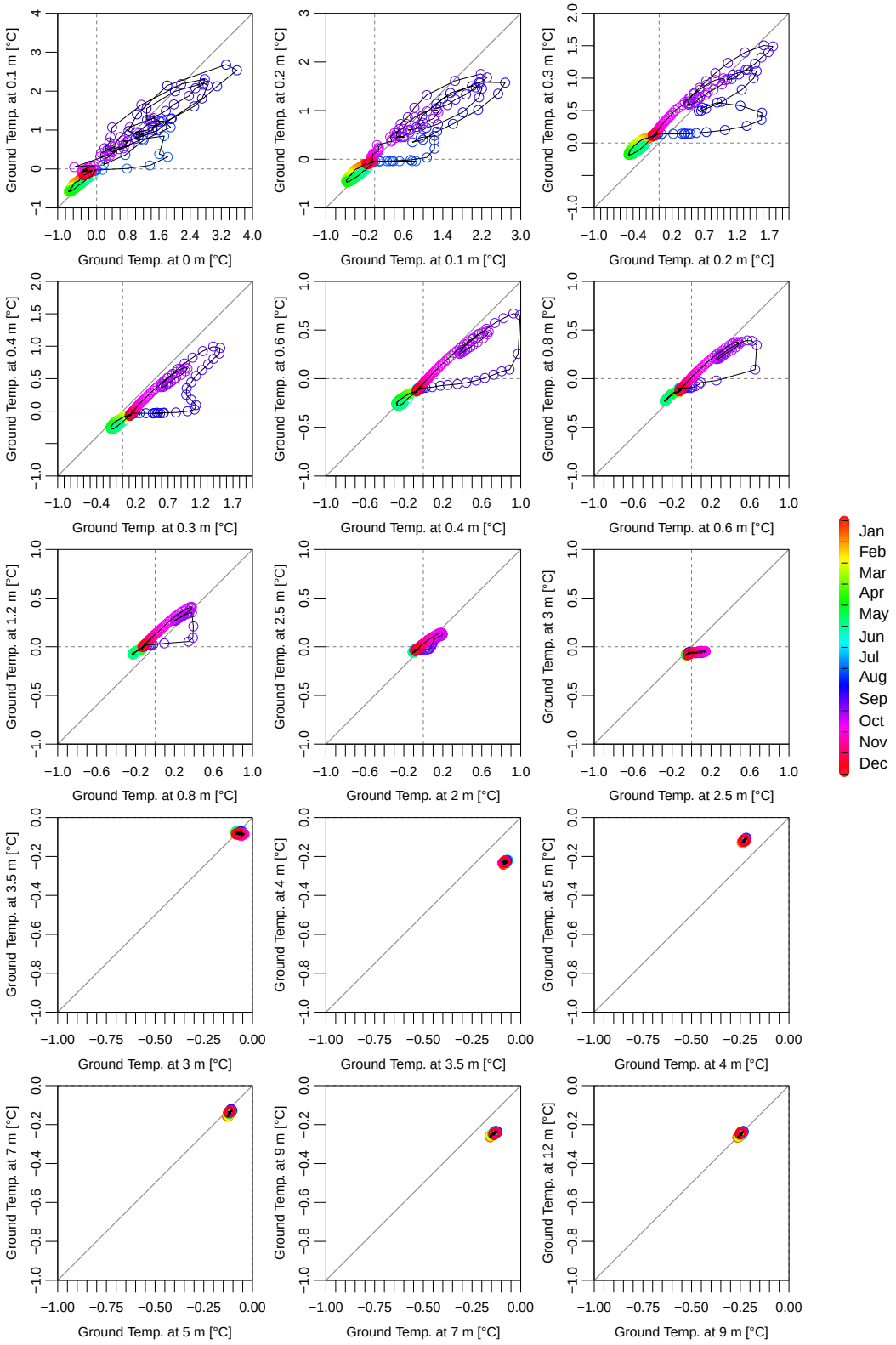


Figure A.5: Thermal Orbits for daily mean temperatures in the year 2014 at SCH5200 for the upper 12 m. The sensor at 1.6 m depth is missing due to missing values.